The Pennsylvania State University

The Graduate School

Graduate Program in Petroleum and Natural Gas Engineering

NUMERICAL AND ANALYTICAL MODELS OF SECONDARY MIGRATION IN FAULTS: DYNAMIC CONTROLS ON HYDROCARBON COLUMN HEIGHT

A Thesis in

Petroleum and Natural Gas Engineering

by

James Paul Ashbaugh

Submitted in Partial Fulfillment
of the Requirements
for the Degree of

Master of Science

December 1997

ABSTRACT

Multi-phase flow modeling has the potential to illuminate the processes by which hydrocarbons are emplaced during secondary migration. An analytical and numerical model of multi-phase flow is presented to describe the relationship between secondary migration through fault zones and the concurrent charging of reservoirs in juxtaposition with these faults. The reservoir hydrocarbon column heights that result from this process are controlled by the petrophysical properties of the fault zone, the flux of water and hydrocarbons in the fault zone, and the geometry of the reservoir. At steady state, the capillary pressure between the fluid phases must be equal in the fault zone and the reservoir. This capillary pressure determines the hydrocarbon column height in the reservoir.

Key results of the modeling are: 1) For a given oil flux, the presence of a dynamic water phase in the fault zone will decrease the oil column height in the reservoir. The amount of decrease will be directly dependent on the water potential gradient in the fault. 2) Three phase oil and gas column heights are a dynamic function of charge rate. 3) Given similar petrophysical fault properties with depth, the reservoir charge rate is controlled by fault zone anisotropy.

TABLE OF CONTENTS

LIST OF FIGURES

LIST OF TABLES

ACKNOWLEDGMENTS

I would like thank Exxon Production Research Company for their support of this research and the efforts Exxon's Trap, Charge, and Retention Section in providing guidance and support.

I thank Dr. Turgay Ertekin for his technical assistance in the area of numerical modeling. I thank Dr. Peter Flemings for providing input to the project from a geologist's perspective and for reviewing this document.

I thank Dr. Paul Hicks, Jr. who provided guidance and support in all aspects of this research. I am particularly appreciative of the thorough review and input provided by Dr. Hicks during every step of the research project.

Most of all I wish to thank my wife for all of her support and encouragement.

NOMENCLATURE

A - Cross-sectional area of the fault [L^2]

B_g - Gas formation volume factor [L^3 at reservoir conditions/L^3 at standard conditions]

B_o - Oil formation volume factor [L^3 at reservoir conditions/L^3 at standard conditions]

g - Gravitational acceleration [L/T^2]

k - Intrinsic permeability [L^2]

kr_g - Gas phase relative permeability as a function of S_g [dimensionless]

kr_o - Oil phase relative permeability as a function of S_g and S_w [dimensionless]

kr_w - Water phase relative permeability as a function of S_w [dimensionless]

P_g - Gas phase pressure [M/LT^2]

P_o - Oil phase pressure [M/LT^2]

P_w - Water phase pressure [M/LT^2]

Q_g - Gas flow rate [L^3/T at standard conditions]

Q_o - Oil flow rate [L^3/T at standard conditions]

Rs_o - Solution oil-gas ratio [L^3 gas at standard conditions/L^3 oil at standard conditions]

S_g - Gas phase saturation [L^3/L^3]

S_o - Oil phase saturation [L^3/L^3]

S_w - Water phase saturation [L^3/L^3]

S_{wirr} - Irreducible water phase saturation [L^3/L^3]

z - Vertical distance from a fixed datum [L]

Φ_o - Oil phase potential [M/LT^2]

μ_g - Gas phase viscosity [M/LT]

μ_o - Oil phase viscosity [M/LT]

μ_w - Water phase viscosity [M/LT]

ρ_g - Gas phase density [M/L^3]

ρ_o - Oil phase density [M/L^3]

ρ_w - Water phase density [M/L^3]

θ - Angle from vertical

Subscripts: g - gas

o - oil

w - water

Chapter 1

INTRODUCTION

Fault zones have been considered to be pathways for secondary hydrocarbon migration, seals which trap hydrocarbons migrating up-structure through reservoir sands, and combined conduit-barrier systems (Hippler, 1993; Schowalter, 1979; Antonellini and Aydin, 1994; Caine et al., 1996.). Hippler (1993) supports the concept that hydrocarbons migrate through brecciated fault zones on the basis of hydrocarbon staining of the fault zone. Others propose that crushing of the rock in the fault zone significantly reduces the porosity and permeability of the fault thus causing the fault zone to act as a seal (Bouvier et al., 1989; Antonellini and Aydin, 1994). Studies by Antonellini and Aydin (1994) showed fault zone reductions in permeability of three orders of magnitude and in porosity of one order of magnitude. Caine et al. (1996) proposed a system whereby the fault is evaluated as two regions; a damaged region where little displacement has occurred but where the permeability has been enhanced by fractures and a core zone where most of the displacement has occurred and the rock has been pulverized. In Cain et al.'s model the fault can act as a conduit, a barrier or a combination conduit-barrier.

Showalter (1979) proposed that hydrocarbon column height in reservoirs in juxtaposition to the fault zone could be calculated using the capillary properties of the sealing material (fault zone). This theory was supported by Pittman (1981) who proposed that the deformation and crushing of rocks in and around the fault zone results

in lower permeability and porosity than in the surrounding unaffected rock. The result is an increase in the capillary entry pressure, the minimum pressure necessary for hydrocarbons to infiltrate the fault zone. In this "capillary entry pressure" model, hydrocarbon column height in the reservoir sand is a static function of the capillary entry pressure.

Bennett (1996) presented a conceptual model whereby the fault zone acts as a conduit, charging reservoirs in juxtaposition with the fault and due to differences in petrophysical properties, as a seal to trap hydrocarbons in the reservoir sand. He then developed a steady-state analytic model for hydrostatic systems, which demonstrated that steady-state hydrocarbon column height in reservoirs in juxtaposition with the fault is a not only a function of the capillary properties of the fault, but a dynamic function of the oil flux in the fault. A numerical reservoir simulator was then used to study transient effects, the effects of vertical variations in fault properties, and the effects of reservoir geometry on hydrocarbon column height. All cases examined were 2-phase (oil-water) systems where there was no water flux in the fault zone and the fault zone was isotropic. For such systems, Bennett (1996) concluded that:

1) Hydrocarbon column height is a dynamic function of charge rate and not a static function of capillary-entry pressure as is often assumed.
2) Faults can serve both as migration pathways and as seals.
3) Hydrocarbons can charge along faults and then backfill adjacent sands.
4) Under-filled structures may result from lateral pinch-out or truncation of reservoirs and the inability of hydrocarbons to displace the water already present.
5) Given similar petrophysical fault properties with depth and no permeability anisotropy, deeper sands will fill sequentially before shallower sands.

We expanded on Bennett's work in three areas. First, in Chapter 2 we consider the effect of flow of water and oil in order to simulate secondary migration. We show that for a given oil flux through the fault, oil column height in juxtaposed reservoir sands decreases as fault zone water flux increases. In Chapter 2, we develop a steady-state analytical model which demonstrates that steady-state hydrocarbon column height is a function of not only hydrocarbon charge history, but also water flux through the fault zone. We then use a numerical model to evaluate the effect of the fault-zone capillary pressure relationship and reservoir boundary conditions on hydrocarbon column height.

Second, in Chapter 3 we extend the two-phase model to consider three-phase (gas, oil, water) systems. We develop a steady-state analytical model which predicts steady-state hydrocarbon (oil and gas) column height. We then investigate the effect of reservoir geometry and hydrocarbon charging on transient hydrocarbon column height with a numerical. We show with that one of the two migrating hydrocarbon phases will generally overcharge the sand and then be flushed from the reservoir by the other phase until the predicted steady-state condition is acheived.

Finally, we used the 2-phase (oil-water) numerical model to show that fault-zone permeability anisotropy can cause potential reservoirs to be charged slowly or completely bypassed by hydrocarbons migrating through the fault zone.

In all cases numerical modeling was completed using the Eclipse 100 numerical reservoir simulation software by GeoQuest®.

Chapter 2

GEO-PRESSURED TWO-PHASE SYSTEMS

Model Objectives

Fault zones which act as migration pathways for hydrocarbons often act as conduits for water being forced from sediments as they are compacted by overburden. The purpose of this modeling effort was to investigate the effect of water flux in the fault zone upon hydrocarbon column height in the reservoir sands. In this model we evaluate, both analytically and numerically, the effect water migration through the fault has upon the oil flux equation and consequently oil column height.

Model Constraints

We consider the system (*Figure Chapter 1-1)* where a sand is in juxtaposition with a fault. Oil is migrating up the fault at a constant flux (Q_o) and constant pressure conditions are specified at the top of the fault for the oil phase (P_o) and at the bottom of the fault for the water phase (P_w). The constant pressure boundaries of the fault are used to establish a water-phase pressure gradient within the fault (*Figure Chapter 1-2*).

Two sets of capillary pressure data were used for the fault zone in the geo-pressure modeling. The first data set was generated using Thomeer's relationship (Jorden and Campbell, 1984):

$$P_c = e^{\left(\log P_d - \left(\frac{G}{\log\left(\frac{S_o}{1-S_{wirr}}\right)}\right)\right)} \quad \text{(Chapter 1-1)}$$

where P_c is the capillary pressure, P_d is the capillary entry pressure, G is the pore geometry factor, S_{wirr} is the irreducible water saturation, and S_o is the oil saturation. *Table Chapter 1-1* lists the parameters used to generate capillary pressure curves (*Figure Chapter 1-3*) for the fault zone and reservoir sand. The capillary pressure curves were modified from Thomeer's equation in the 0.99 to 1.00 S_w range to allow P_{cow} to go to zero at an S_w of 1.0. The parameters used in Thomeer's equation generated a capillary pressure for which at high water saturation, capillary pressure slowly decreased with increasing water saturation. This relationship provides a capillary pressure versus oil saturation (S_o) for a typical hydrocarbon reservoir. A second data set, provided by Exxon Production Research (EPR), was derived by conducting laboratory experiments on core from a fault zone (*Figure Chapter 1-4*). The same reservoir capillary pressure curve, which was determined using Thomeer's equation, was used in both cases.

Table Chapter 1-1: Parameters for Thomeer's Relationship

Variable	Fault	Reservoir
P_d	10.0 psi	5.0 psi
G	0.1	0.5
S_{wirr}	0.3	0.2

The oil-water relative permeability curves for the fault zone and sand are given in *Figure Chapter 1-5* and *Figure Chapter 1-6*, respectively.

Table Chapter 1-2 presents model input data used in all analytical and numerical geo-pressure models.

Table Chapter 1-2: Geo-Pressure Model Input Parameters

Parameter	Value	Units
Q_o/A	$2.95x10^{-7}$	STB/day/ft2
μ_o	0.352	cp
ρ_o	53	lb/ft^3
ρ_w	67	lb/ft^3
k_f	0.017	millidarcies
θ	5^o	

Analytical Model Development

We start with the one-dimensional steady-state incompressible flow equation for a system which is governed by Darcy's Law (Chapter 1-2) :

$$\frac{Q_o}{A} = \frac{kkr_o}{\mu_o}(\nabla\Phi_o)_f \qquad \text{(Chapter 1-2)}$$

Note that the oil formation factor (Bo) is not included in this development because due to the incompressible assumption it is taken to be 1.

The oil-phase potential (Φ_o) is defined as:

$$\Phi_o = P_o - \rho_o g z \qquad \text{(Chapter 1-3)}$$

and we define oil-water capillary pressure (P_{cow}) for a water-wet system as:

$$P_{cow} = P_o - P_w \qquad \text{(Chapter 1-4)}$$

We now substitute equation (Chapter 1-4) into equation (Chapter 1-3) and write Φ_o as:

$$\Phi_o = P_w + P_{cow} - \rho_o g z \qquad \text{(Chapter 1-5)}$$

and the gradient of Φ_o along the length of the fault becomes:

$$(\nabla \Phi_o)_f = \left(\frac{dP_w}{dz} + \frac{dP_{cow}}{dz} - \rho_o g \right) \cos\theta \qquad \text{(Chapter 1-6)}$$

For an incompressible system and constant Q_o, S_o in the fault zone is constant. Therefore P_{cow} is constant and $\frac{dP_{cow}}{dz}$ is 0. Then equation (Chapter 1-6) becomes:

$$(\nabla \Phi_o)_f = \left(\frac{dP_w}{dz} - \rho_o g \right) \cos\theta \qquad \text{(Chapter 1-7)}$$

By substituting equation (Chapter 1-7) into equation (Chapter 1-2) , we have a general one-dimensional incompressible flow equation for the fault zone.

$$\frac{Q_o}{A} = \frac{k k r_o}{\mu_o} \left(\frac{dP_w}{dz} - \rho_o g \right) \cos\theta \qquad \text{(Chapter 1-8)}$$

Note that in a hydrostatic system $\frac{dP_w}{dz} = \rho_w g$ and equation (Chapter 1-8) reduces to:

$$\frac{Q_o}{A} = \frac{kkr_o}{\mu_o}\left(\rho_w - \rho_o\right) g \cos\theta \qquad \text{(Chapter 1-9)}$$

This was the approach used by Bennett (1996).

By solving equation (Chapter 1-8) for kr_o we can use the S_w-kr_o relationship to determine S_w, which then can be used in the S_w-P_{cow} relationship to determine P_{cow}. Then assuming that the sand is hydrostatic, the oil column height can be calculated as,

$$h_o = \frac{P_{cow}}{\left(\rho_w - \rho_o\right) \cdot g} \qquad \text{(Chapter 1-10)}$$

Using the input parameters (*Table Chapter 1-2*), equations above and the two sets of fault zone capillary pressure data (*Figure Chapter 1-3* and *Figure Chapter 1-4*), we calculate the oil column height versus water-phase pressure gradient (*Figure Chapter 1-7*). *Figure Chapter 1-7* illustrates two major points: 1) a dynamic water phase in the fault zone decreases oil column height and 2) knowledge of the fault zone oil-water capillary pressure relationship is important in predicting steady-state oil column height.

All equations have been presented in a form independent of units. A complete example of the steady-state analytical solution, with equations given in field units, is given in Appendix A.

Numerical Model Development

A series of four simulation runs were completed using a system with a 60 foot wide fault with two 50 foot thick sands attached to the hanging wall of the fault. The two sands were used to evaluate the effect of different boundary conditions at the end of the sands on steady-state column height. The lower sand was connected to a large aquifer, while the upper sand terminated at a no-flow boundary (see *Figure Chapter 1-8*). A summary of the input parameters used in the 4 runs is given in *Table Chapter 1-3*.

Table Chapter 1-3: 2-Phase Geo-Pressure Run Summary

Run	Water Phase Gradient	Capillary Pressure Data	Numerical Oil Column Height (ft)	Analytical Oil Column Height (ft)
1	geo-pressure 0.8 psi/ft	Thomeer	Upper sand 140 Lower sand 160	Both sands 166
2	hydrostatic	Thomeer	Upper sand 140 Lower sand 160	Both sands 168
3	geo-pressure 0.8 psi/ft	EPR	Upper sand 140 Lower sand 185	Both sands 329
4	hydrostatic	EPR	Upper sand 140 Lower sand 340	Both sands 669

The analytical and numerical results for Runs 1 and 2, which use capillary pressure data generated using Thomeer's relationship (*Figure Chapter 1-3*), are in excellent agreement for the lower sand which is attached to a large aquifer. A small decrease in column height is seen in the upper sand due to trapped (or perched) water increasing the water phase pressure in the sand and thereby not allowing additional oil to flow into the sand. Both the analytical and numerical results show little effect on column height due to water-phase pressure gradient in the fault.

The results for Runs 3 and 4, which use the EPR capillary pressure data, show a decrease in the numerical column height versus the analytical column height, in both the sands due to trapped water increasing the water phase pressure in the sand. The lower sand is connected to a large aquifer, allowing more oil to charge the sand, but the aquifer is not large enough or compressible enough to prevent the water pressure in the sand from increasing and limiting column height. *Figure Chapter 1-9* shows the difference in oil column height for Run 3 (geo-pressure) and Run 4 (hydrostatic) at 1 million years. Both the analytical and numerical results (*Table Chapter 1-3*) show a significant effect on column height due to water-phase pressure gradient in the fault.

The numerical model demonstrates again the importance of knowing the fault-zone oil-water capillary pressure relationship. The water saturation in the fault zone is a function of the water pressure gradient $\left(\frac{dP_w}{dz}\right)$ and oil flux $\left(\frac{Q_o}{A}\right)$ in the fault. The capillary pressure in the fault and at the fault/sand interface is a function of water saturation (S_w). *Figure Chapter 1-10* is a blow-up of the fault-zone capillary pressure curves over the fault-zone water saturation range used in Runs 1 through 4. Two significant observations can be seen in *Figure Chapter 1-10*. First, the analytical column heights are larger in Runs 3 and 4 because the capillary pressures are much higher than those for Runs 1 and 2. Second, in Runs 3 and 4 there is a larger difference in the geo-pressure and hydrostatic column heights because of the larger slope, $\left(\frac{dP_{cow}}{dS_w}\right)$, in the EPR capillary pressure curve. Therefore, for the same change in S_w, we have significant differences in the change in P_{cow} and consequently very different column heights.

Hydrocarbon column height in the sand is dependent on the fault-zone water pressure gradient, oil flux, and capillary pressure curve magnitude and slope.

The numerical model also illustrates the importance of the boundary conditions in the sand as can be seen in the difference in column height between the upper and lower sands in both the geo-pressure and hydrostatic simulations.

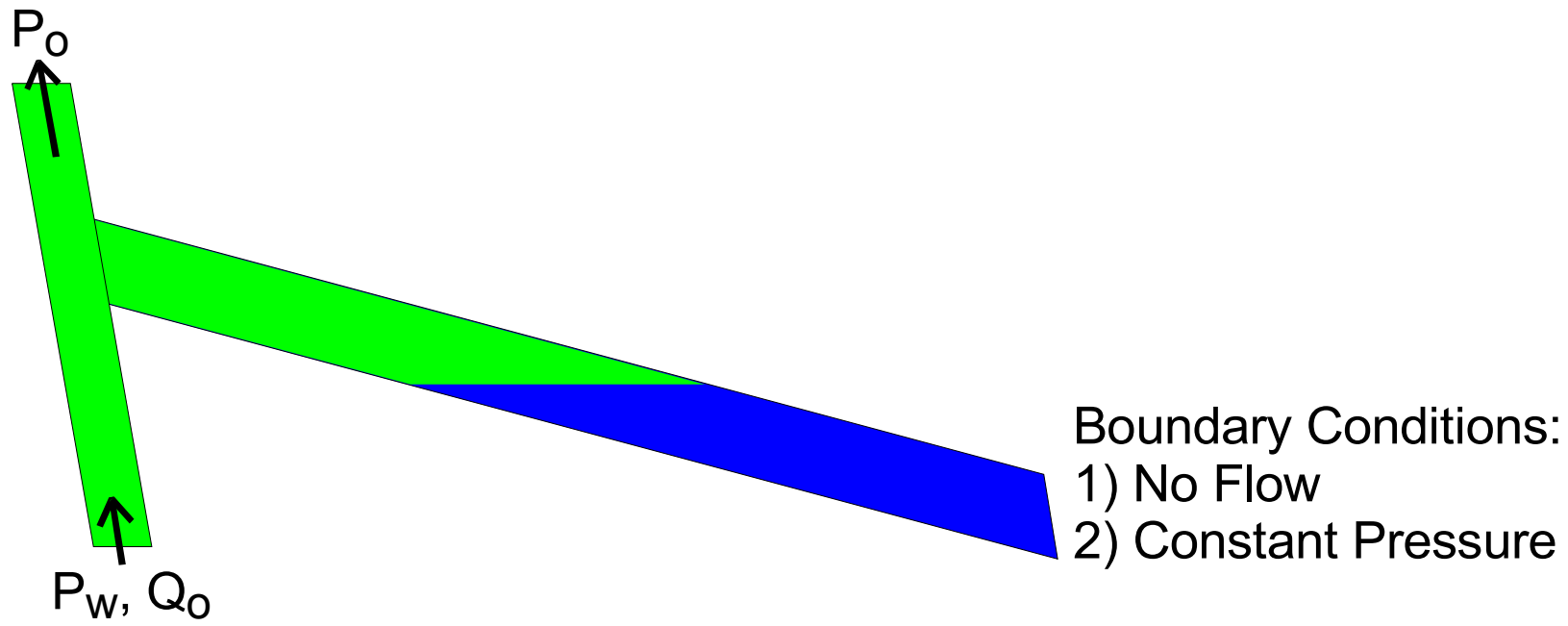

Figure Chapter 1-1: Schematic diagram of a geo-pressured fault/reservoir system with a constant oil phase pressure at the top of the fault, and a constant water phase pressure and constant oil flow rate at the bottom of the fault.

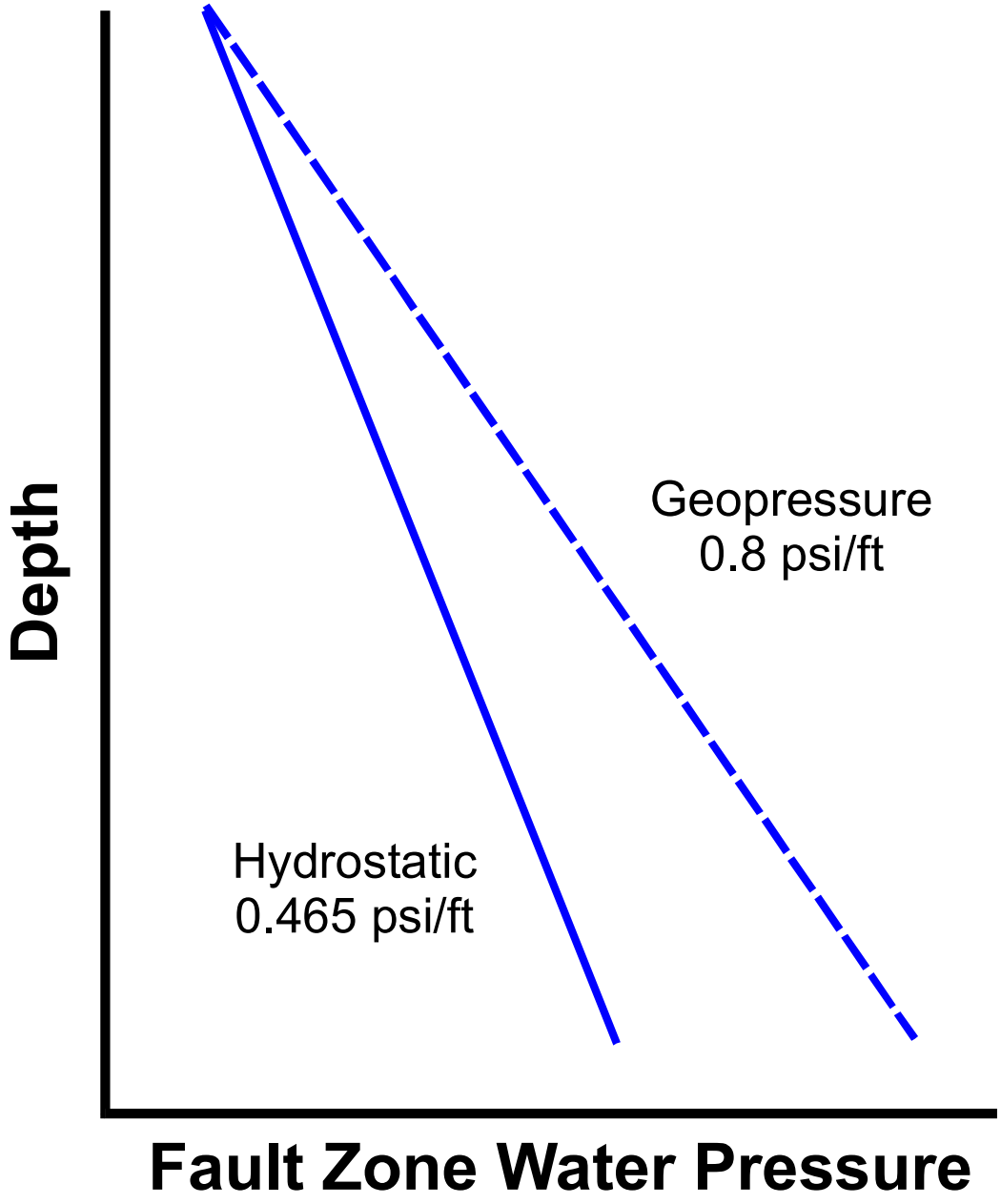

Figure Chapter 1-2: Fault-zone water pressure gradient geo-pressure model created by setting constant pressure boundaries at the top and bottom of the fault.

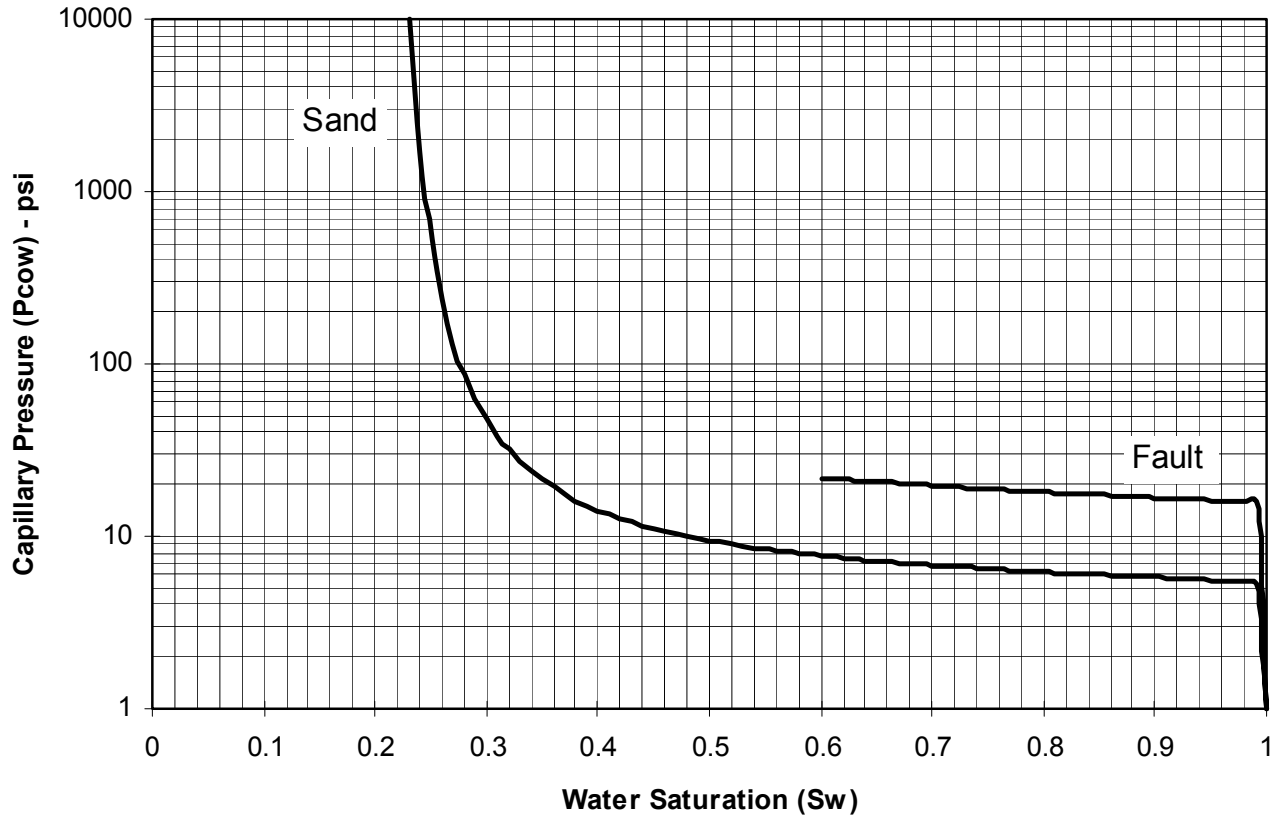

Figure Chapter 1-3: Oil-water capillary pressure verses water saturation using Thomeer's relationship (Jorden and Campbell, 1984) and input parameters given in Table 2-1.

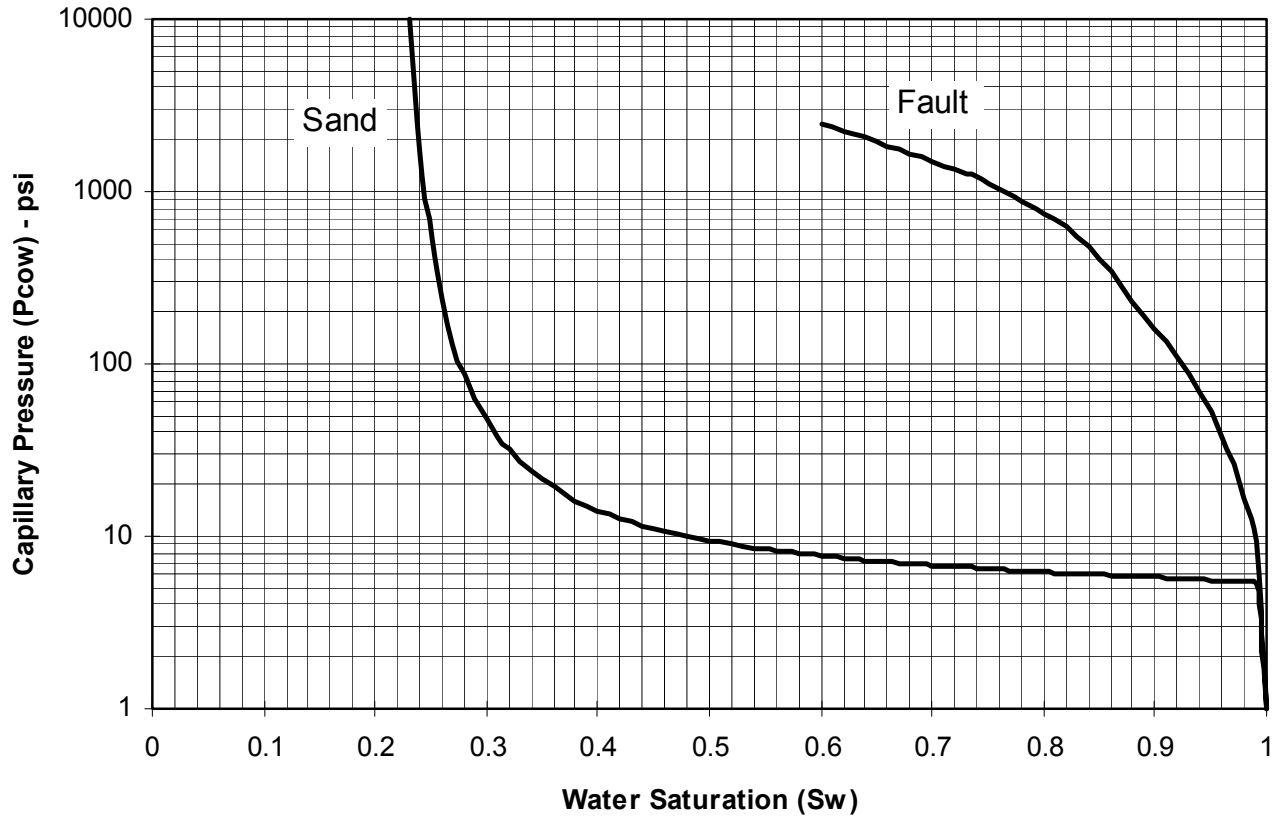

Figure Chapter 1-4: Oil-water capillary pressure versus water saturation using EPR data for the fault zone and Thomeer's relationship (Jorden and Campbell, 1984) with input parameters given in Table 2-1 for the sand.

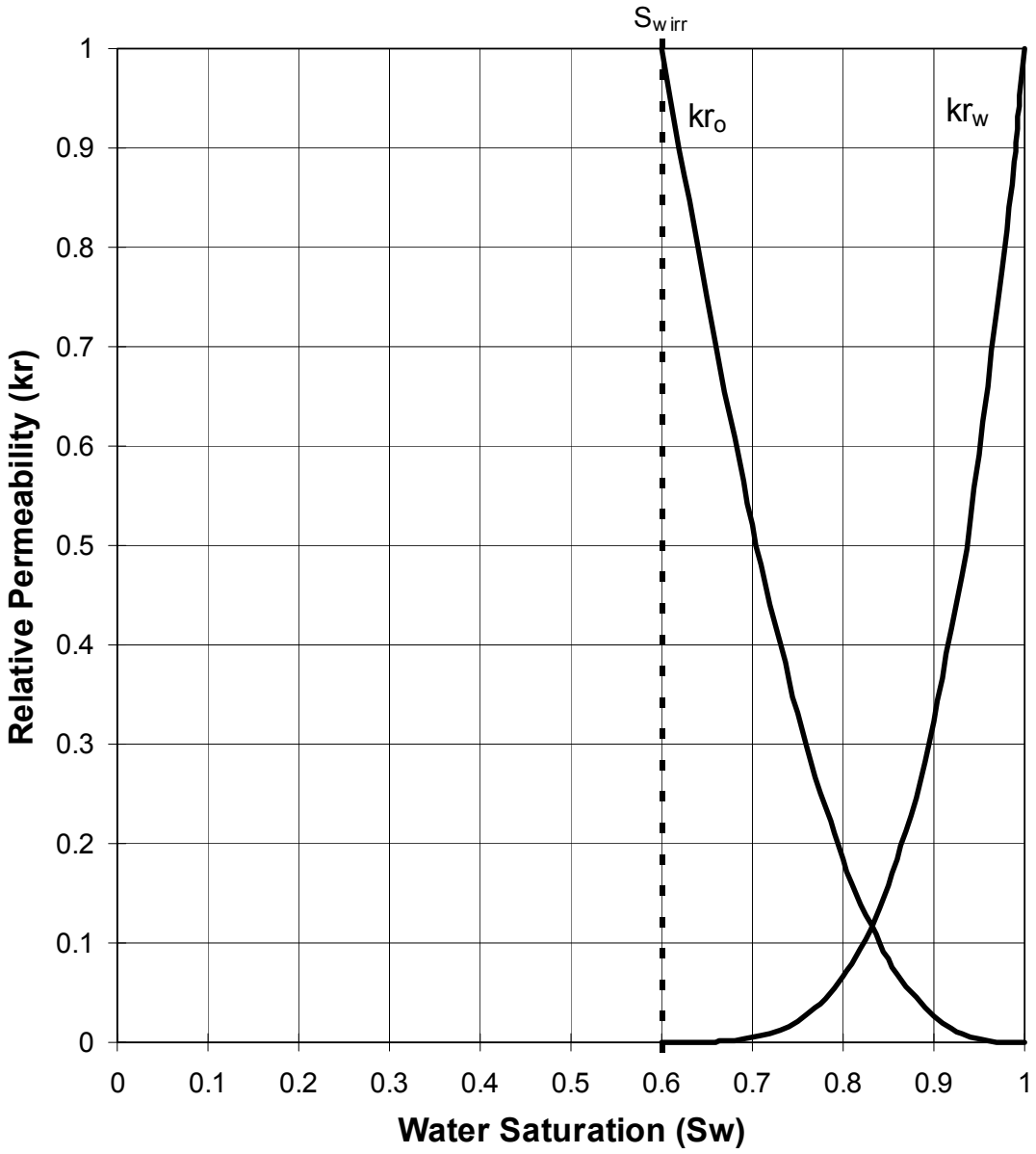

Figure Chapter 1-5: Fault-zone oil-water relative permeability using a S_{wirr} of 0.6.

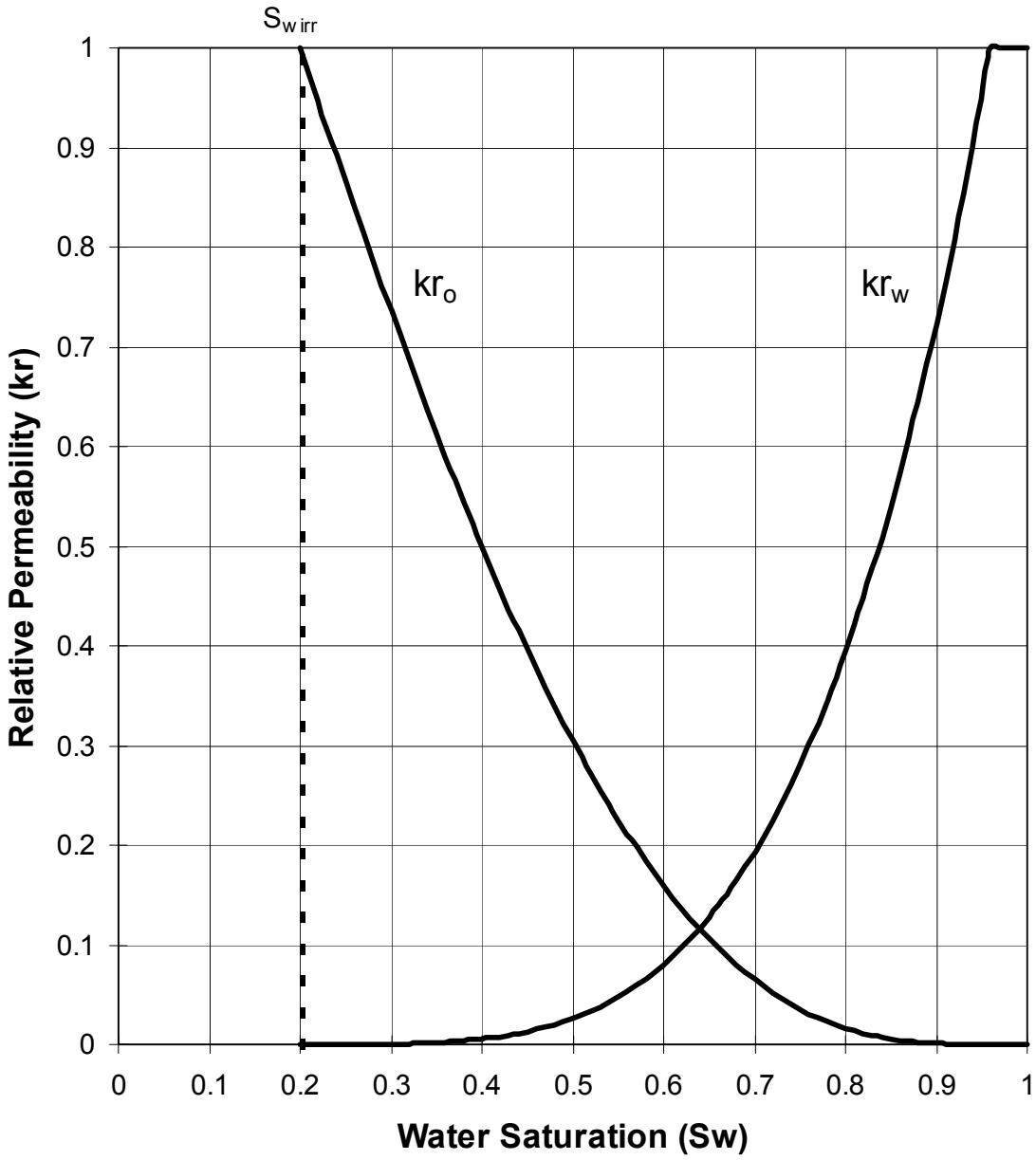

Figure Chapter 1-6: Reservoir sand oil-water relative permeability using a S_{wirr} of 0.2.

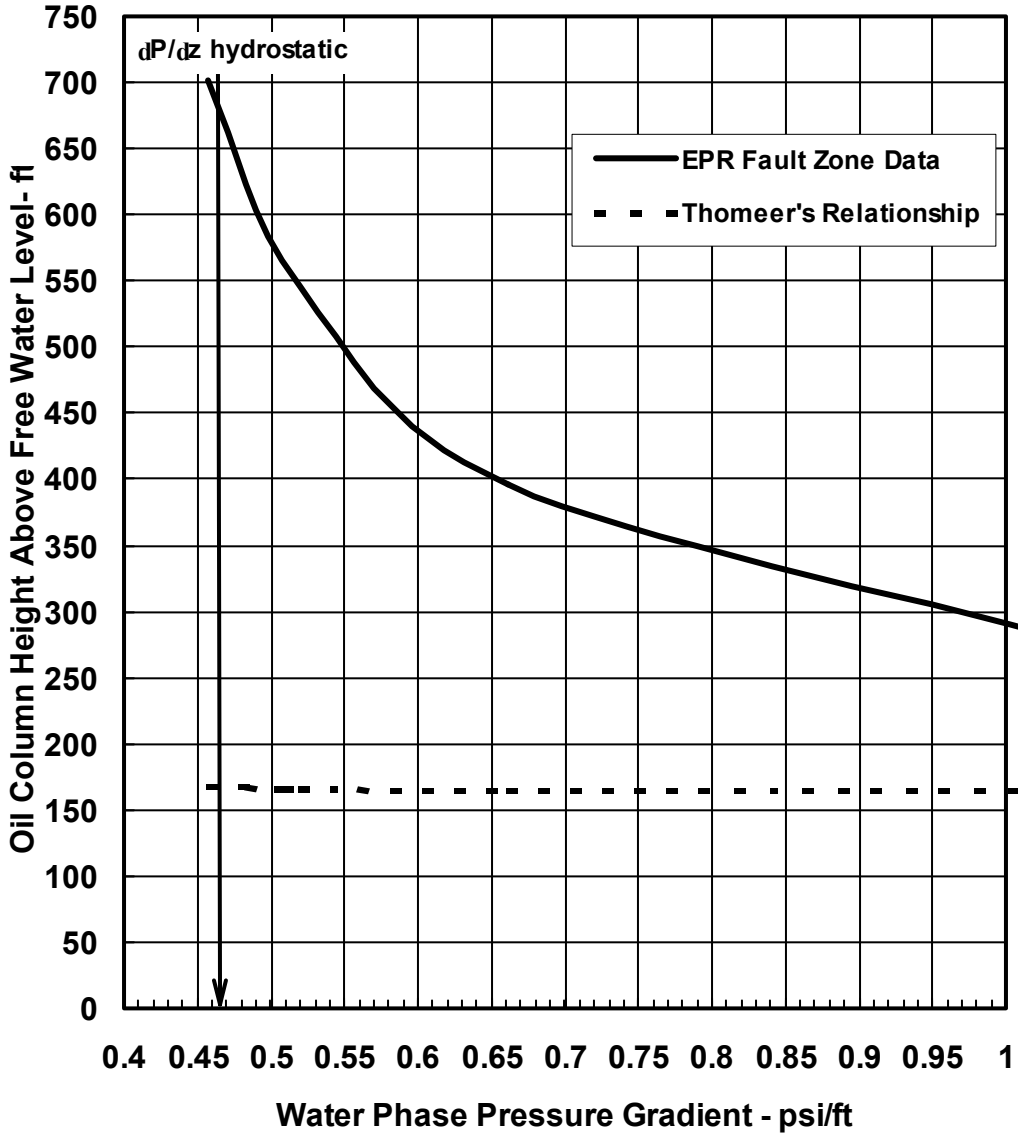

Figure Chapter 1-7: Oil column height versus water phase pressure gradient calculated from equations (Chapter 1-8) and (Chapter 1-10)

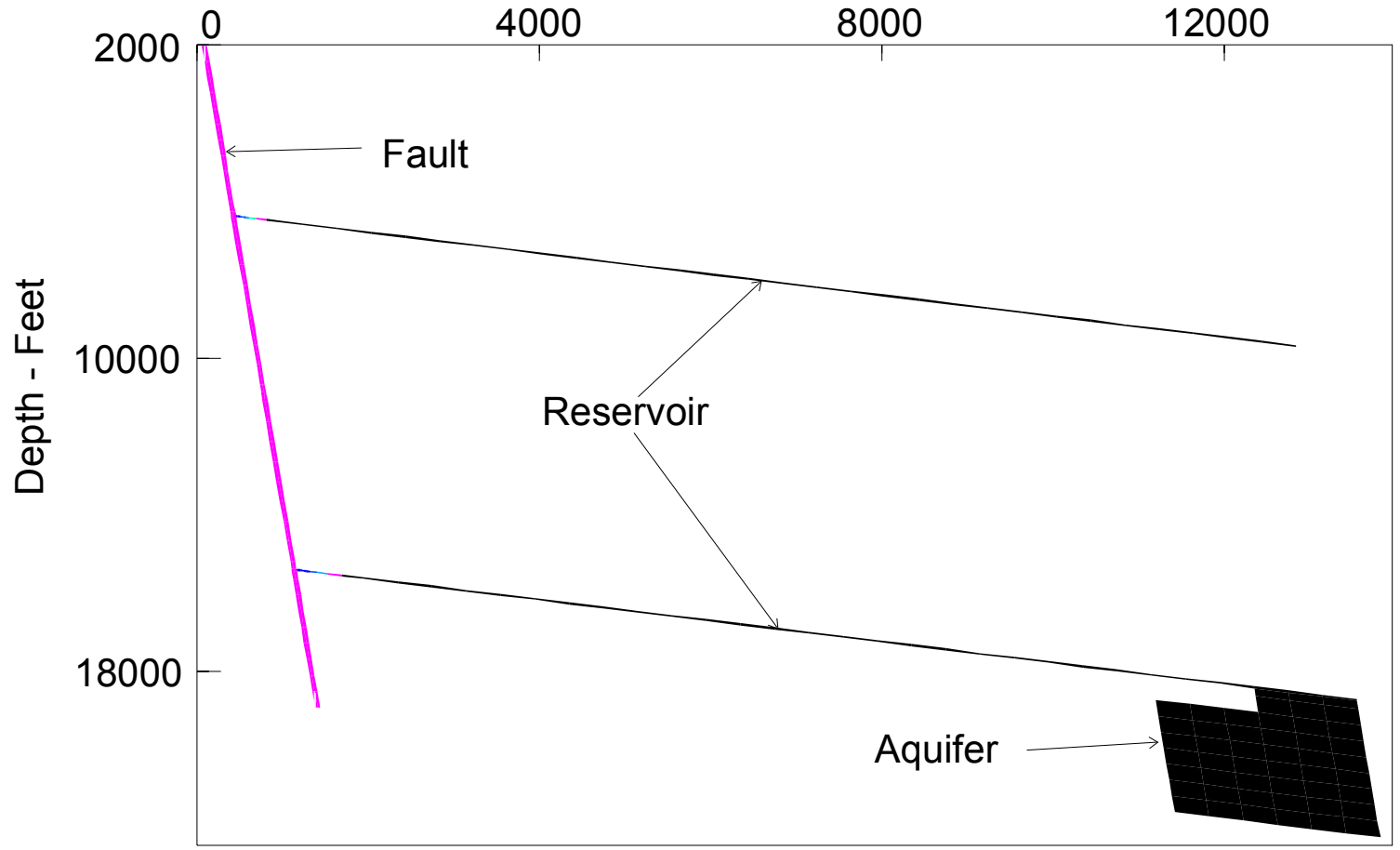

Figure Chapter 1-8: Geo-pressure simulation grid structure with a no flow boundary at the end of the upper sand and a large aquifer connected to the lower sand.

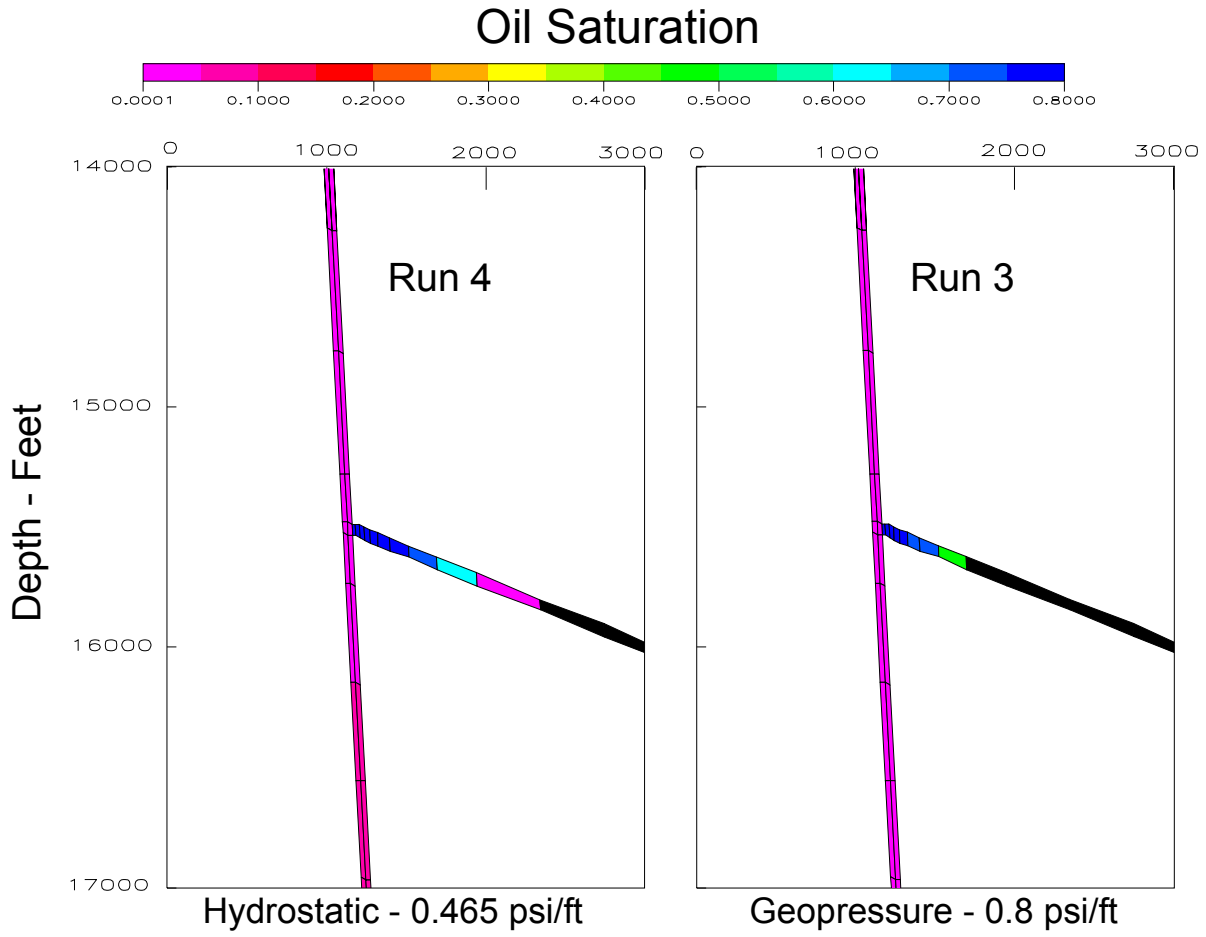

Figure Chapter 1-9: Oil saturation in the lower sand at 1 million years for a hydrostatic system and a system with a 0.8 psi/ft water phase pressure gradient in the fault, EPR capillary pressure model.

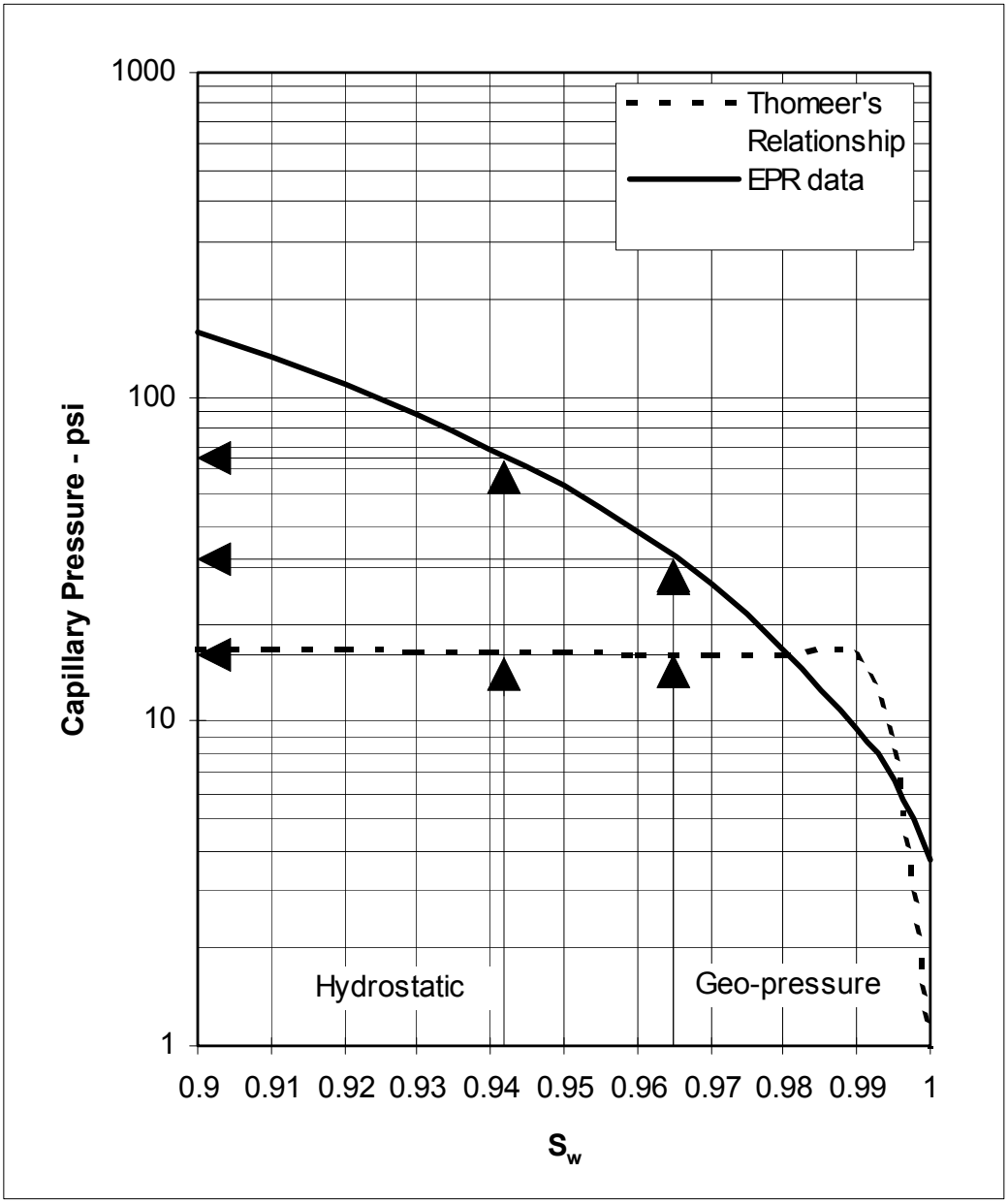

Figure Chapter 1-10: Comparison of fault-zone capillary pressure using Thomeer's equation and EPR data for geo-pressure and hydrostatic systems

Chapter 3

OIL AND GAS DISTRIBUTIONS IN STACKED PAY RESULTING FROM THREE-PHASE MIGRATION IN FAULTS

MODEL OBJECTIVES

This work expands on the previous two-phase work in Chapter 2, and Bennett, 1996. We consider 3-phase systems where both oil and gas are migrating through the fault. The first task was to develop a 3-phase, steady-state analytical model which describes oil and gas saturations in the fault, and oil and gas column heights in the reservoir sands based on the fault-seal (capillary pressure) model. The second task was to develop a numerical model and compare fault saturations and hydrocarbon column heights in the reservoir to the analytical model results. Two sealing mechanisms (fault seal and anticlinal seal) were then evaluated with the numerical model.

MODEL CONSTRAINTS

The problem we consider from both an analytical and numerical perspective is illustrated in *Figure 3-1*. A fault is charged from below with both oil and gas. Pressure at the point of injection, the bottom of the fault, may be above the bubble point pressure. At pressures above the bubble point oil and gas migrate as a single phase and charge

sands in the proportions at which they are injected and in a manner similar to the previous 2-phase models. When the oil phase pressure drops below the bubble point pressure, gas begins being exolved from the oil. As a result the oil and gas migrate and charge adjacent sands as discrete phases.

The physical properties summarized in *Table 3-1* and *Table 3-2* are used for all 3-phase models. PVT data used for all 3-phase modeling was derived using correlations presented by Beggs and Robinson (1975) and Vasquez and Beggs (1980) for the oil phase and by McCain (1973) and Lee, et al. (1966) for the gas phase. Both the analytical and numerical models are isothermal and a temperature of 300^{o}F was used to generate the PVT data. Graphs of all PVT data are included as Appendix B.

Table 3-1: Rock Properties, 3-Phase Model

Rock Property	Permeability (horizontal)	Permeability (vertical)	Porosity	Thickness	Width	Angle
Fault	0.017 md	0.017 md	15 %	60 ft	120 ft	10^{o} Anticline 5^{o} Fault Seal
Reservoir	1.0 md	1.0 md	20 %	50 ft	120 ft	variable

Table 3-2: Fluid Properties, 3-Phase Model

Fluid Properties (at standard conditions)	Water	Oil	Gas
Density	67.0 lb/ft3	53.05 lb/ft3	0.06109 lb/ft3
Viscosity	1.084 cp	0.8951 cp	0.0138 cp

Figure 3-2 presents the fault zone and reservoir sand oil-gas capillary pressure data used for all 3-phase models. These were scaled from the oil-water capillary pressure data (EPR) using the Levertt-J function (Amyx et al., 1960). Two-phase oil-water

capillary pressure (EPR) and oil-water relative permeability as a function of water saturation are the same as those used in the 2-phase models (see *Figures 2-4, 2-5*, and *2-6*). Two-phase oil-gas relative permeability as a function of gas saturation at connate water saturation (the water phase is present at irreducible saturation) are shown in *Figure 3-3* and *Figure 3-4* for the reservoir and fault, respectively. Three-phase oil relative permeability as a function of water saturation and gas saturation are calculated using the Modified Stone I Model (Aziz and Settari, 1979). The resulting 3-phase oil relative permeability for the reservoir and fault are show in *Figure 3-5* and *Figure 3-6*, respectively.

ANALYTICAL MODEL DEVELOPMENT.

We begin by considering steady-state flow within a hydrostatic fault. For the oil phase, the flux is driven by gravity and is proportional to the relative and intrinsic permeability and the potential gradient as in equation (3-1):

$$\frac{Q_o}{A} = \frac{k \cdot kr_o \cdot \left(\rho_w - \rho_o\right) \cdot g \cdot \cos\theta}{B_o \cdot \mu_o} \qquad (3\text{-}1)$$

This is the same as equation 1-12 except for the addition of the oil formation volume factor (B_o) term which accounts for the oil compressibility and mass transfer effects. The gas flux can be expressed as the sum of the free gas flux and solution gas flux as in equation (3-2) :

$$\frac{Q_g}{A} = \frac{k \cdot kr_g \cdot \left(\rho_w - \rho_g\right) \cdot g \cdot \cos\theta}{B_g \cdot \mu_g} + \frac{Rs_o \cdot k \cdot kr_o \cdot \left(\rho_w - \rho_o\right) \cdot g \cdot \cos\theta}{B_o \cdot \mu_o} \qquad (3\text{-}2)$$

We now consider the case of *Figure 3-1* and calculate the fault zone oil and gas saturations. Unlike the incompressible systems investigated in the 2-phase modeling where saturations in the fault are constant, the oil and gas properties in equations (3-1) and (3-2) are a function of pressure and consequently the phase saturations are a function of pressure. Therefore, equation (3-1) and equation (3-2) must be solved for a specific depth within the fault. Because many of the values in equations (3-1) and (3-2) are functions of pressure, the equations must be solved iteratively. The following paragraphs describe the steps to complete one iteration. One of two procedures is used depending on whether the fluids are above ($P>P_b$) or below ($P<P_b$) the bubble point pressure. When the fluid pressures are above the bubble point only two phases (oil and water) are present and when the pressure drops below the bubble point, gas has come out of solution and three phases (oil, gas, and water) are present. The solution procedure for each case is outlined below and a detailed example for when the system pressure is below the bubble point (3-phase) is included as Appendix C.

First we will determine oil saturation (S_o) for a system at a depth below the bubble point. Below the bubble point the problem is similar to the two-phase case. First we must estimate an oil phase pressure (P_o) corresponding to the depth. A good first approximation would be the water phase pressure (P_w) which is hydrostatic. Then from the PVT tables in Appendix B, we determine values for B_o, μ_o, and ρ_o. Given Q_o, A, k, and ρ_w, we can use equation (3-1) to calculate kr_o. We next refer to the 2-phase oil-water

relative permeability curve to determine S_w. We then refer to the oil-water capillary pressure curve to determine the oil-water capillary pressure (P_{cow}). The new oil phase pressure is $P_o = P_w + P_{cow}$. We then repeat the process until P_o no longer changes. Since the oil phase properties are weak functions of pressure when the pressure is above the bubble point, only a few iterations are needed for convergence.

We next consider the case of a depth above the bubble point ($P<P_b$). The solution becomes more complicated for 3-phase flow for two reasons: 1) the oil parameters, B_o, μ_o, and ρ_o in equation (3-1) are now strong functions of pressure and 2) kr_o is no longer a function only of S_w but a function of both S_w and S_g (see *Figure 3-6*). First we must estimate oil phase (P_o) and gas phase (P_g) pressures corresponding to the depth. A good first approximation for each would be the water phase pressure which is hydrostatic. Then from the PVT tables in Appendix B, we determine values for B_o, μ_o, ρ_o, B_g, μ_g, and ρ_g. Given Q_o, A, k, and ρ_w, we can use equation (3-1) to calculate kr_o. Then given Q_g, we can use equation (3-2) to calculate kr_g. We next refer to the 2-phase oil-gas relative permeability curve (*Figure 3-4*) to determine S_g. In *Figure 3-6* we follow a constant S_g line to the appropriate kr_o curve and determine S_w. Then, $S_o=1-S_w-S_g$. We then refer to the oil-water capillary pressure curve to determine the oil-water capillary pressure and to the oil-gas capillary pressure curve to determine the oil-gas capillary pressure (P_{cog}). The new guesses for the oil and gas phase pressures are $P_o = P_w + P_{cow}$ and $P_g = P_w + P_{cow} + P_{cog}$, respectively. We repeat the process until P_o and P_g no longer change. Since the oil and gas phase properties are strong functions of pressure when the pressure is below the bubble point, several iterations may be needed for convergence. A

numerical example of this case is included as Appendix C. The oil and gas rates used in the example are much higher than those used in the numerical modeling. The rates used in the example were chosen to improve clarity of the graphical presentation.

The assertion that $P_g = P_w + P_{cow} + P_{cog}$ is predicated on the assumption that there is a continuous oil phase present. Blunt et al. (1995) demonstrate that even in 3-phase gas-oil-water systems where very little oil is present, the oil often forms a thin film between the gas and water phases. Furthermore, Blunt et al. (1995) present a means, based on the interfacial tensions between the three phases, for predicting the presence of this oil film.

Since we have continuous water, oil, and gas phases across the fault-reservoir interface, at steady-state conditions, P_w, P_o, and P_g within the reservoir and fault are in equilibrium at the fault-reservoir interface. By calculating the steady-state values for P_w, P_o, and P_g in the fault at the sand face, hydrocarbon column heights in the adjoining sand can be determined. *Figure 3-7* depicts the pressure distribution in a static hydrocarbon/water column where the pressure gradient is a function of fluid density and column height can be determined as follows in equations (3-3) and (3-4)

$$h_{gas+oil} = \frac{P_{cow}}{(\rho_w - \rho_o) \cdot g} \tag{3-3}$$

$$h_{gas} = \frac{P_{cog}}{(\rho_o - \rho_g) \cdot g} \tag{3-4}$$

NUMERICAL MODEL DEVELOPMENT

We chose to implement a boundary condition at the ends of the reservoir sands such that the water-phase pressure in the reservoir would be in equilibrium with the fault. The fault/sand geometries investigated in the 3-phase simulations were too complex to permit water-phase equilibrium to be achieved using directly connected grid blocks between the ends of the sands and the top of the fault. Therefore, three 3-phase runs made using a simple geometry (which would allow directly connected grid blocks) and various means of connecting the lower ends of the reservoirs to the fault were examined to determine the optimal means for achieving water phase equilibrium.

A base run for comparison was done using direct grid block connections. The second run was made using non-neighbor connections from the end of the sands to the top of fault. And a third run was made using non-neighbor connections from the sands to a column running parallel to the fault and connected to the fault at the top. The first and third runs produced similar results for sand charge rate and produced a column height in agreement with the steady-state analytical column height. In the second run, the sands continued to charge well beyond the time that the steady-state analytical column height had been reached. It was determined that non-neighbor connections should only be made between cells located at approximately the same depth. The third run allowed for more flexible gridding in the sands for subsequent simulations; therefore, the equilibration method used in the third run was used for all subsequent 3-phase simulations.

In all the simulation results presented below there is a "constant pressure" boundary condition imposed at the end of each reservoir sand. The constant pressure

boundary is modeled by adding `non-neighbor connections' (not shown in the figures) between the end of the sand and a column of cells running parallel to the fault (not shown in figures). The top of this column is connected to the top cell in the fault. This keeps the aquifer region of each sand in hydrodynamic equilibrium with the fault. Also, in all the simulations there is a well injecting oil and a well injecting gas at a constant rate at the bottom of the fault zone and there is a well producing with a constant bottom hole pressure specification at the top of the fault zone. The fault is one cell thick.

NUMERICAL MODEL RESULTS

Two 3-phase runs were made and are noted as Run 5 and Run 6. Both 3-phase runs consist of a 60 foot thick fault and three sands attached to the hanging wall side of the fault. In Run 5 the fault is inclined at an angle 10^{o} from vertical and the upper sand is sealed by the fault and the lower two sands have a rollover anticline structure (see *Figure 3-8*). In Run 6 the fault is inclined at an angle 5^{o} from vertical and all three sands are sealed by the fault (see *Figure 3-9*). The input data for the 3-phase simulations are summarized in *Table 3-3*. Results of the 3-phase numerical modeling are discussed below.

Table 3-3: Summary of 3-Phase Simulation Input Parameters

Run	Oil Flux STB/day/ft^2	Gas Flux MCF/day/ft^2	Injection Pressure psia	Seal Type
5	3.14×10^{-7}	4.49×10^{-7}	8600	Anticlinal
6	4.34×10^{-7}	9.92×10^{-7}	8450	Fault

Run 5: Anticlinal Model

The anticlinal model (Run 5) was run to investigate the sand charge rate for each fluid and the path that is followed to reach the steady state hydrocarbon column height in a combination fault seal/anticlinal system. The injected gas-to-oil ratio (GOR) was set to cause the bubble-point pressure to occur between the middle and lower sands. The theoretical steady-state hydrocarbon column height (measured from the highest point in the sand) for each sand was calculated as described above. A comparison of the analytical heights to the numerical is given in *Table 3-4* and is discussed below. Steady-state column heights based on capillary pressure are calculated at the sand/fault interface. The calculated heights then are added to the height of the anticline above the fault intercept to determine the analytical column heights for the anticlinal structures.

Figure 3-10, Figure 3-11, and *Figure 3-12* show oil in place and free gas in place versus time for the upper, middle and lower sands, respectively for Run 5. *Figure 3-13* through *Figure 3-16* present oil and gas saturation maps at times of 1, 4, 7, and 10 million years, respectively for Run 5. Note in the saturation figures that the vertical dimension of the sands have been expanded and "h_a" represents the analytical column heights.

Table 3-4: Comparison of Numerical and Analytical Column Heights, Run 5: Anticlinal Model

	Total Height (ft)		Gas Height (ft)	
Sand	Numerical	Analytical	Numerical	Analytical
Upper	2400	2431	390	29
Middle	3895	3563	1850	2020
Lower	3060	3183	250	0

The lower sand is an anticline structure and there is only an oil phase present in the fault at the sand interface. The high pressure drop at the sand/fault interface initially causes some gas to flash (come out of solution) and enter the sand. This gas quickly migrates to the top of the structure but does not exist in quantities sufficient to block oil flow. The difference in the analytical and numerical gas column heights shown in *Table 3-4* for the lower sand is a result of the flashed gas. *Figure 3-12* shows that the oil charges the lower sand at a relatively constant rate and reaches steady state at approximately 1.5 million years.

The middle sand is an anticline structure and there are separate oil and gas phases present in the fault at the sand interface. At steady state, P_w, P_o, and P_g will be in equilibrium between the fault and the reservoir at the fault-reservoir interface. The pressure of the oil and gas phases are determined by adding the oil-water capillary pressure to the water phase pressure and adding the oil-gas capillary pressure to the oil phase pressure, respectively. Initially the water saturation, S_w, in the sand is 1.0, the capillary pressures, P_{cow} and P_{cog} are 0.0 and $P_g=P_o=P_w$.. As oil and gas migrate the fault, water saturation, S_w, decreases and gas saturation, S_g, increases, increasing P_{cow} and P_{cog} respectively. This increases P_o and P_g within the fault and creates a driving force causing the oil and gas to charge the reservoir sand. Because P_{cow} is a function of S_w only, P_g is calculated from P_o, and $P_{cog} << P_{cow}$, we expect that almost all the oil and gas would charge the sand until S_w in the sand is such that, P_{cow} in the sand at the fault-sand interface approaches P_{cow} in the fault. Because the ratio of gas to oil flux (1.42 MCF/STB) in the fault is not the same as the ratio of gas to oil expected to be in place in

the sand (2.32 MCF/STB) at steady-state, one of the phases (in this case the oil phase) overcharges the reservoir. Then as P_{cow} in the sand approaches P_{cow} in the fault, the hydrocarbon phase which has overcharged the reservoir sand will begin to be expelled and will be replaced by the undercharged phase.

As the column height grows, gravity segregation occurs and the anticline above the fault interface should become gas saturated. As segregation occurs and a gas cap forms in the anticline, the oil in the leg opposite the fault is trapped and the oil in leg adjacent to the fault is displaced back into the fault (see *Figure 3-13* through *Figure 3-16*). Gas will continue to charge until the leg opposite the fault reaches equilibrium and residual oil saturation is reached in the adjacent leg. Note *Figure 3-13* through *Figure 3-16* show both the sands and fault to scale and a blowup of each sand so that the saturation distributions can be seen more clearly.

The upper sand is sealed only by the fault (capillary pressure). For reasons discussed above both fluids initially charge the sand. For this case of fault seal the gas initially overcharges the reservoir. *Figure 3-10* shows that at 3 million years the charge rate begins to decline for both fluids. By 4 million years the gas is no longer charging the sand and by 5 million years gas is being discharged by the sand. Through this time the oil continues to charge the sand and displace the gas. By 10 million years the steady-state total column height has almost been reached (*Figure 3-16*). However, the gas column height still exceeds the steady-state value and gas is being displaced by oil. *Figure 3-14* through *Figure 3-16* show that the gas height reaches a maximum at about 4 million years and then begins to recede leaving a residual saturation as an artifact of the

maximum height reached. Steady-state conditions were not reached in the upper sand in this simulation.

Run 6: Fault Seal Model

The fault seal model (Run 6) was run to investigate the effect of pressure (depth) on the hydrocarbon column height in a fault seal model where the sands have little or no rollover. The GOR for Run 6 was set to create a separate gas phase throughout the fault. A comparison of the analytical column heights to the numerical is given in *Table 3-5* and discussed below. *Figure 3-17, Figure 3-18,* and *Figure 3-19* show oil in place and free gas in place versus time in the upper, middle, and lower sands respectively for Run 6. *Figure 3-20* through *Figure 3-24* present oil and gas saturation maps at times of 2, 4, 10, 15, and 20 million years, respectively for Run 6.

Table 3-5: Comparison of Numerical and Analytical Column Height, Run 6: Fault Seal Model

	Total Height (ft)		Gas Height (ft)	
Sand	Numerical	Analytical	Numerical	Analytical
Upper	3025	3312	735	50
Middle	2990	2494	40	54
Lower	2235	1957	40	52

Because the physical properties (B, μ, and ρ) and the mass flux (due to solution gas traveling with the oil phase) of the oil and gas phases are strong functions of pressure, the oil (S_o) and gas (S_g) saturations within the fault zone change as the hydrocarbons migrate up the fault. As the fluids migrate up the fault, the pressure decreases. This causes gas traveling in the oil phase to come out of solution and causes expansion of the free gas. This in turn causes the gas saturation within the fault to

increase. Even though the mass traveling in the oil phase decreases as the oil migrates up the fault, the oil phase saturation increases. This is due to the increase in viscosity and density of the oil phase as gas is evolved from the oil.

The decrease in pressure as we move up the fault also effects the hydrocarbon column height. For systems at pressures below the bubble point, ρ_o increases as pressure decreases (because of the gas coming out of solution). Therefore, the effect on column height for the oil phase will always be an increase as both S_o (P_{cow}) and ρ_o increase as the oil migrates up the fault (see equation (3-3)). The effect on column height is very small for the gas phase and gas column height can either increase or decrease depending on the shape of the oil-gas capillary pressure curve. This is a result of offsetting effects of the increase in S_g (see equation (3-2)) and P_{cog} causing an increase in column height against the decrease in ρ_g (equation (3-4)) causing a decrease in column height.

For systems at pressures above the bubble point, there is only oil phase present. The effect on column height of the oil phase above the bubble is analogous to the effect on column height of the gas phase below the bubble point pressure.

Since there is free gas present in the fault we expect both free gas and oil to charge the reservoir sands. Additionally, since the analytical gas column height predicted for each of the three sands is small, we would expect the gas phase to overcharge the sands and subsequently be displaced by the oil phase. We see this happening as all three sands initially are charged with gas and oil (*Figure 3-20*). The lower, middle and upper sands begin discharging gas at 2 (*Figure 3-19*), 4 (*Figure 3-18*), and 4.5 (*Figure 3-17*) million years, respectively.

From 2 million years to 7 million years the lower sand continues to charge with oil and discharge the excess gas (*Figure 3-19*). By 7 million years the lower sand has reached steady state and the numerical column heights are in agreement with those calculated analytically (*Table 3-5*). Similarly, from 4 million years to 20 million years the middle sand continues to charge with oil and discharge excess gas (*Figure 3-18*). By 20 million years the middle sand has reached steady state and the numerical column heights are in agreement with those calculated analytically (*Table 3-5*).

Gas begins to be expelled from the upper sand at 4.5 million years, shortly after gas has begun to be expelled from the middle sand. The upper sand does not reach steady state in the simulation. We can see by the slope of the gas in place curves in *Figure 3-17* through *Figure 3-19* during the gas expulsion time period that as we move up the column, the gas is expelled more slowly. As gas is discharged from lower sands, there is a temporary increase in gas flux in the fault above that sand and consequently an increase in the gas saturation within the fault above that sand (*Figure 3-25*) causing overcharging of the shallower sands. This causes the maximum transient gas column height to increase as we move up the fault (see *Figure 3-21*). The presence of a gas cap within the sand limits the oil charge rate by decreasing kr_o increasing the distance the oil must migrate at a low kr_o.

As previously mentioned, all the modeling is isothermal, and temperature changes, as the oil and gas migrate up the fault, would also effect density and viscosity of the fluids.

IMPLICATIONS OF 3-PHASE FAULT SEAL MODEL

Two major observations can be drawn from the 3-phase fault seal model:

1. For constant oil and gas flux rates within the fault, depth has only a small effect on steady-state gas column height and steady-state oil column height will decrease with increasing depth.
2. Transient effects can lead to the presence of significant gas columns which are not predicted by the steady-state analytical model. The column heights will eventually go to steady state, but it will take a long time. Furthermore, transient gas column height will be higher in shallow sands as oil charges the lower sands and gas is flushed out.

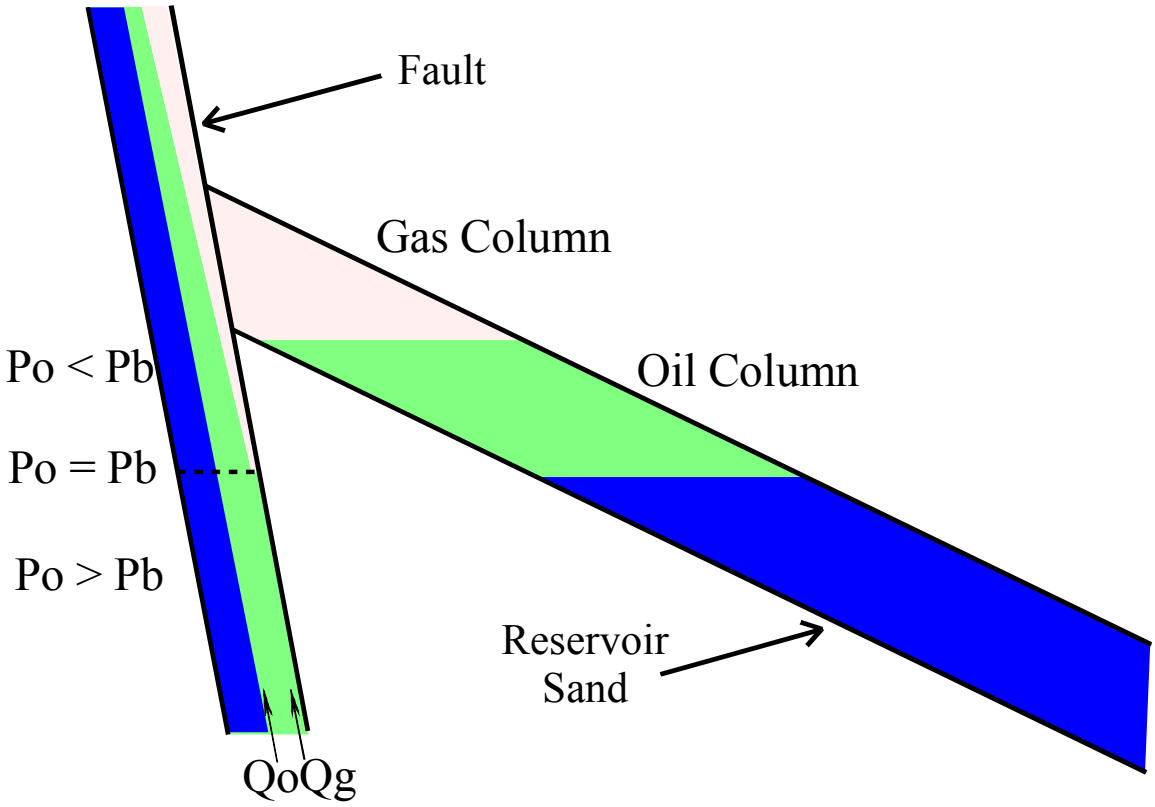

Figure 3-1: 3-Phase migration schematic. Po = oil phase pressure and Pb = bubble point pressure. Below the bubble point pressure, a discrete gas phase is present.

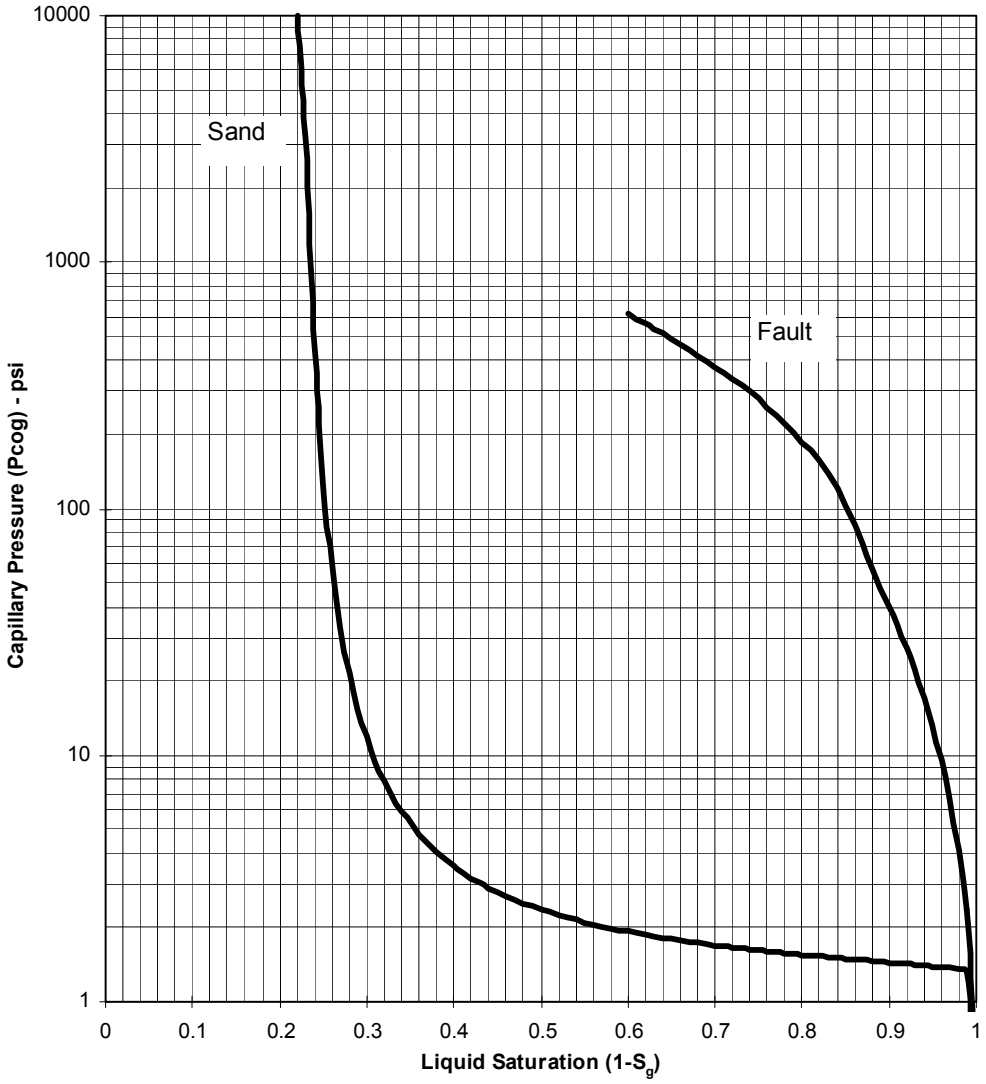

Figure 3-2: Oil-gas capillary pressure scaled by multiplying the oil-water capillary pressure, *Figure 2-4*, by the ratio the oil-gas interfacial tension (5 dynes/cm) to the oil water interfacial tension (20 dynes/cm).

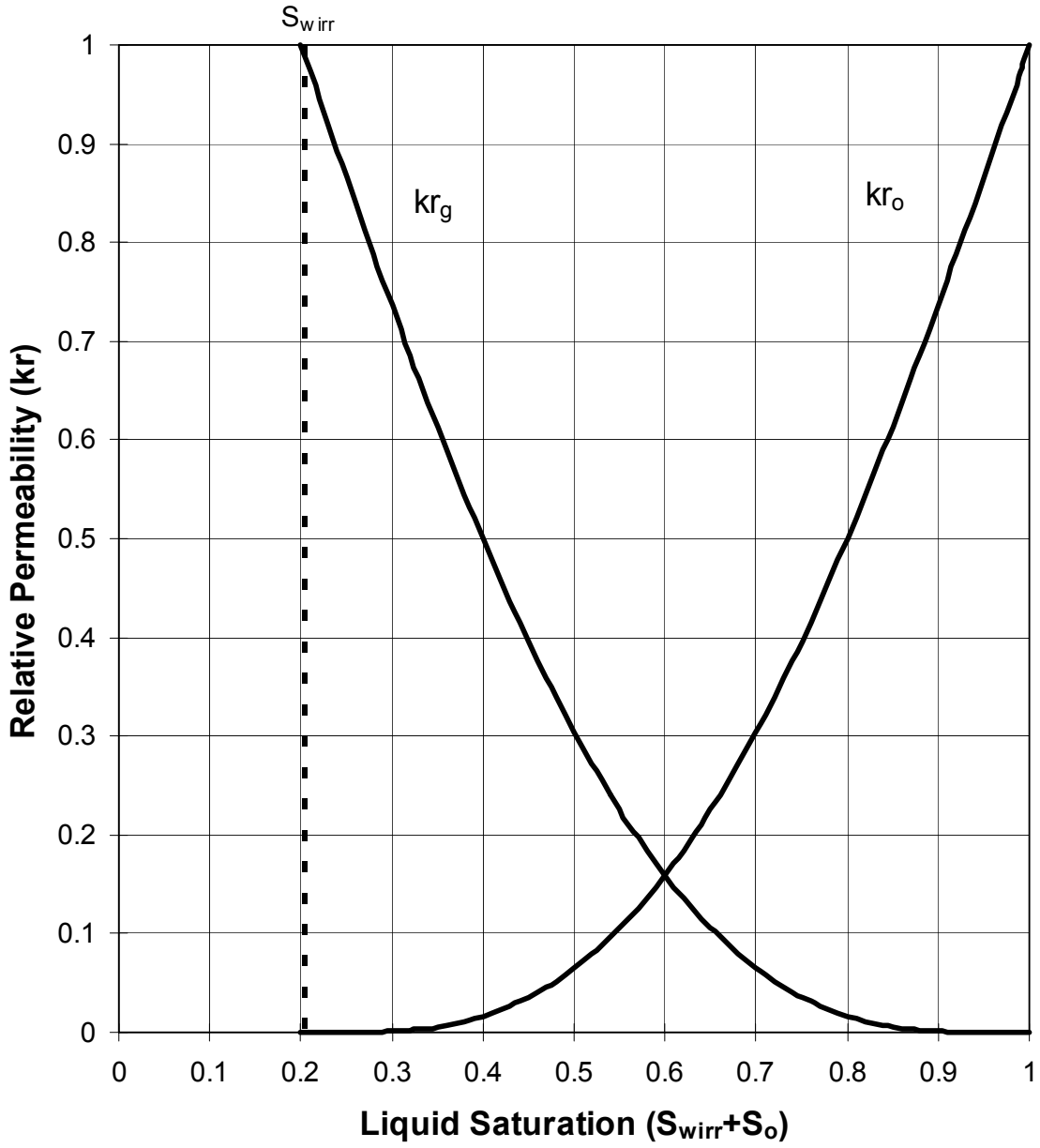

Figure 3-3: Reservoir sand 2-phase oil-gas relative permeability at irreducible water saturation (S_{wirr}), assumed to be the same as the 2-phase oil-water relative permeability, *Figure 2-6*.

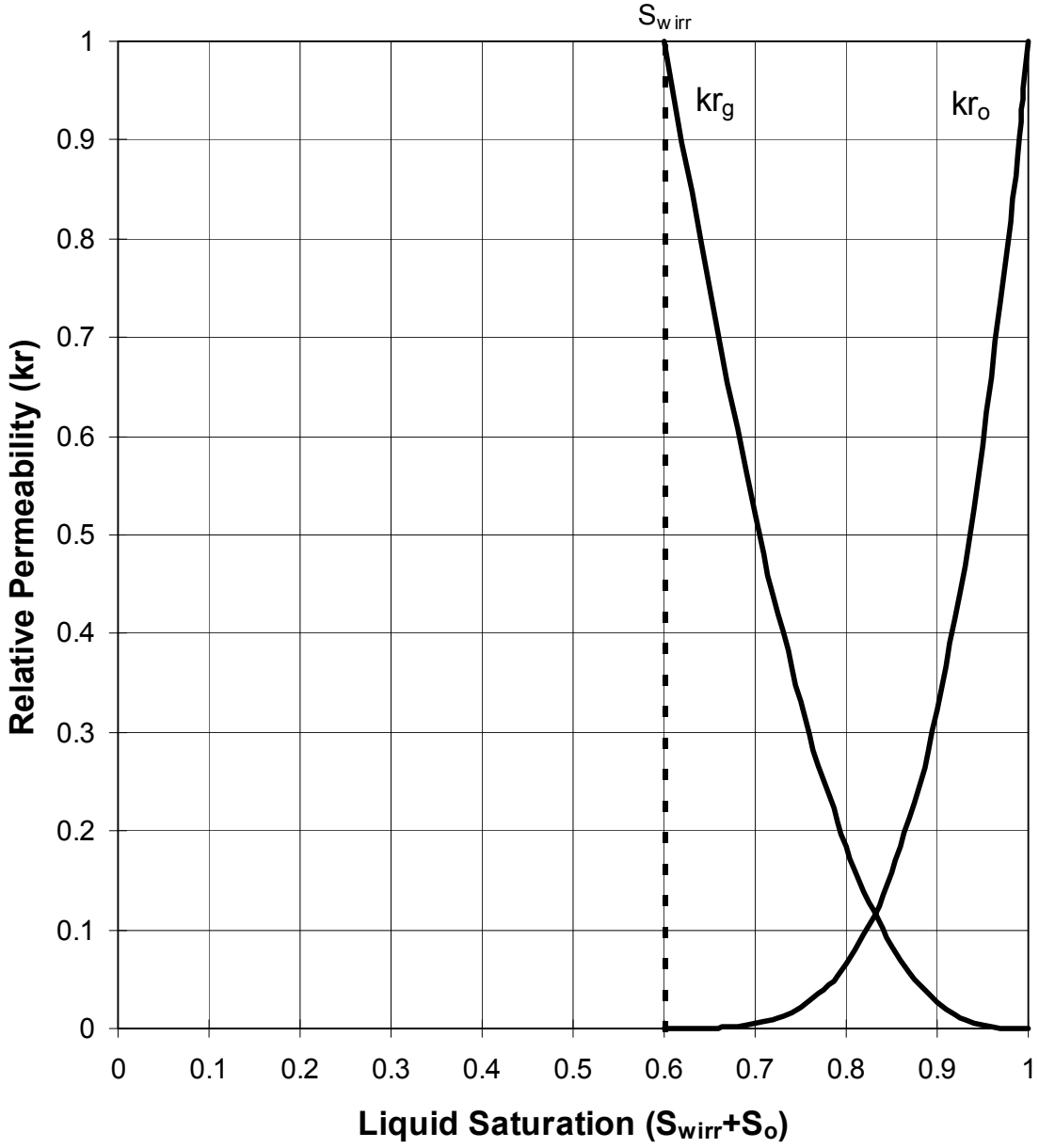

Figure 3-4: Fault zone 2-phase oil-gas relative permeability at irreducible water saturation (S_{wirr}), assumed to be the same as the 2-phase oil-water relative permeability, *Figure 2-5*.

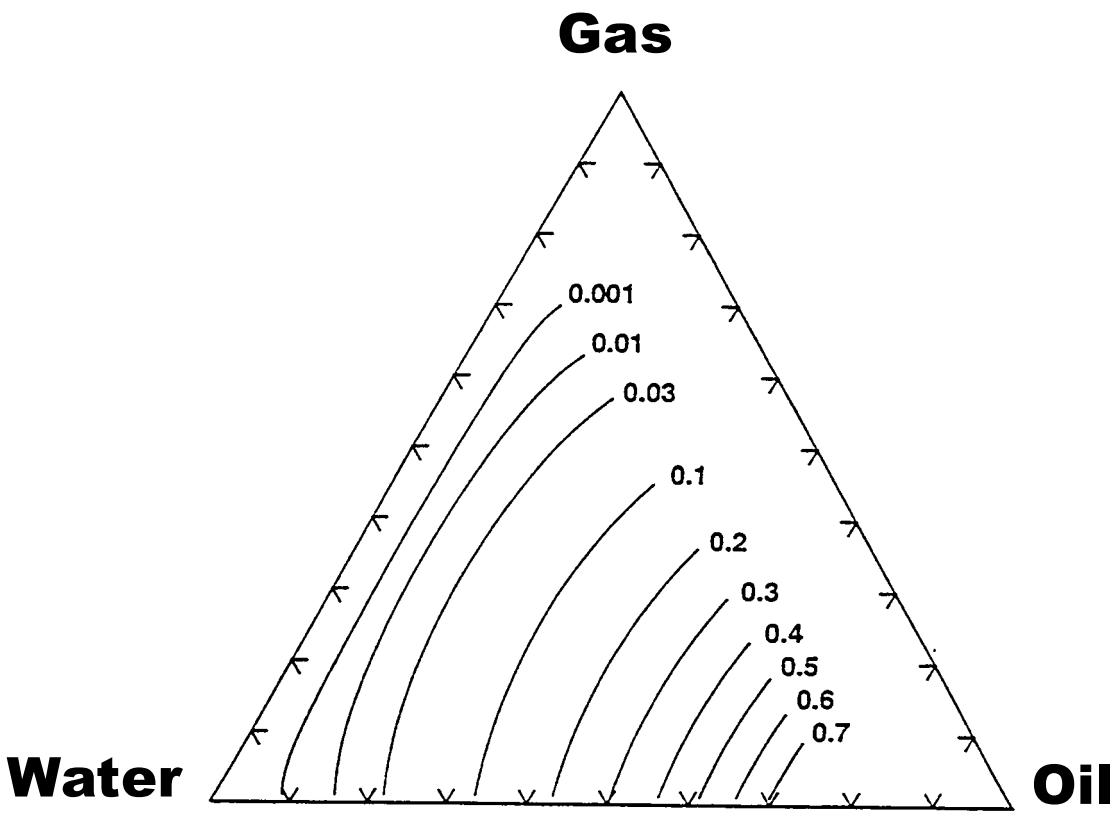

Figure 3-5: Reservoir sand 3-phase oil-gas relative permeability, Modified Stone I Model (Aziz and Settari, 1979).

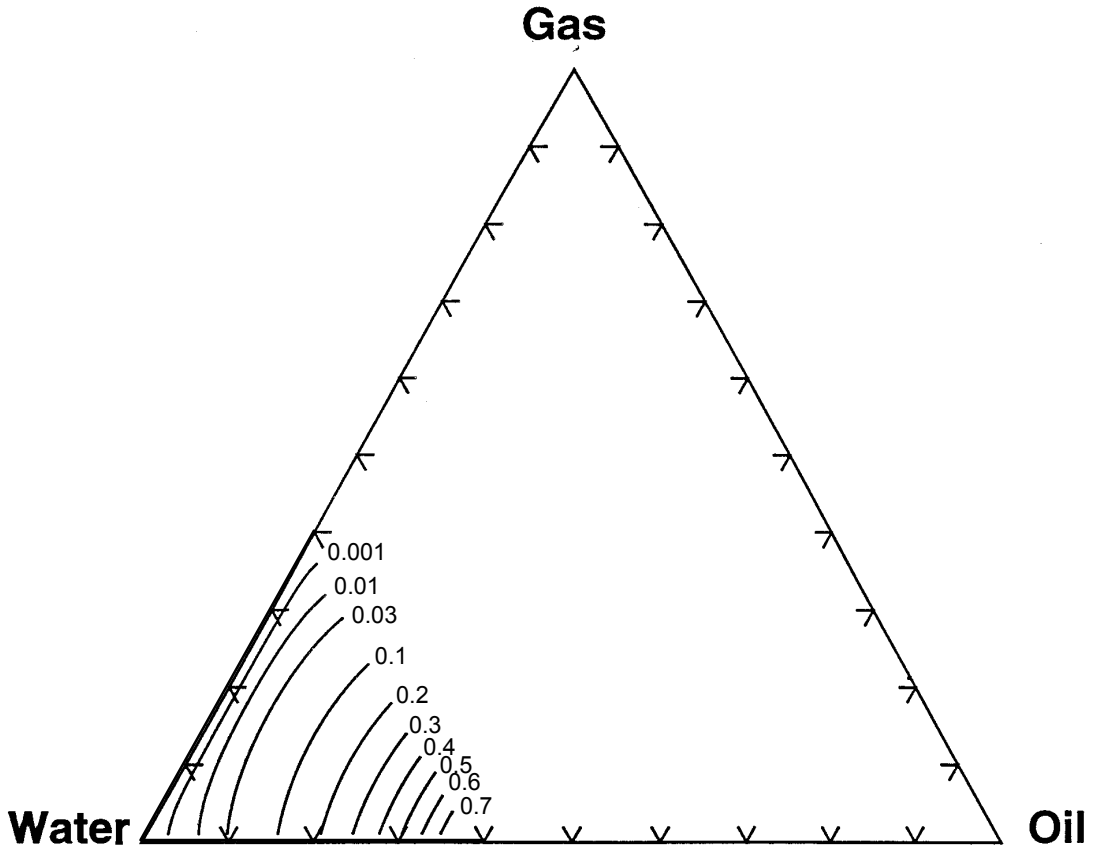

Figure 3-6: Fault zone 3-phase oil-gas relative permeability, Modified Stone I Model (Aziz and Settari, 1979).

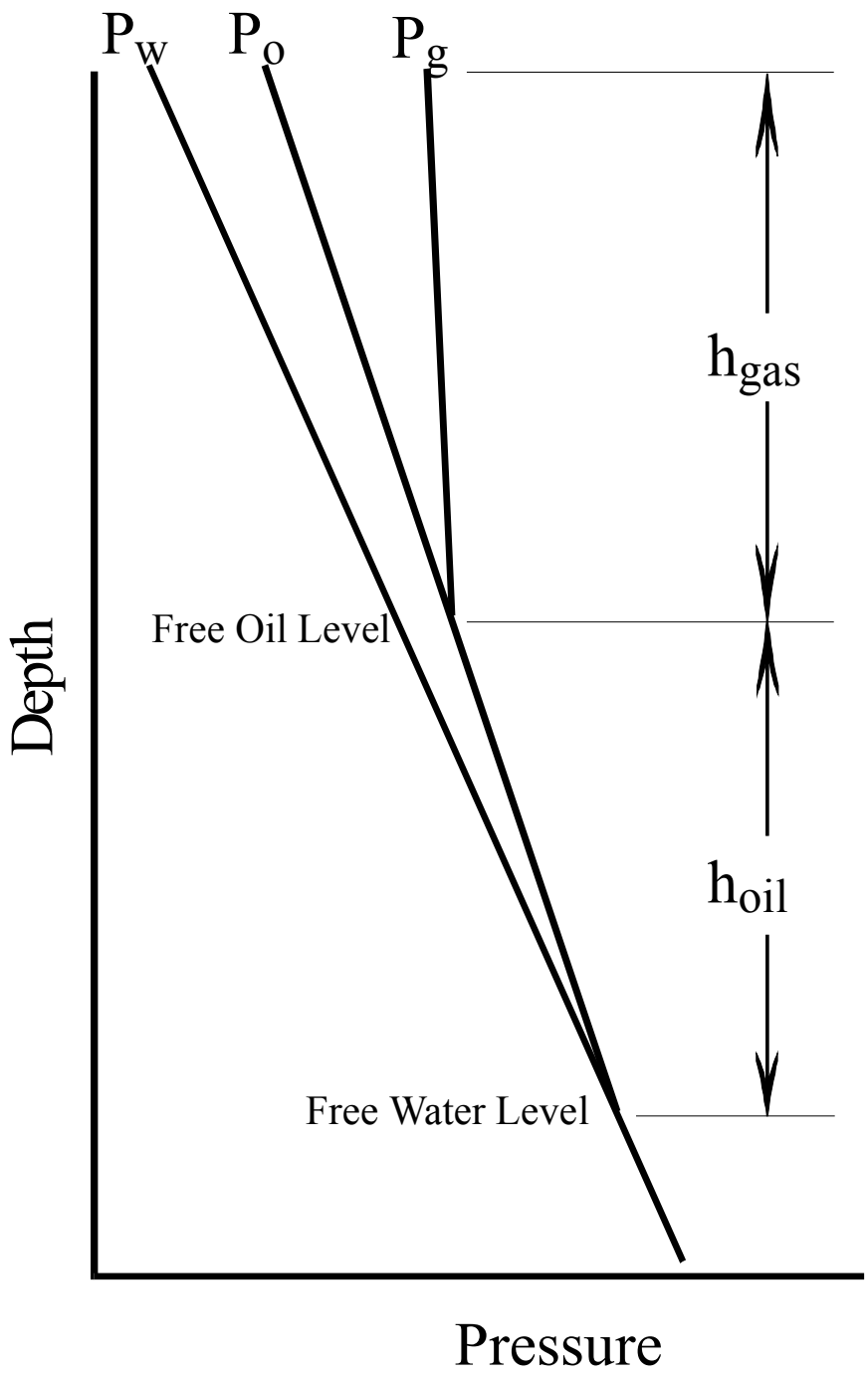

Figure 3-7: Fluid pressure in the reservoir sand vs. depth schematic for a 3-phase hydrostatic system.

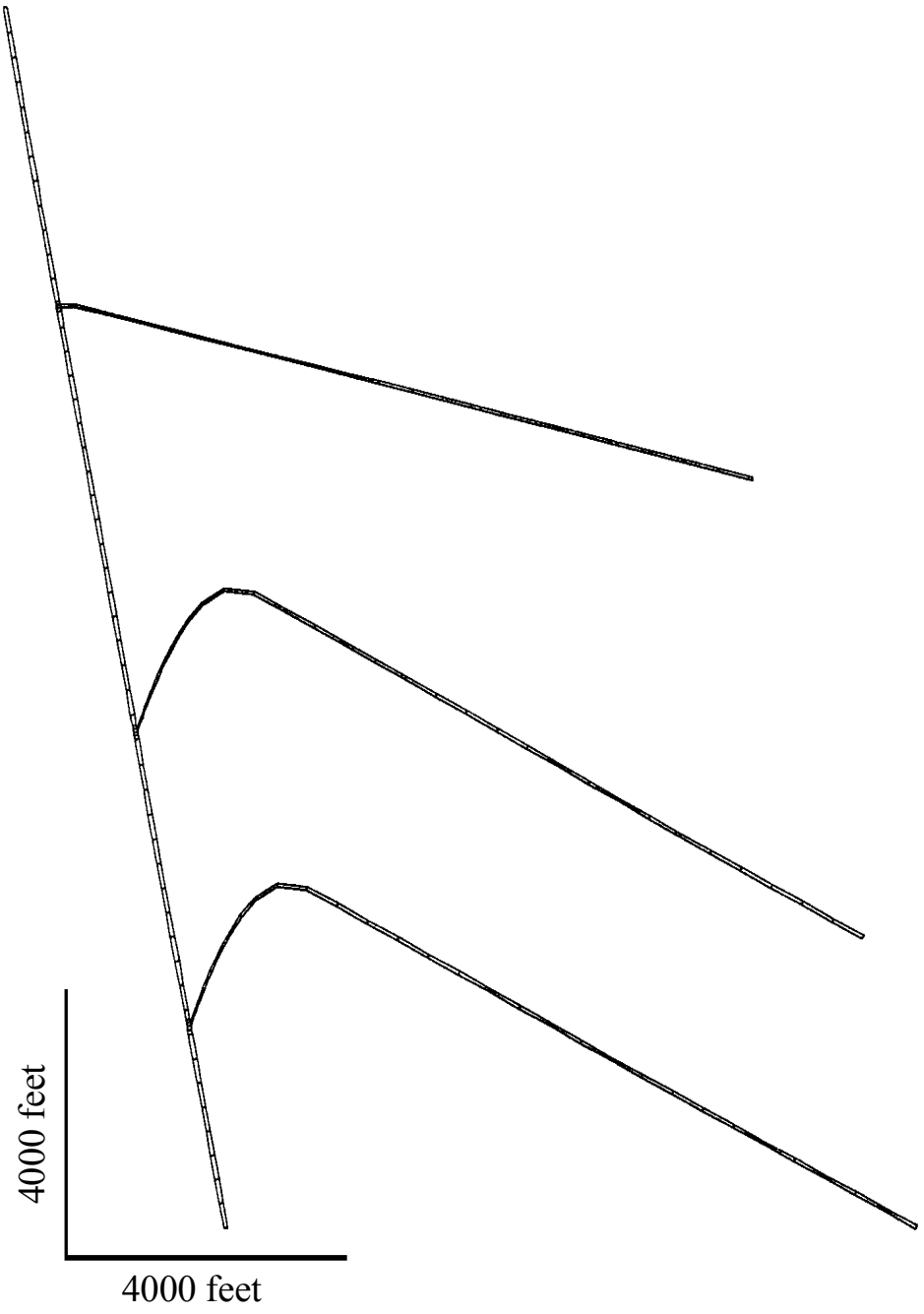

Figure 3-8: Anticlinal structure geometry (Run 5) where hydrocarbons are trapped by the anticline. The fault is 60 feet wide and the sand is 50 feet thick (see *Table 3-1*).

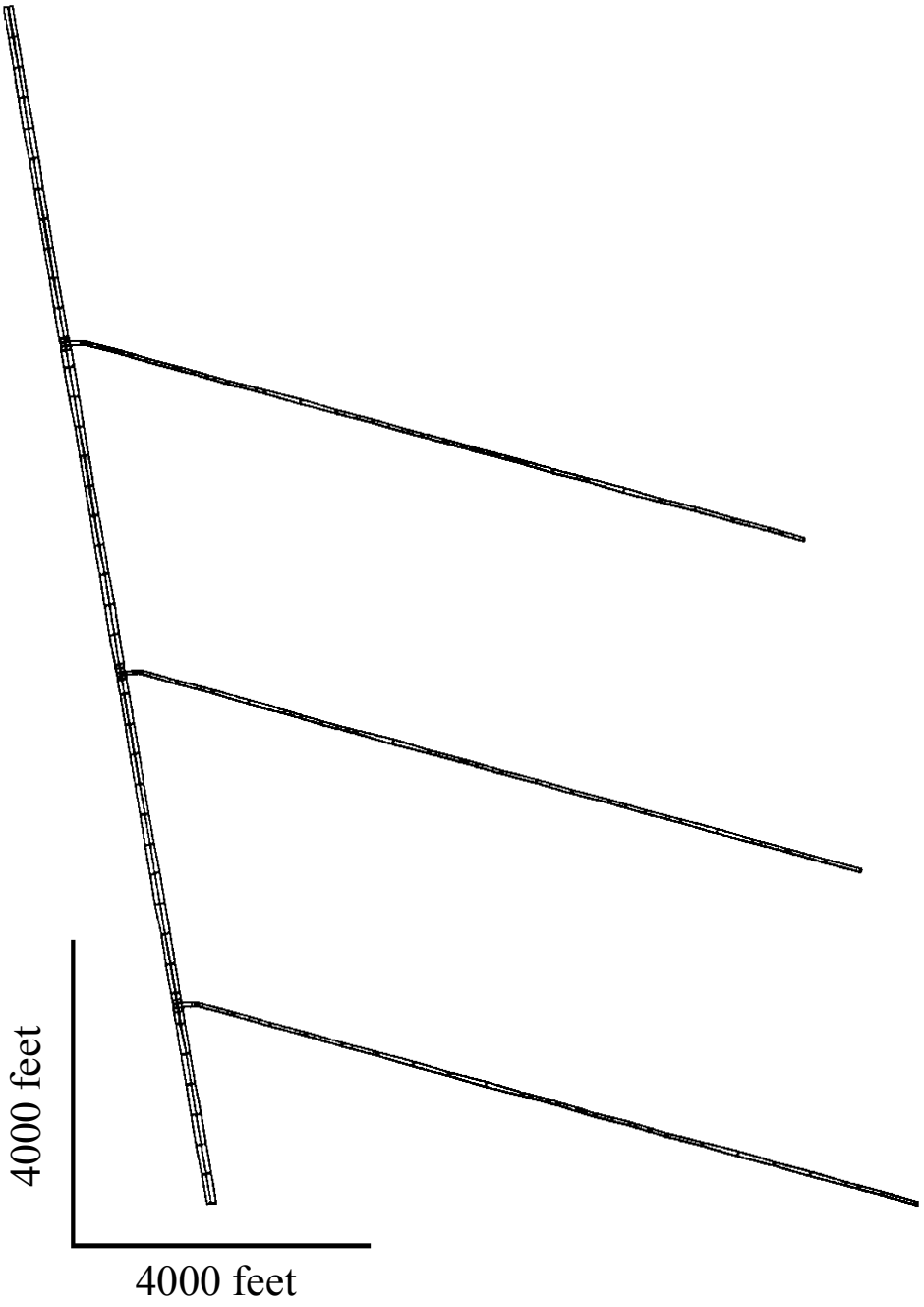

Figure 3-9: Fault seal geometry (Run 6) where hydrocarbons are trapped by capillary pressure. The fault is 60 feet wide and the sand is 50 feet thick (see *Table 3-1*).

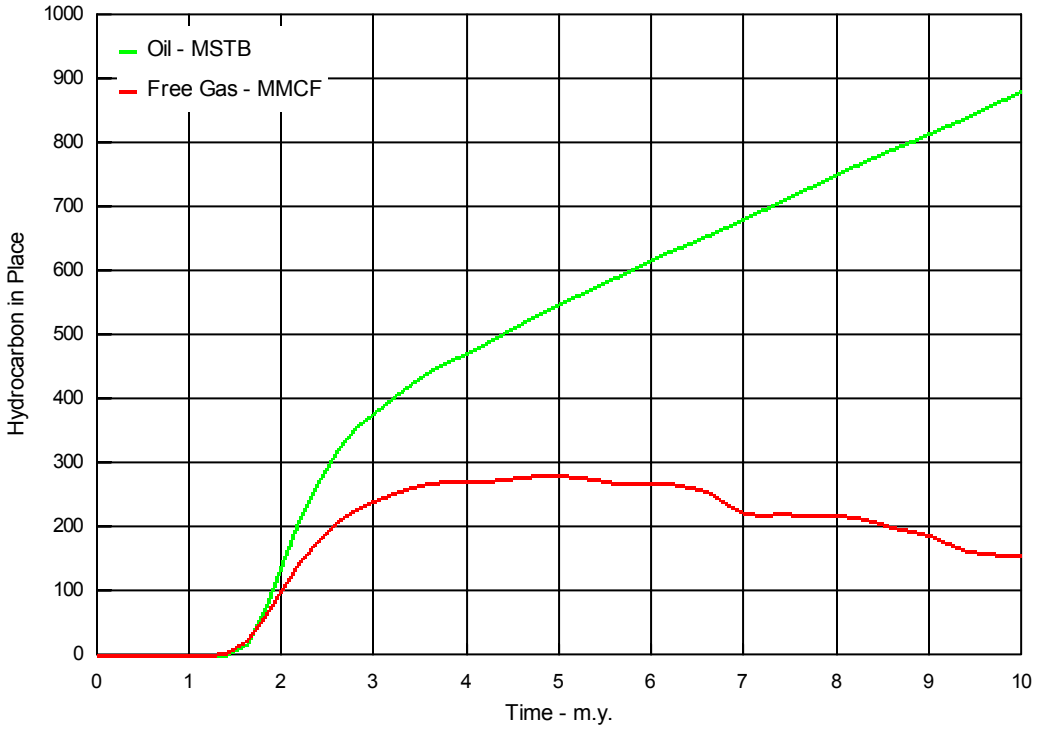

Figure 3-10: Hydrocarbon in Place versus Time in the Upper Sand (Run 5: Anticlinal Model).

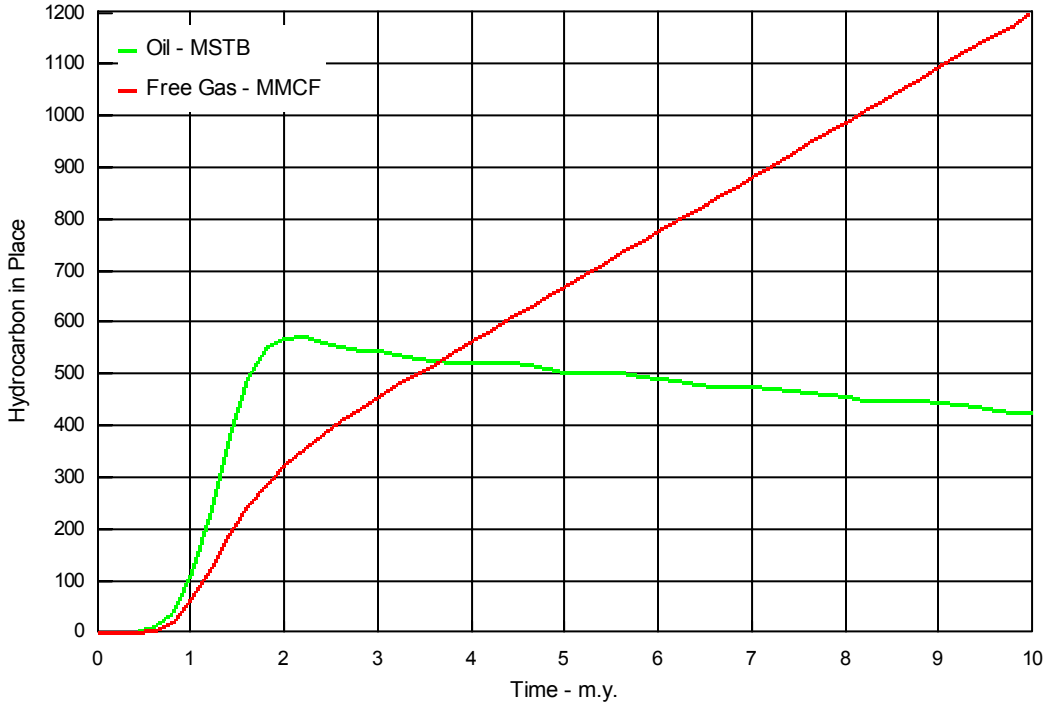

Figure 3-11: Hydrocarbon in Place versus Time in the Middle Sand (Run 5: Anticlinal Model).

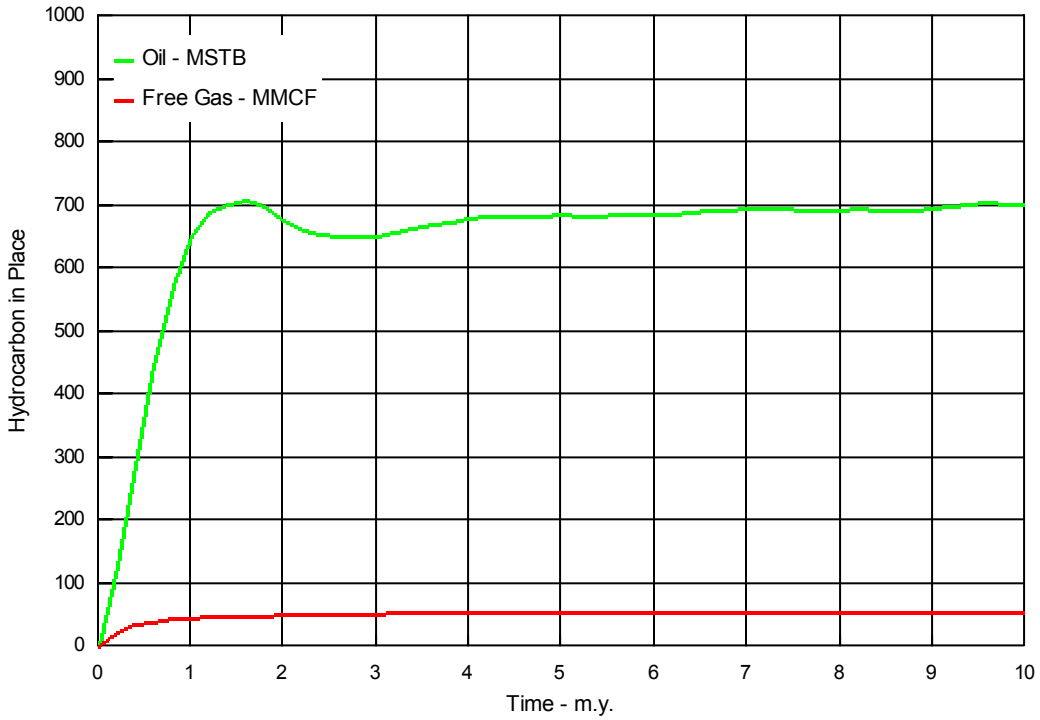

Figure 3-12: Hydrocarbon in Place versus Time in the Lower Sand (Run 5: Anticlinal Model).

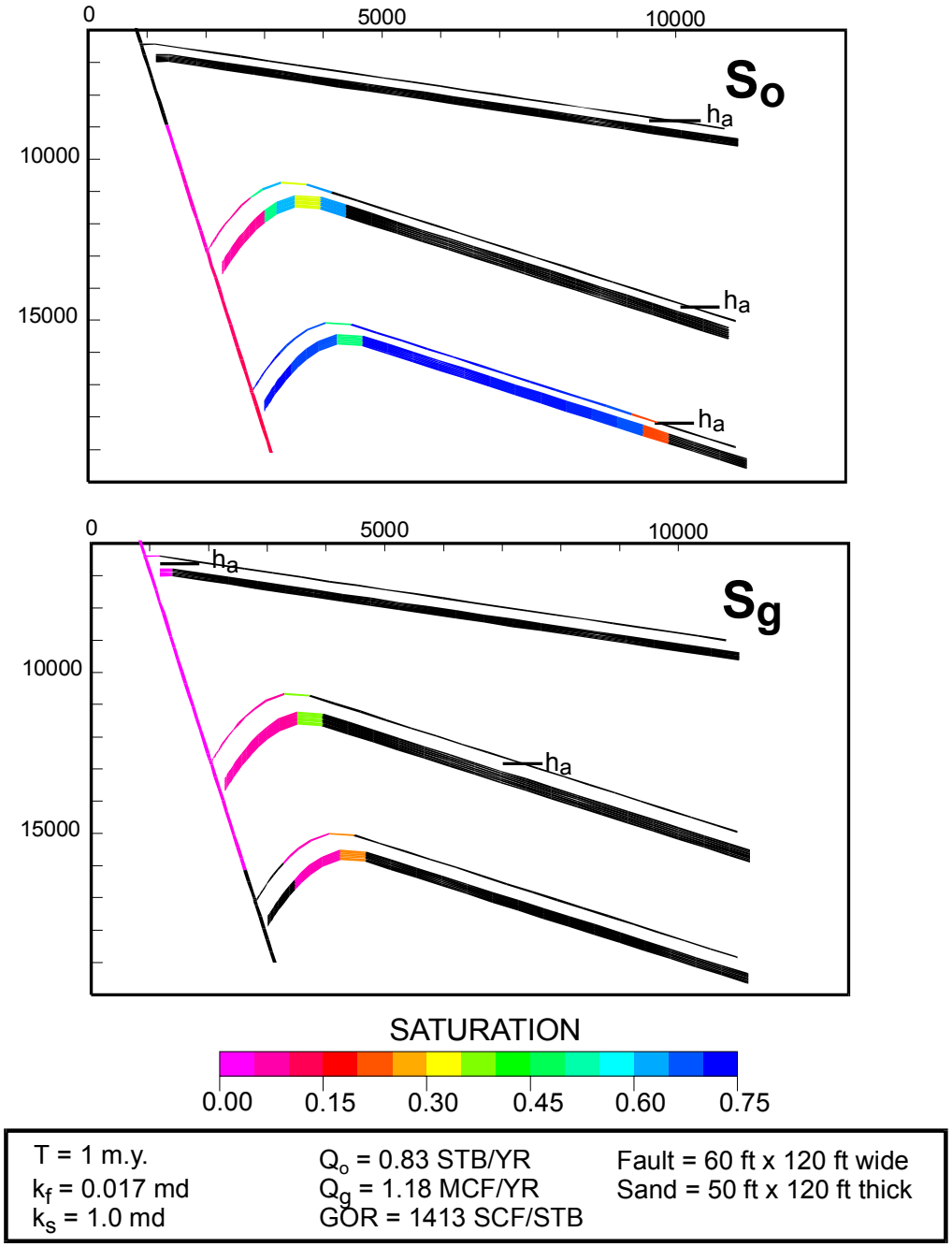

Figure 3-13: Hydrocarbon Saturation at 1 Million Years (Run 5: Anticlinal Model). Where T is the time of the simulation, k_f is the fault zone permeability, k_s is the reservoir sand permeability, Q_o is the oil charge rate, Q_g is the gas charge rate and GOR is the ratio of injected gas to oil.

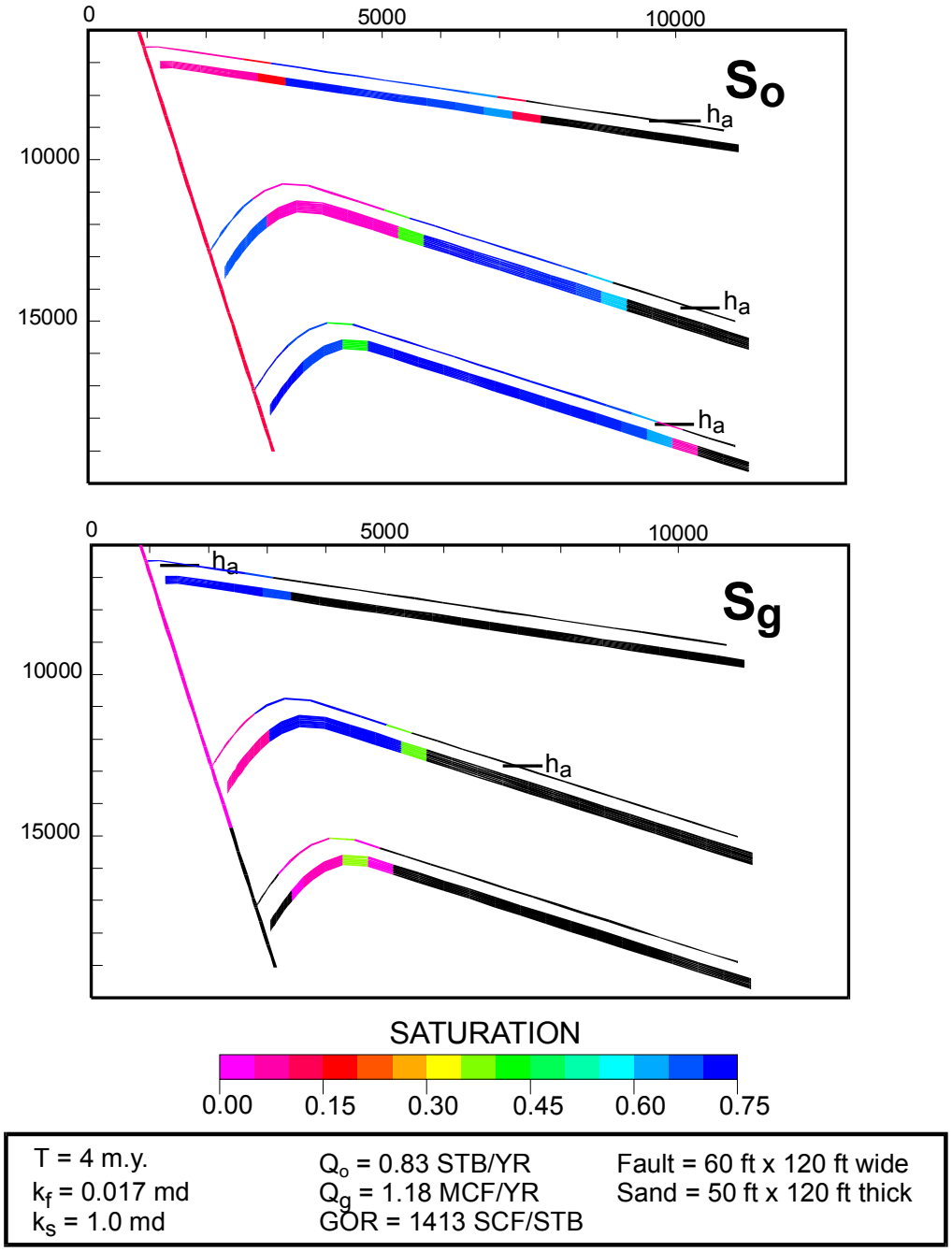

Figure 3-14: Hydrocarbon Saturation at 4 Million Years (Run 5: Anticlinal Model). Where T is the time of the simulation, k_f is the fault zone permeability, k_s is the reservoir sand permeability, Q_o is the oil charge rate, Q_g is the gas charge rate and GOR is the ratio of injected gas to oil.

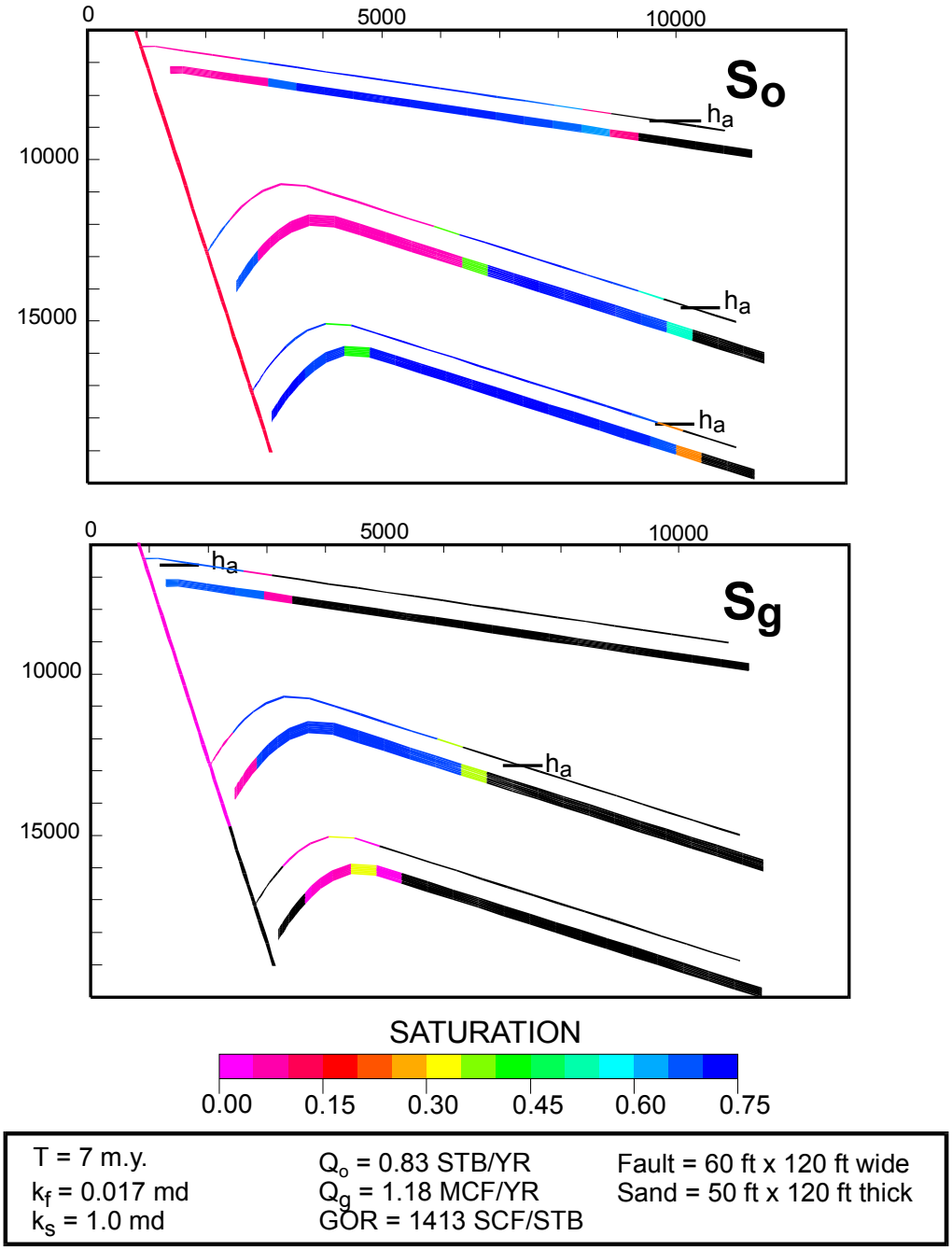

Figure 3-15: Hydrocarbon Saturation at 7 Million Years (Run 5: Anticlinal Model). Where T is the time of the simulation, k_f is the fault zone permeability, k_s is the reservoir sand permeability, Q_o is the oil charge rate, Q_g is the gas charge rate and GOR is the ratio of injected gas to oil.

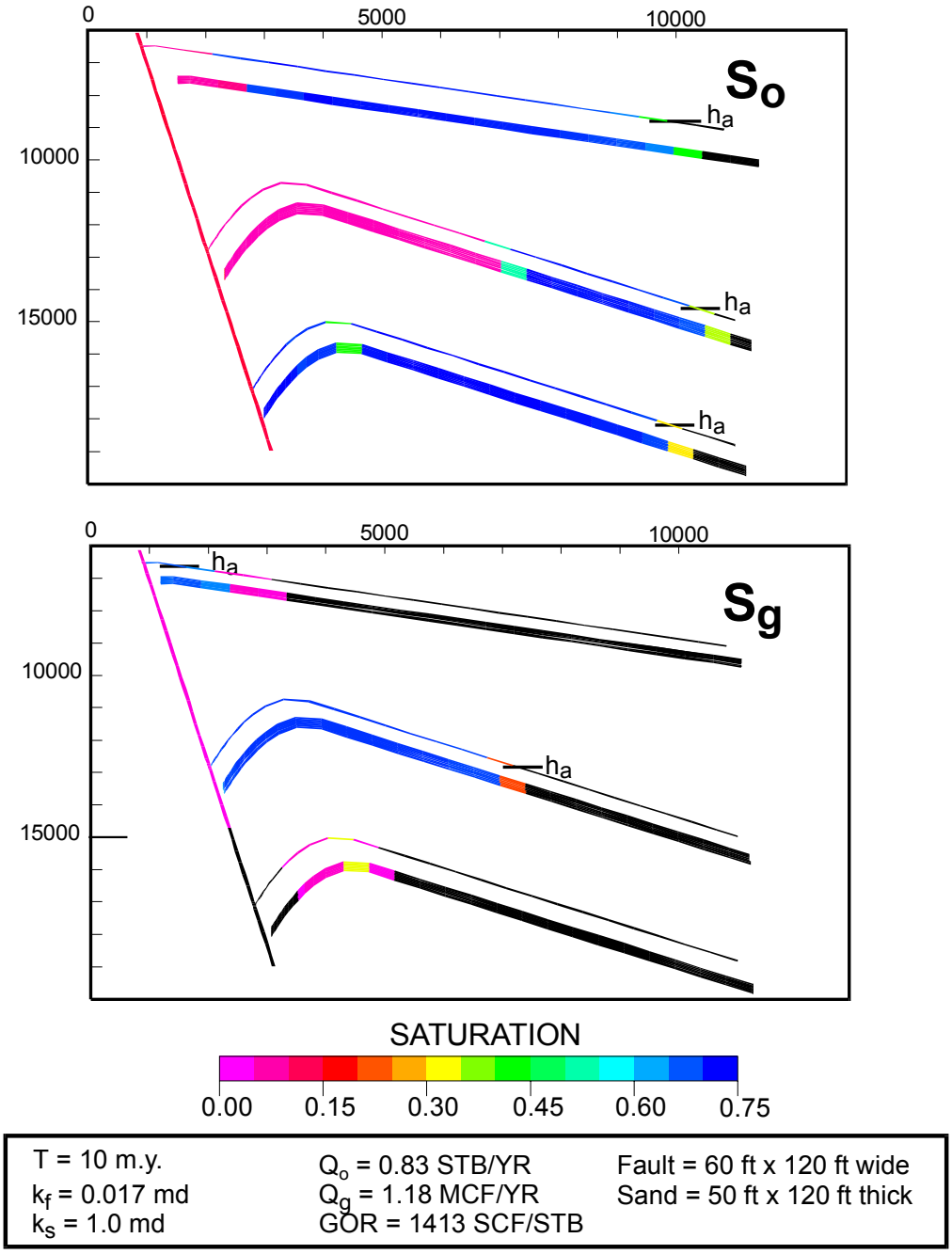

Figure 3-16: Hydrocarbon Saturation at 10 Million Years (Run 5: Anticlinal Model). Where T is the time of the simulation, k_f is the fault zone permeability, k_s is the reservoir sand permeability, Q_o is the oil charge rate, Q_g is the gas charge rate and GOR is the ratio of injected gas to oil.

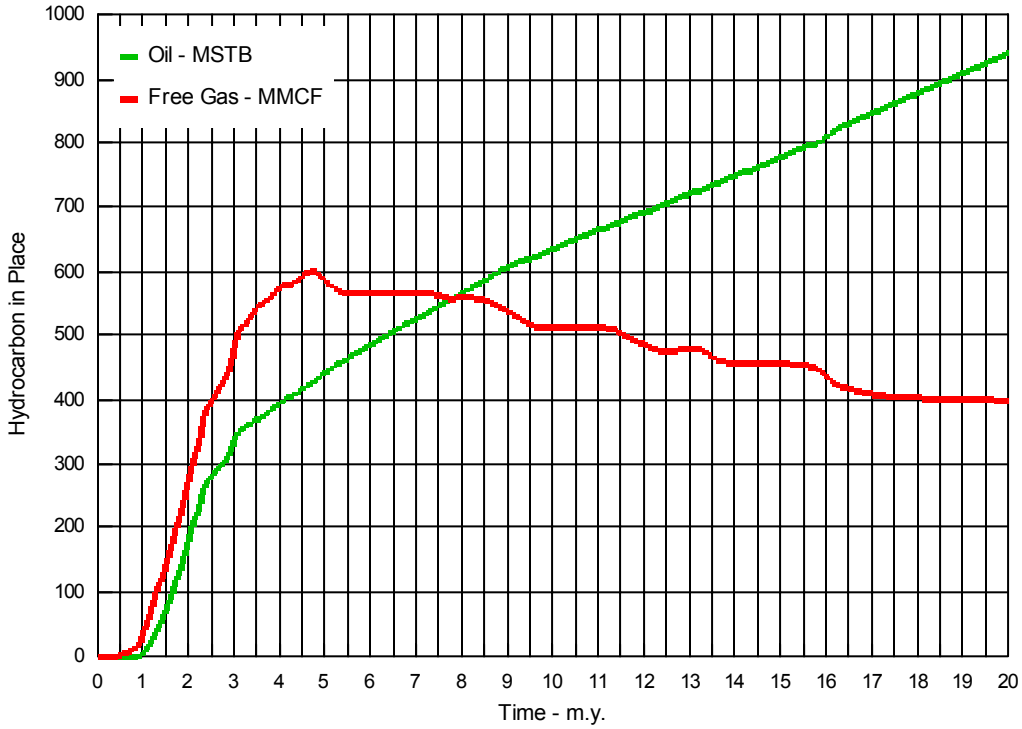

Figure 3-17: Hydrocarbons in Place versus Time in the Upper Sand (Run 6: Fault Seal Model).

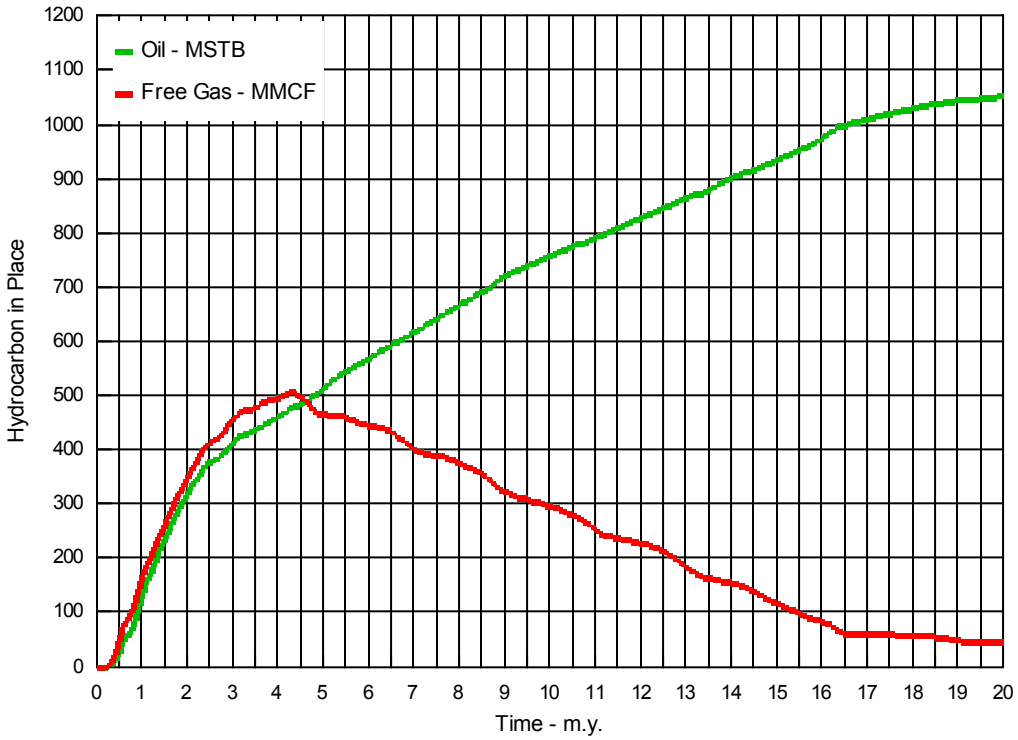

Figure 3-18: Hydrocarbons in Place versus Time in the Middle Sand (Run 6: Fault Seal Model).

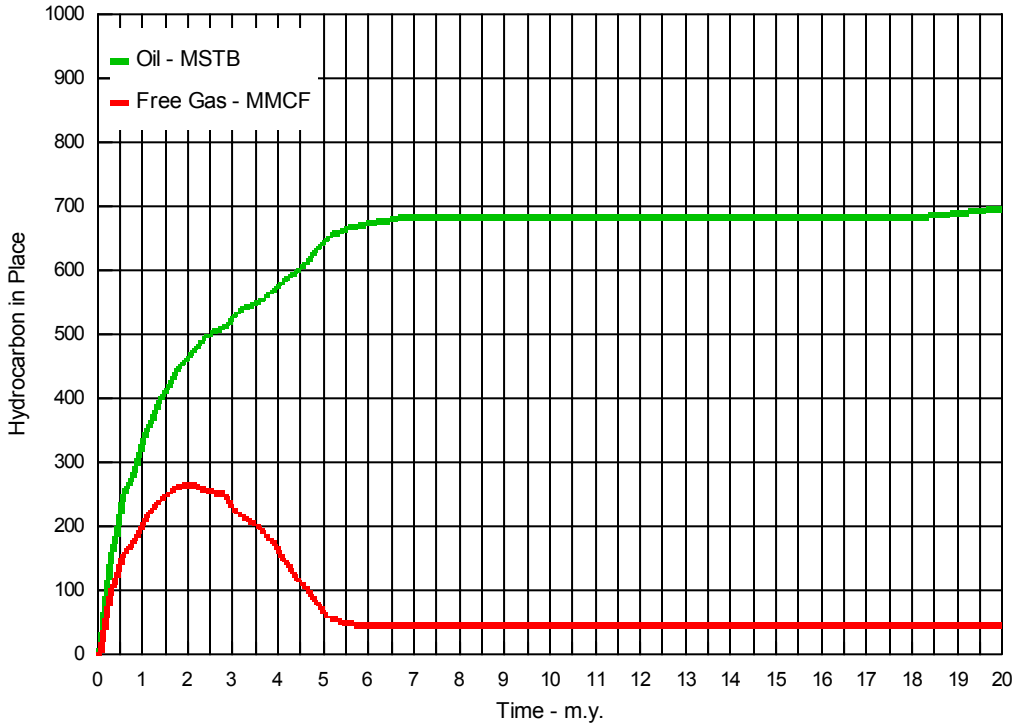

Figure 3-19: Hydrocarbons in Place versus Time in the Lower Sand (Run 6: Fault Seal Model).

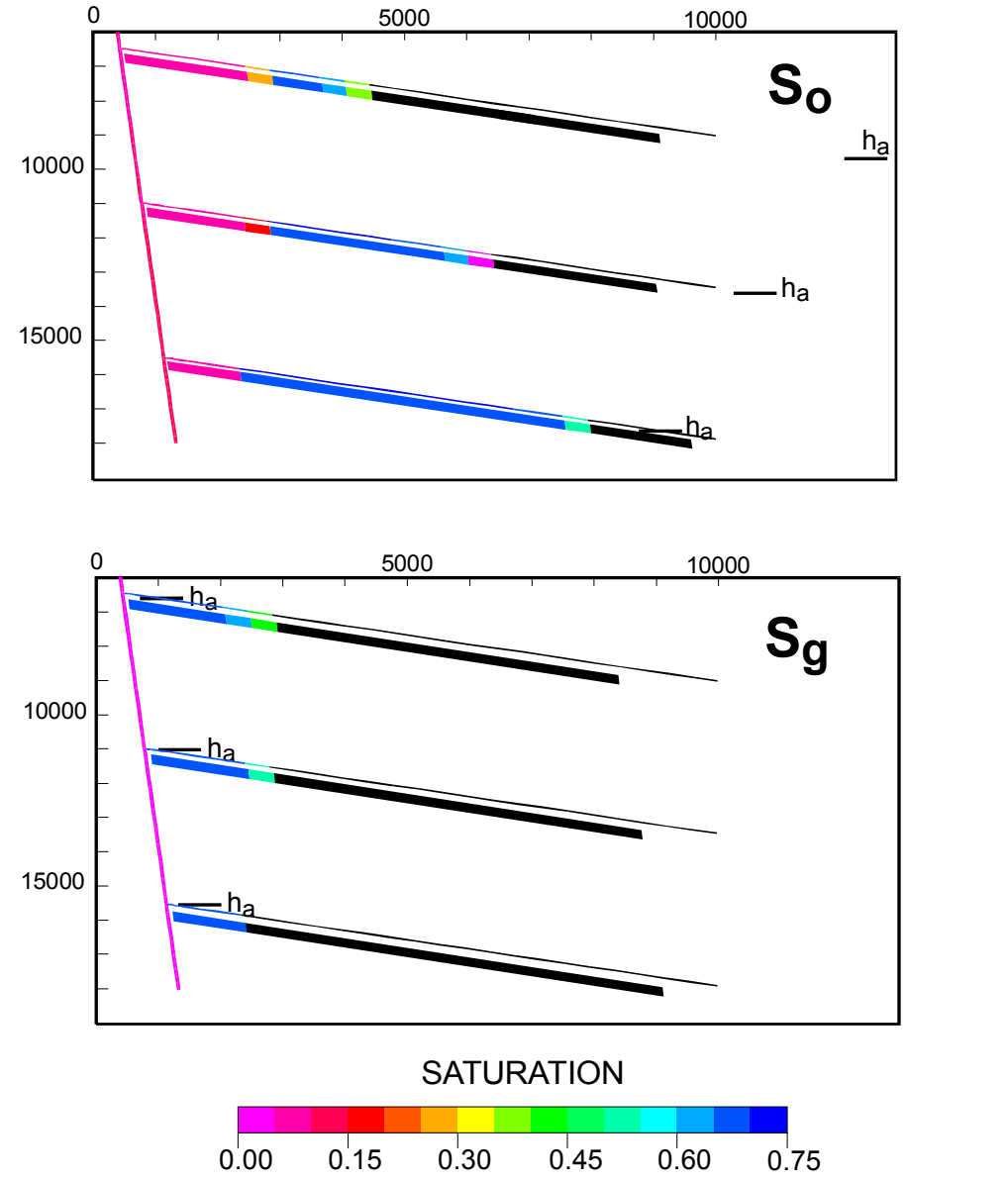

Figure 3-20: Hydrocarbon Saturation at 2 Million Years (Run 6: Fault Seal Model). Where T is the time of the simulation, k_f is the fault zone permeability, k_s is the reservoir sand permeability, Q_o is the oil charge rate, Q_g is the gas charge rate and GOR is the ratio of injected gas to oil.

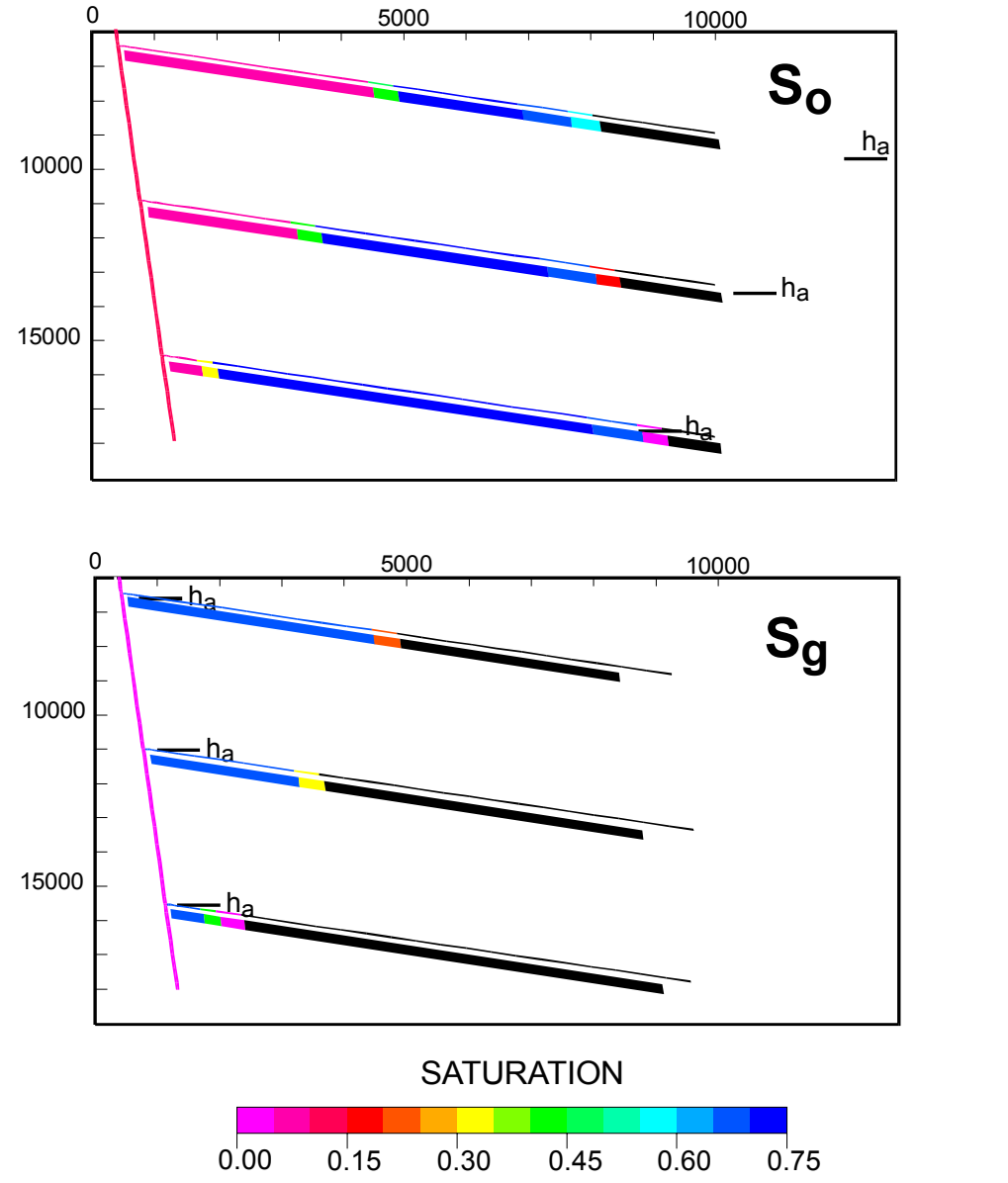

Figure 3-21: Hydrocarbon Saturation at 4 Million Years (Run 6: Fault Seal Model). Where T is the time of the simulation, k_f is the fault zone permeability, k_s is the reservoir sand permeability, Q_o is the oil charge rate, Q_g is the gas charge rate and GOR is the ratio of injected gas to oil.

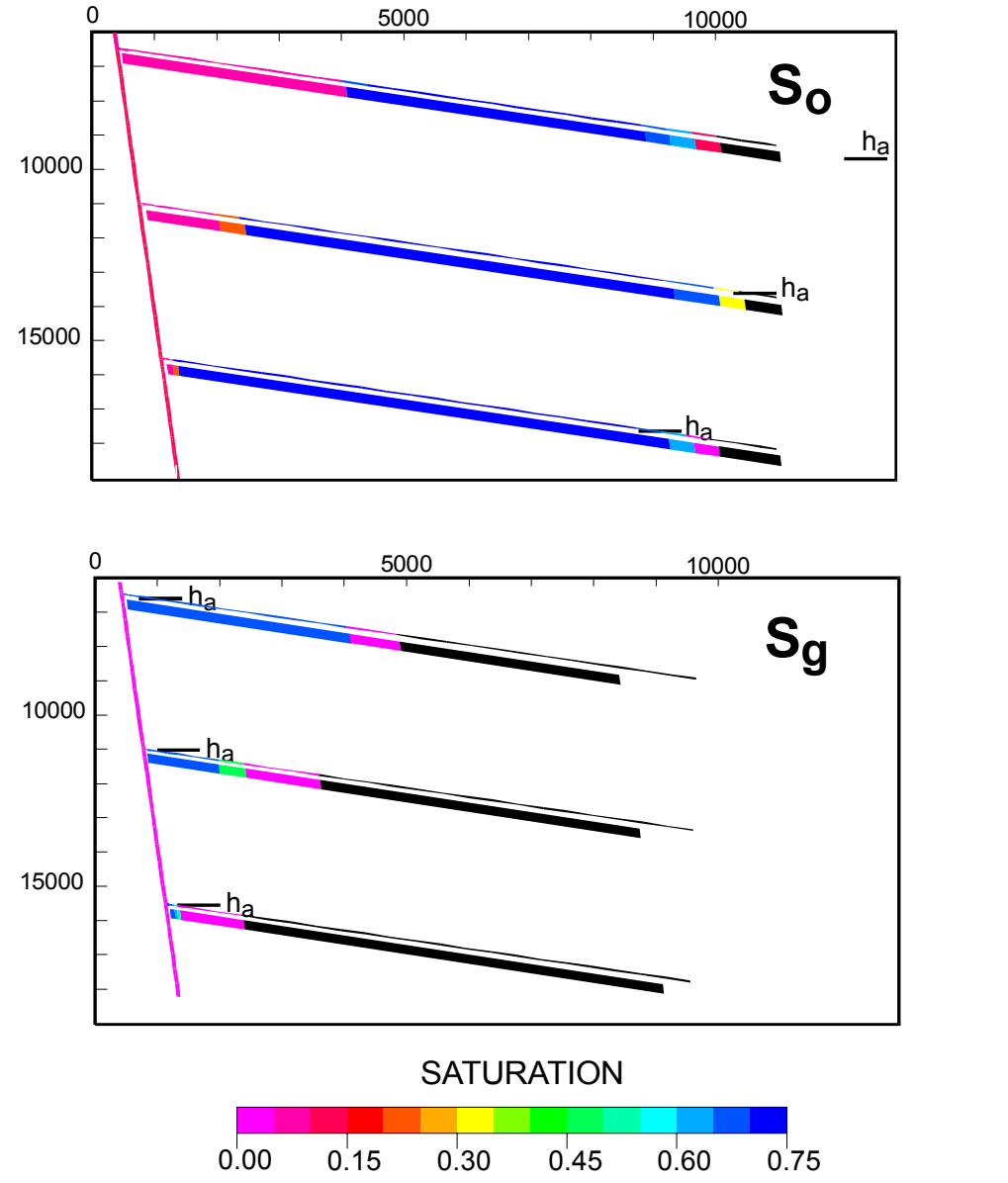

Figure 3-22: Hydrocarbon Saturation at 10 Million Years (Run 6: Fault Seal Model). Where T is the time of the simulation, k_f is the fault zone permeability, k_s is the reservoir sand permeability, Q_o is the oil charge rate, Q_g is the gas charge rate and GOR is the ratio of injected gas to oil.

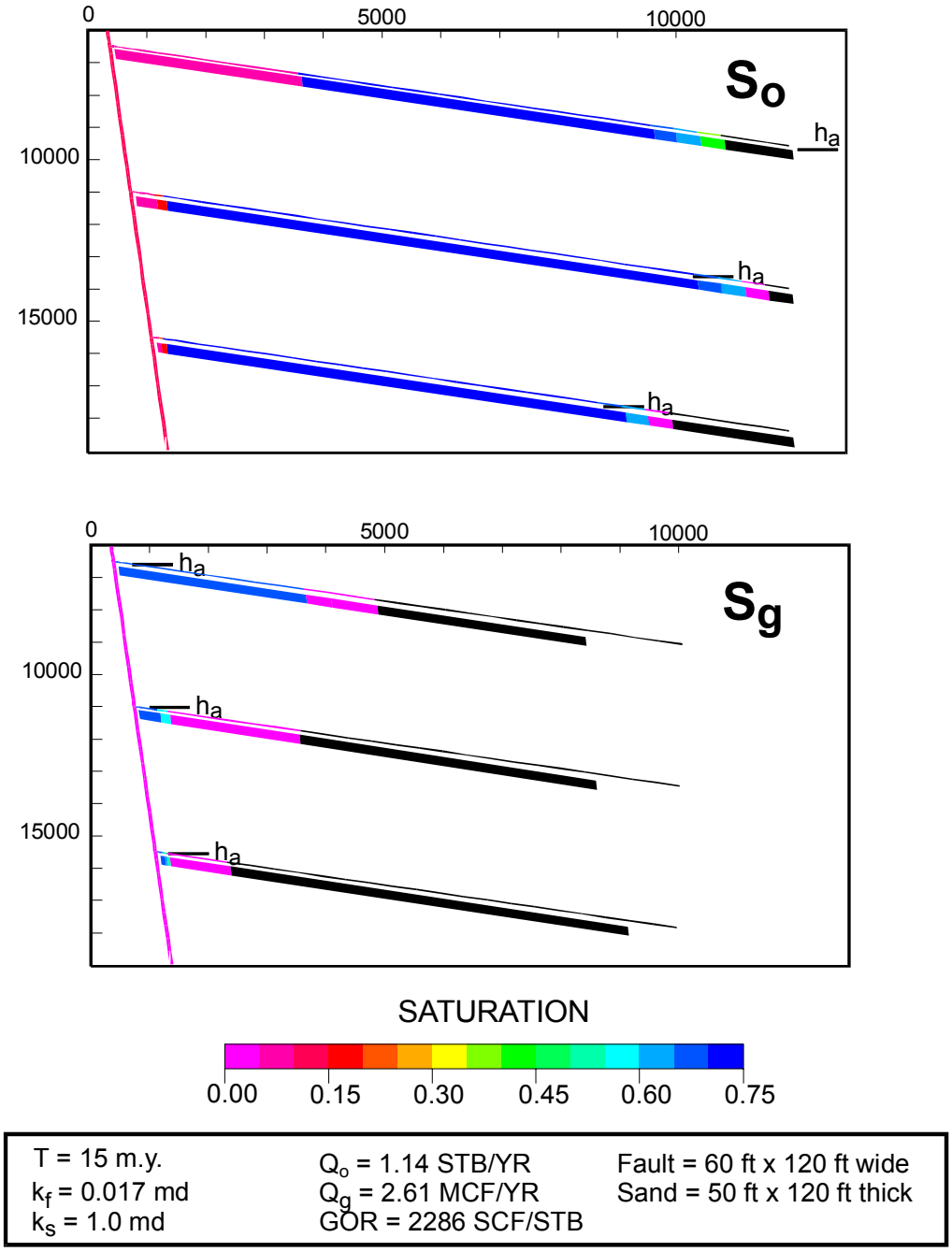

Figure 3-23: Hydrocarbon Saturation at 15 Million Years (Run 6: Fault Seal Model). Where T is the time of the simulation, k_f is the fault zone permeability, k_s is the reservoir sand permeability, Q_o is the oil charge rate, Q_g is the gas charge rate and GOR is the ratio of injected gas to oil.

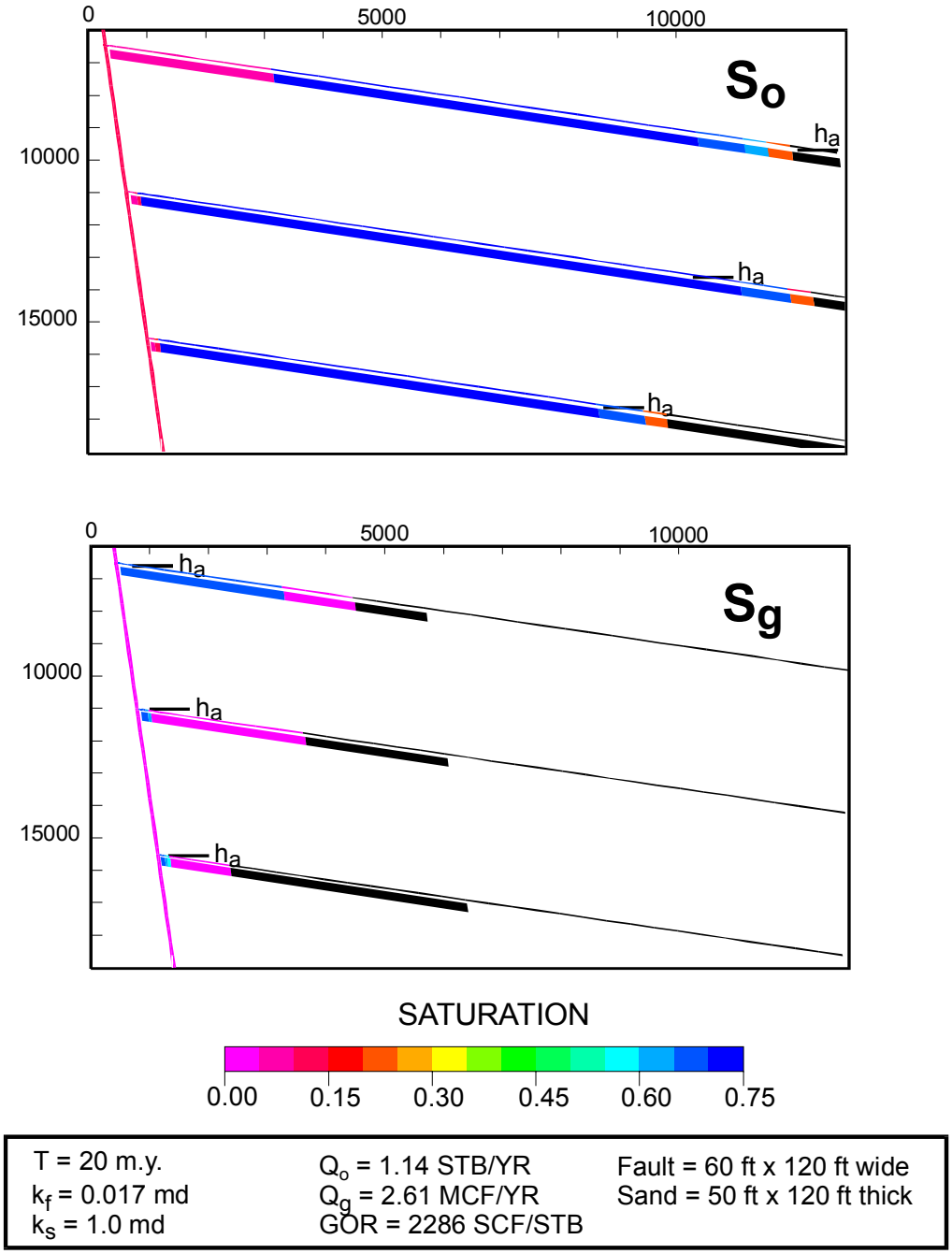

Figure 3-24: Hydrocarbon Saturation at 20 Million Years (Run 6: Fault Seal Model). Where T is the time of the simulation, k_f is the fault zone permeability, k_s is the reservoir sand permeability, Q_o is the oil charge rate, Q_g is the gas charge rate and GOR is the ratio of injected gas to oil.

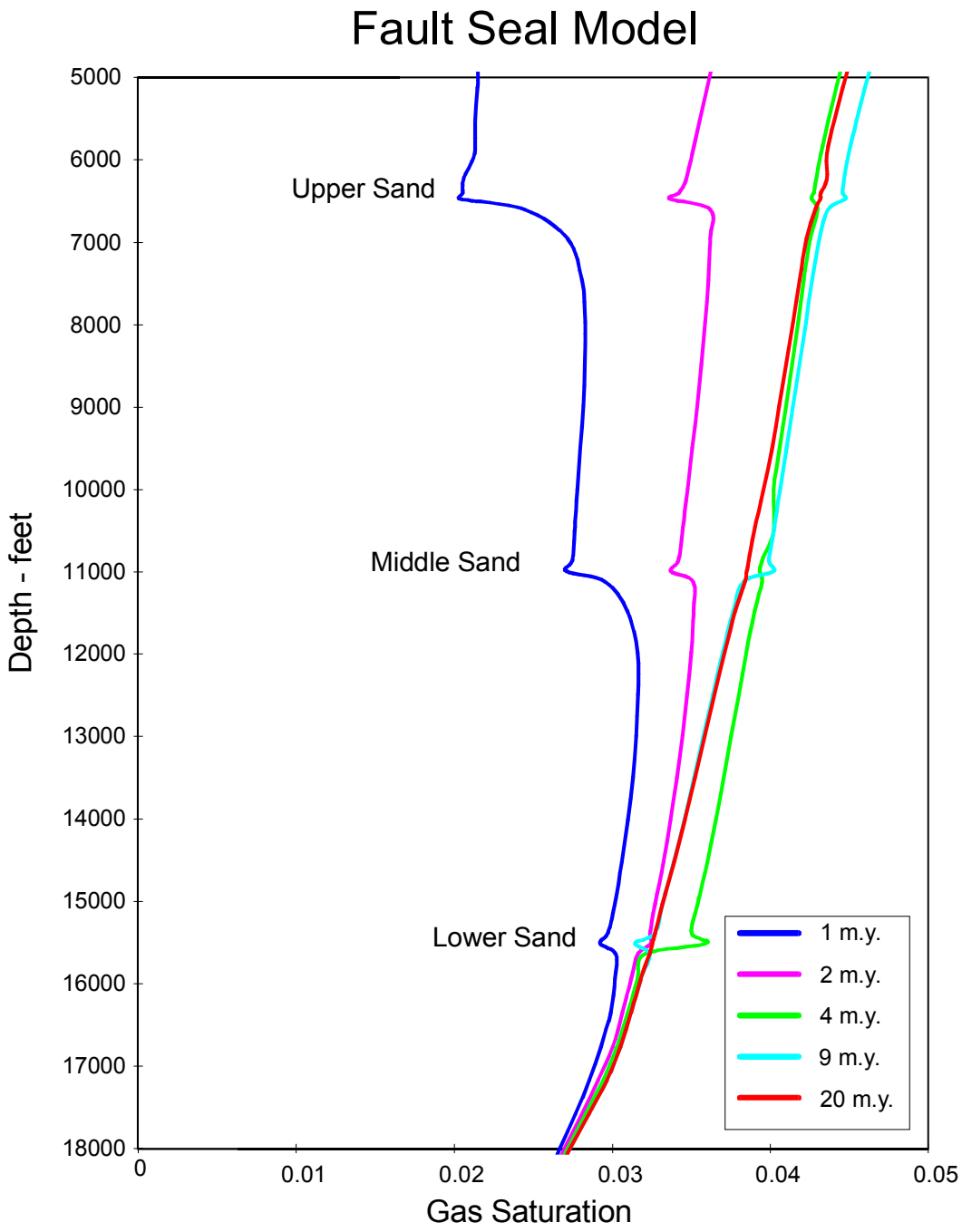

Figure 3-25: Fault zone gas saturation at various times (Run 6). As gas migrates up the fault, a shift in the saturation curve to the left, decrease in gas saturation, indicates that gas is charging the sand and a shift to the right, increase in gas saturation, indicates that the sand is expelling gas.

BIBLIOGRAPHY

Antonellini, M., and A. Aydin, 1994, Effect of Faulting on Fluid Flow in Porous Sandstones: Petrophysical Properties: AAPG Bulletin, v. 78, p. 35-377.

Amyx, J. W., D. M. Bass Jr., and R. L. Whiting, 1960, Petroleum Reservoir Engineering: New York, McGraw-Hill. 610 p.

Aziz, K., and A. Settari, 1979, Petroleum Reservoir Simulation: London, Applied Science Publishers LTD. 476p.

Beggs, H. D. and J. R. Robinson,1975, Estimating the Viscosity of Crude Oil Systems: Journal of Petroleum Technology, p. 1140-1141.

Bennett, M., 1996, Simulation of Secondary Migration in Faults: Dynamic Controls on Hydrocarbon Column Height: M.S. thesis in Mineral Engineering, The Pennsylvania State University.

Blunt, M., D. Zhou, and D. Fenwick, 1995, Three-Phase Flow and Gravity Drainage in Porous Media: Transport in Porous Media, v. 20, p. 77-103.

Bouvier, J. D., C. H. Kaars-Sijpesteijn, D. F. Kluesner, C.C. Onyejekwe, and R. C. van der Pal, 1989, Three-Dimensional Seismic Interpretation and Fault Sealing Investigations, Nun River Field, Nigeria: AAPG Bulletin, v. 73, p. 1397-1414.

Caine, J., J. Evans, and C. Forster, 1996, Fault Zone Architecture and Permeability Structure: Geology, v. 24, p. 1025-1028.

Hippler, S. J., 1993, Deformation Microstructures and Diagenesis in Sandstone Adjacent to an Extensional Fault: Implications for the Flow and Entrapment of Hydrocarbons: AAPG Bulletin, v. 77, p. 625-637.

Jorden, J. R., and F. L. Campbell, 1984, Well Logging I - Rock Properties, Borehole Environment, Mud, and Temperature Logging: New York, Society of Petroleum Engineers of AIME, 167p.

Lee, A. L., M. H. Gonzalez, and B. E. Eakin, 1966, The Viscosity of Natural Gases, Journal of Petroleum Technology, pp. 997-1000.

McCain, W. D., 1973, The Properties of Petroleum Fluids, Tulsa, PennWell Publishing Company. 305p.

Pittman, E. D., 1981, Effect of Fault-Related Granulation on Porosity and Permeability of Quartz Sandstones, Simpson Group (Ordivician), Oklahoma: AAPG Bulletin, v. 65, p. 2381-2387.

Schowalter, T.T., 1979, Mechanics of Secondary Hydrocarbon Migration and Entrapment: AAPG Bulletin, v. 63, p. 723-760.

Vasquez, M. and H. D. Beggs, 1980, Correlations for Fluid Physical Property Prediction: Journal of Petroleum Technology, p. 968-970.

Appendix A

GEO-PRESSURE ANALYTICAL EXAMPLE

General Equation for 1-dimensional incompressible flow in oilfield units

$$\frac{Q_o}{A} = \frac{0.001127 k k r_o}{\mu_o}\left(\frac{dP_w}{dz} - \rho_o\right)\cos\theta \qquad \text{(A-1)}$$

Oil Column Height

$$h_o = \frac{144\,P_{cow}}{\left(\rho_w - \rho_o\right)} \qquad \text{(A-2)}$$

where:

A - Cross-sectional area of fault, ft^2

h_o - Oil column height, ft

k - Intrinsic permeability, md

kr_o - Relative permeability to oil, dimensionless

P_{cow} - Capillary pressure, psi

P_w - Water phase pressure, psi

Q_o - Oil flow rate, STB/D

S_w - Water phase saturation, dimensionless

z - Depth below datum, ft

μ_o - Oil viscosity, cp

ρ_o - Oil density, lb/ft^3

ρ_w - Water density, lb/ft^3

θ - Angle of fault from vertical

Geo-pressure Model Input Parameters

Q_o - 2.124x10^{-3} STB/D
A - 7200 ft^2
k_{fault} - 0.017 md

ρ_o - 53 lb/ft^3
ρ_w - 67 lb/ft^3
μ_o - 0.352 cp

Example using EPR Fault Zone Capillary Pressure Data

Parameter	Case 1	Case 2
dP/dz	0.8	0.465 (hydrostatic)
kr_o	0.0013	0.0056
S_w	0.965	0.942
P_{cow}	32	65
h_o	329	669

Example using Thomeer's Capillary Pressure Relationship

Parameter	Case 1	Case 2
dP/dz	0.8	0.465 (hydrostatic)
kr_o	0.0013	0.0056
S_w	0.965	0.942
P_{cow}	16.1	16.3
h_o	166	168

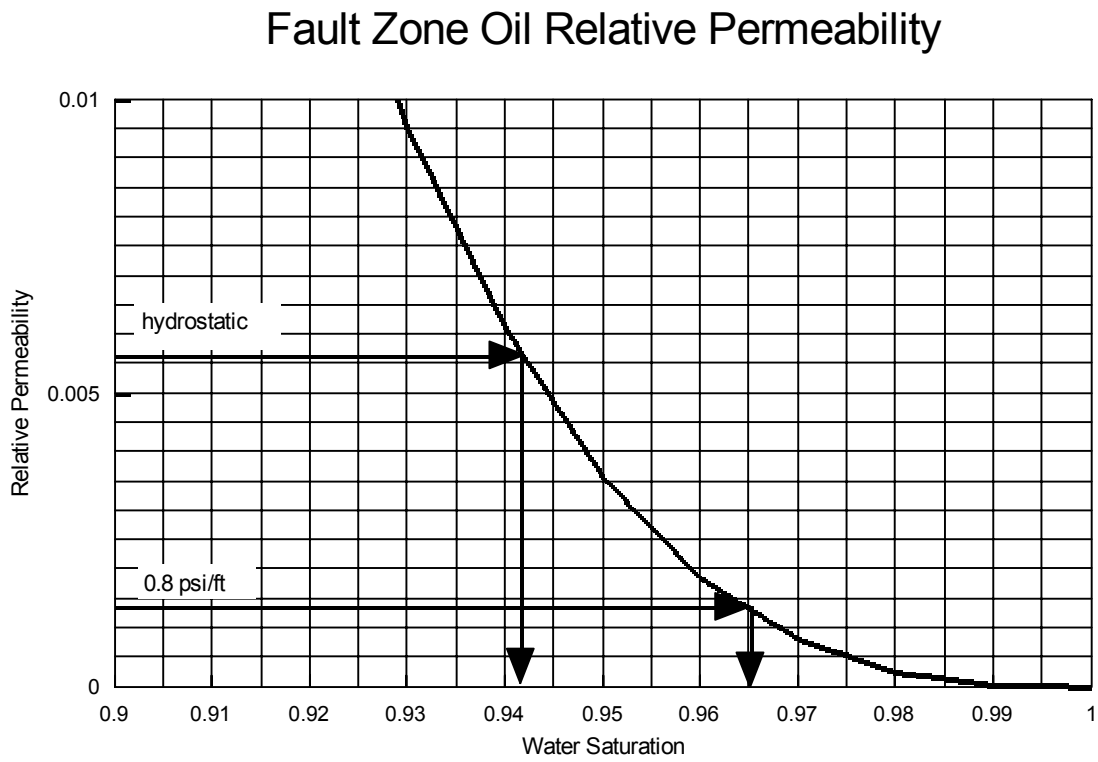

Figure A-1: Expanded oil relative permeability in the fault zone.

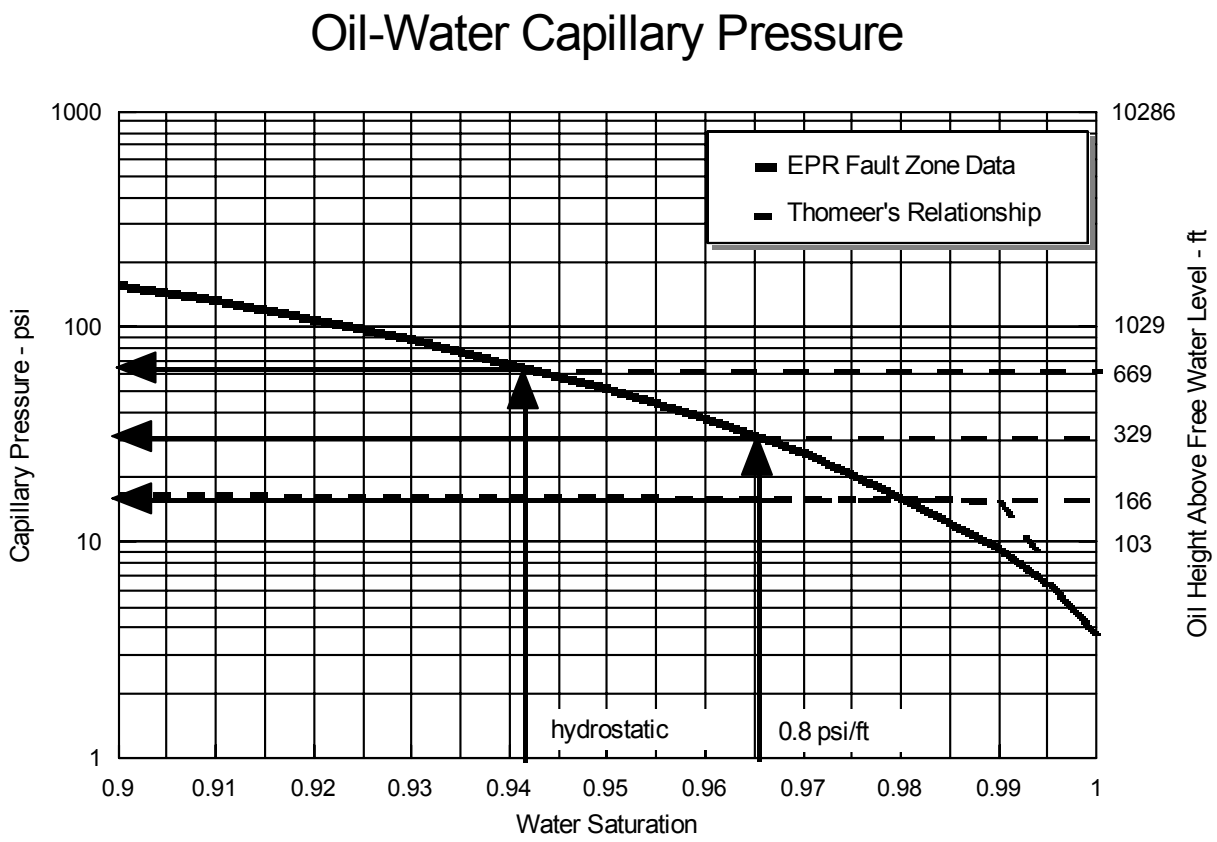

Figure A-2: Expanded capillary pressure in the fault zone.

Appendix B

3-PHASE PVT DATA

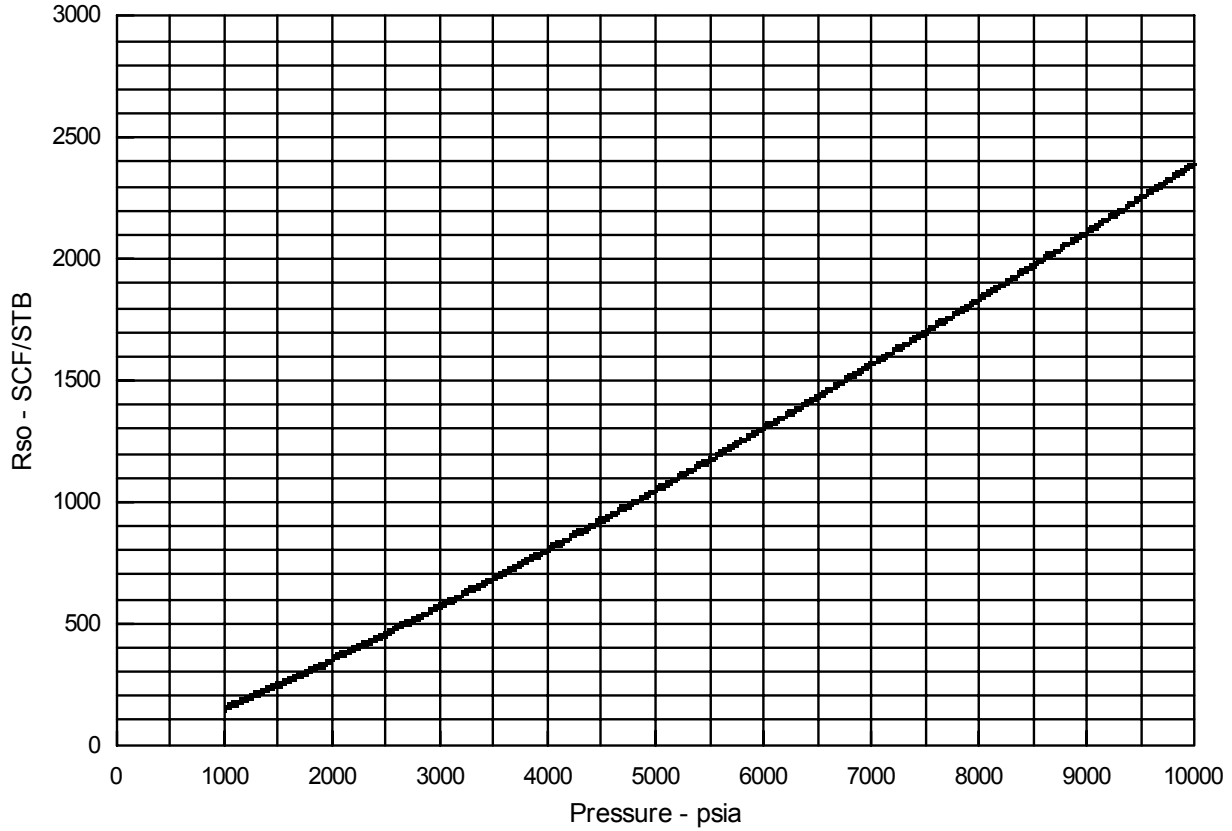

Figure B-1: Solution Gas-Oil Ratio (Rs_o) versus Pressure for a 35^o API oil and 0.8 specific gravity gas at 300^o F (Vazquez and Beggs, 1980)

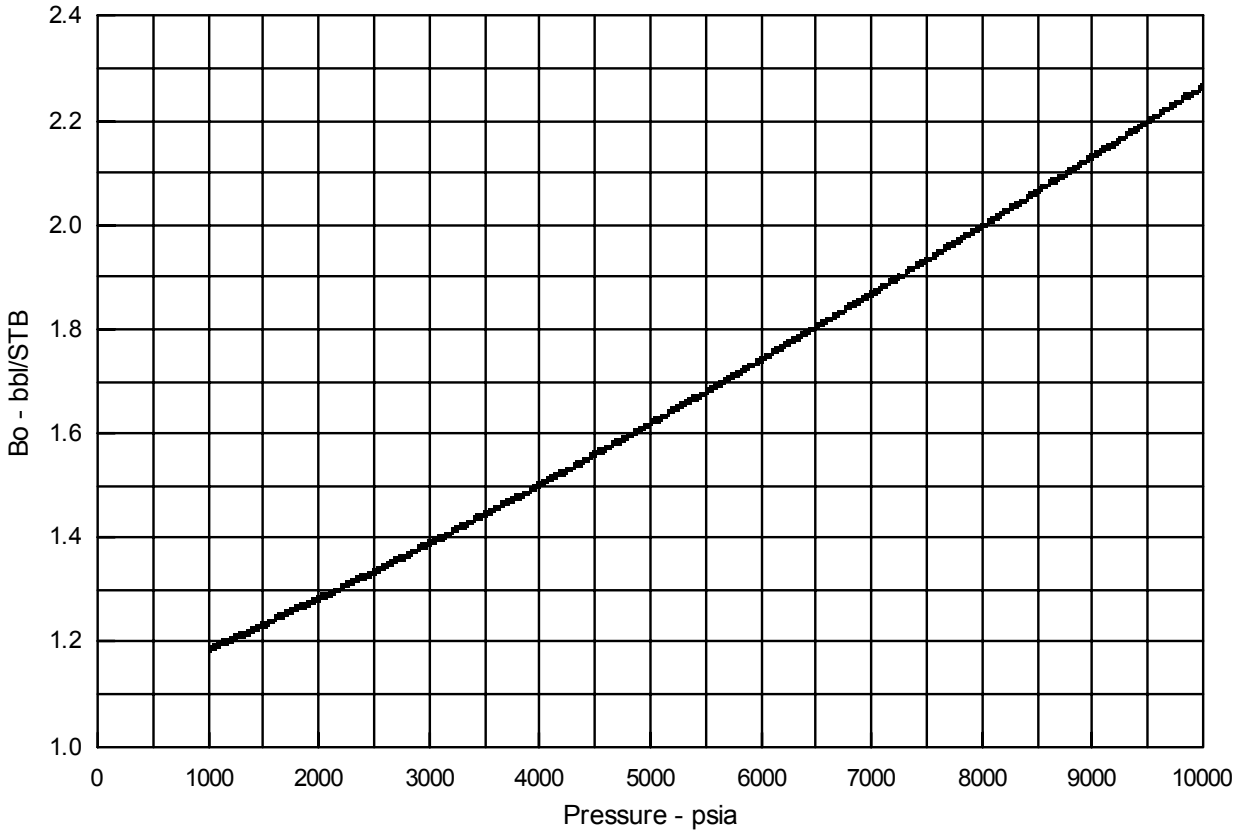

Figure B-2: Oil Formation Volume Factor (B_o) versus Pressure for a 35^o API oil and 0.8 specific gravity gas at 300^o F (Vazquez and Beggs, 1980)

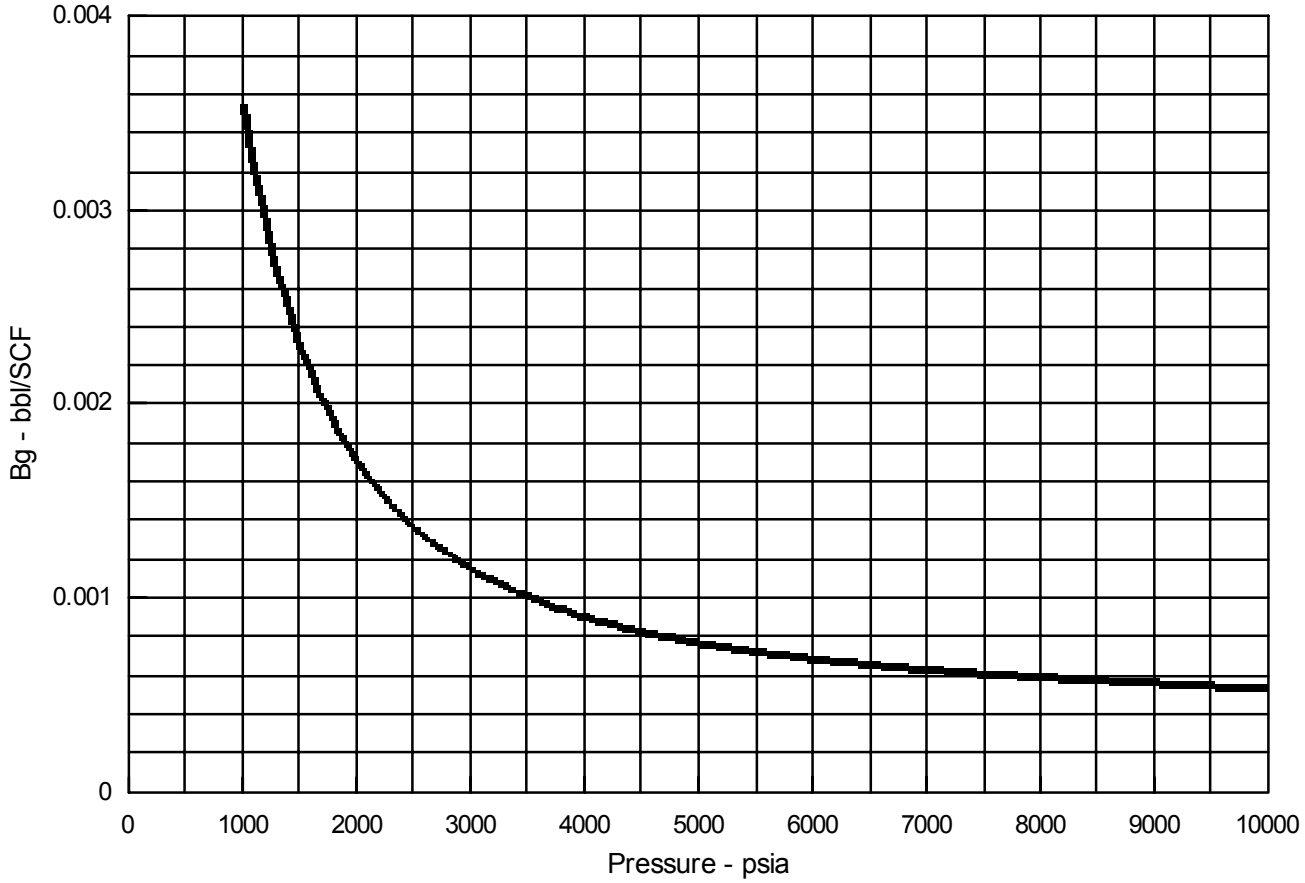

Figure B-3: Gas Formation Volume Factor (B_g) versus Pressure for a 0.8 specific gravity gas at 300^o F (McCain, 1973)

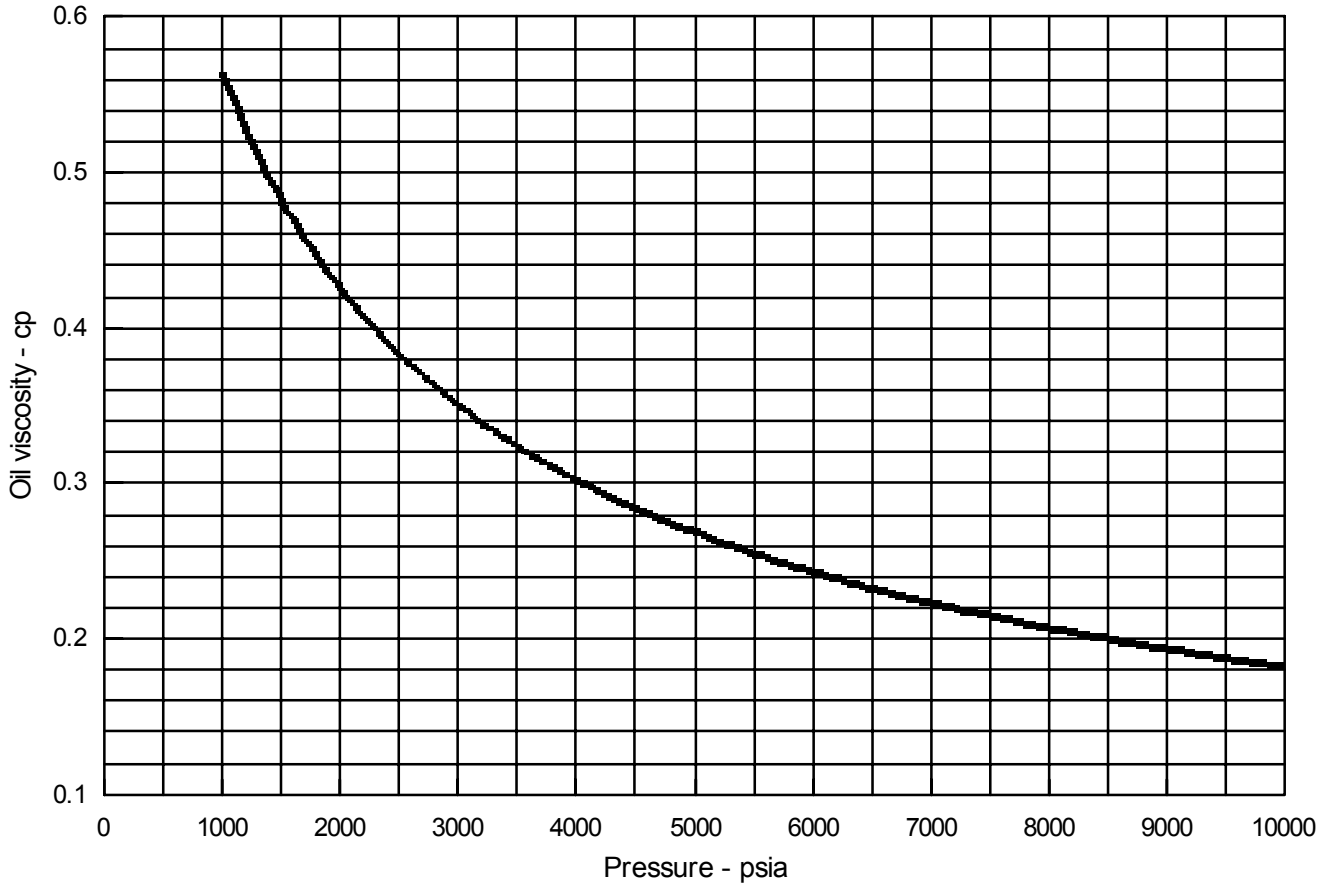

Figure B-4: Oil Viscosity (μ_o) versus Pressure for a 35^o API oil and 0.8 specific gravity gas at 300^o F (Vazquez and Beggs, 1980)

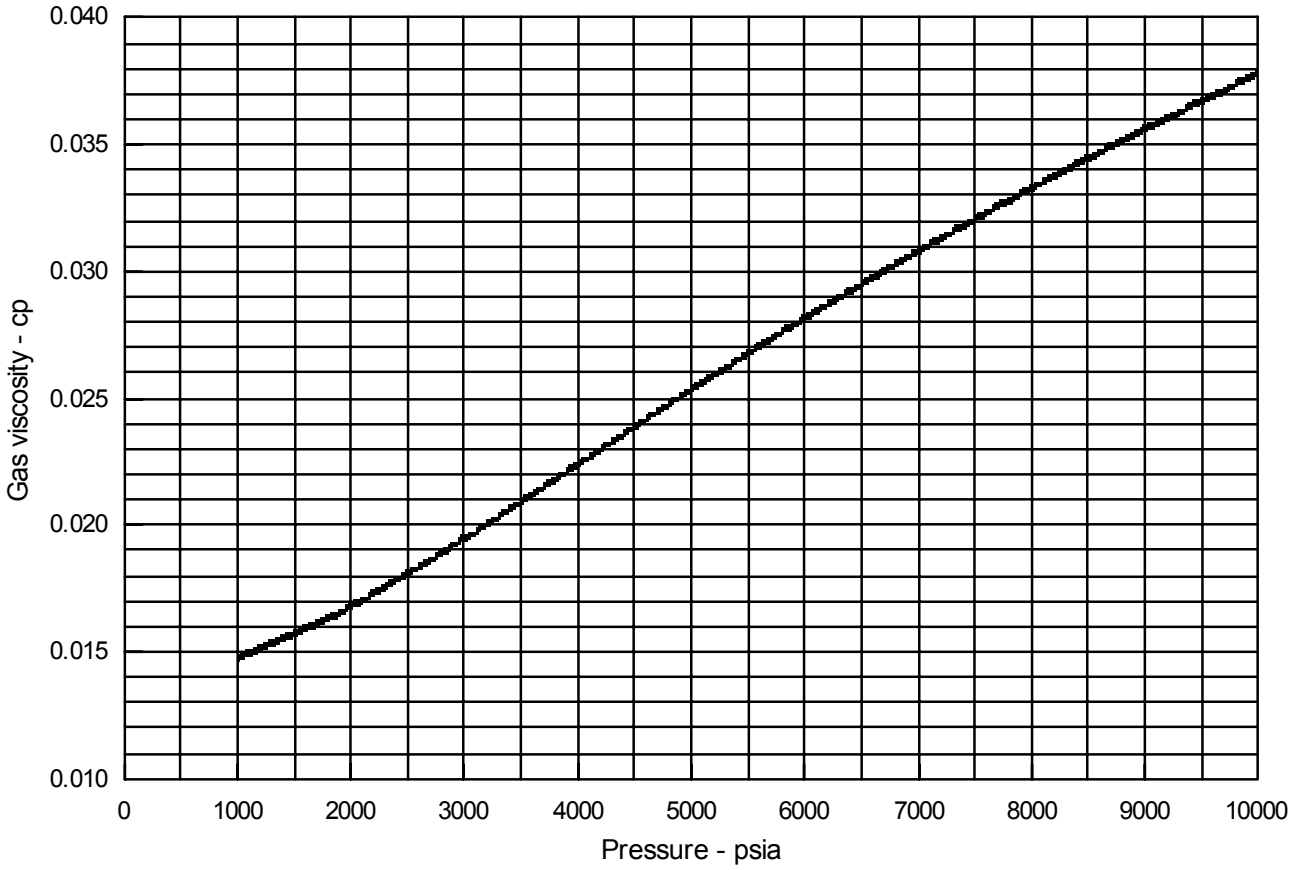

Figure B-5: Gas Viscosity (μ_g) versus Pressure for a 0.8 specific gravity gas at 300^o F (Lee, et al., 1966)

Appendix C

EXAMPLE OF 3-PHASE ANALYTICAL SOLUTION FOR HYDROCARBON COLUMN HEIGHT

The 3-phase equation for oil flux through a hydrostatic water column can be written as follows for field units:(C-1)

$$\frac{Q_o}{A} = \frac{0.001127 \cdot k \cdot kr_o \cdot \frac{(\rho_w - \rho_o)}{144}}{B_o \cdot \mu_o} \tag{C-1}$$

And the equation for gas flux as:

$$\frac{Q_g}{A} = 0.001127 \cdot \left(\frac{k \cdot kr_g \cdot \frac{(\rho_w - \rho_g)}{144}}{B_g \cdot \mu_g} + \frac{Rso \cdot k \cdot kr_o \cdot \frac{(\rho_w - \rho_o)}{144}}{B_o \cdot \mu_o} \right) \tag{C-2}$$

Total column height is written as:

$$h_{oil+gas} = \frac{144 \cdot P_{cow}}{\rho_w - \rho_o} \tag{C-3}$$

and gas column height as:

$$h_{gas} = \frac{144 \cdot P_{cog}}{\rho_o - \rho_g} \tag{C-4}$$

where:

A - Cross-sectional area of fault, ft^2

B_g - Gas formation volume factor, res.bbl./SCF

B_o - Oil formation volume factor, res.bbl./STB

h - Height, ft

k - Intrinsic permeability, md

kr - Relative permeability, dimensionless

P_c - Capillary pressure, psi

Q_g - Gas flow rate, SCF/D

Q_o - Oil flow rate, STB/D

Rs_o - Solution gas-oil ratio, SCF/STB

μ - Viscosity, cp

ρ - Density, lb/ft^3

Subscripts: g - gas

o - oil

w - water

Given the following data:

Depth	12826	ft
Q_o	6.26E-03	STB/D
Q_g	32.055	SCF/D
A	7200	sq. ft.
k	0.017	md
P_w (hydrostatic)	5964.09	psia
ρ_w	67	lb/ft3

Step 1. Using P_w as a first estimate for P_o and P_g, determine values for all pressure dependent parameters from PVT data (*Figure C-1 - Figure C-7*).

Iteration	P_o	P_g	B_o	B_g	Rs_o	μ_o	μ_g	ρ_o	ρ_g
0	5964.09	5964.09	1.74	0.00069	1299	0.244	0.028	38.59	15.68

Step 2. Rearrange equation (C-1) to solve for kr_o

$$kr_o = \frac{144 \cdot Q_o \cdot B_o \cdot \mu_o}{0.001127 \cdot k \cdot A \cdot (\rho_w - \rho_o)} \qquad \text{(C5)}$$

Step 3. Use values from step 1 in equation (C-5) and calculate kr_o to be 0.0977

Step 4. Rearrange equation (C-2) to solve for kr_g

$$kr_g = \frac{B_g \cdot \mu_g}{\rho_w - \rho_g} \cdot \left(\frac{144 \cdot Q_g}{0.001127 \cdot k \cdot A} - \frac{Rs_o \cdot kr_o \cdot (\rho_w - \rho_o)}{B_o \cdot \mu_o} \right) \qquad \text{(C-6)}$$

Step 5. Use values from step 1 in equation (C-6) and calculate kr_g to be 0.0094

Step 6. Enter 2-phase oil-gas relative permeability chart (*Figure C-8*) and determine the gas saturation where a kr_g of 0.0094 intercepts the gas relative permeability curve. (S_g = 0.07)

Step 7. Enter 3-phase oil relative permeability chart (*Figure C-9*) and determine the water saturation where a gas saturation of 0.07 intercepts the kr_o equals 0.0977 relative permeability curve. (S_w = 0.82)

Step 8. Enter the oil-water capillary pressure chart (*Figure C-10*) and determine the P_{cow} where an S_w of 0.82 intercepts the fault zone capillary pressure curve. (P_{cow} = 630 psi)

Step 9. Enter the oil-gas capillary pressure chart (*Figure C-11*) and determine the P_{cog} where an S_g of 0.07 intercepts the fault zone capillary pressure curve. (P_{cog} = 22 psi)

Step 10. Add P_{cow} to P_w to determine a new P_o . (P_o = 6594 psia)

Step 11. Add P_{cog} to P_o to determine a new P_g . (P_g = 6616 psia)

Step 12. Compare new hydrocarbon phase pressures to previous iteration. If difference is greater than 1 psi repeat steps 1 through 11 using new pressures.

The following table shows the results of the remaining iterations for this example.

Iteration	P_o	P_g	B_o	B_g	Rs_o	μ_o	μ_g	ρ_o	ρ_g
1	5964.1	5964.1	1.74	0.00069	1299	0.244	0.028	38.59	15.68
2	6594.1	6616.3	1.83	0.000655	1464	0.231	0.0298	37.9	16.56
3	6518.1	6539.8	1.81	0.000663	1443	0.232	0.0294	37.98	16.37
4	6518.1	6539.8							

Iteration	ρ_o	ρ_g	kr_o	kr_g	S_g	S_w	P_{cow}	P_{cog}
1	38.59	15.68	0.0977	0.0094	0.07	0.82	630	22.2
2	37.9	16.56	0.0949	0.0093	0.069	0.83	554	21.7
3	37.98	16.37	0.0946	0.0093	0.069	0.83	554	21.7
4								

Step 13. Use the values for density and capillary pressure from the last iteration in equation (C-3) to calculate hydrocarbon column height (above free water level) to be 2,751 ft.

Step 14. Use the values for density and capillary pressure from the last iteration in equation (C-4) to calculate gas column height (above free oil level) to be 62 ft.

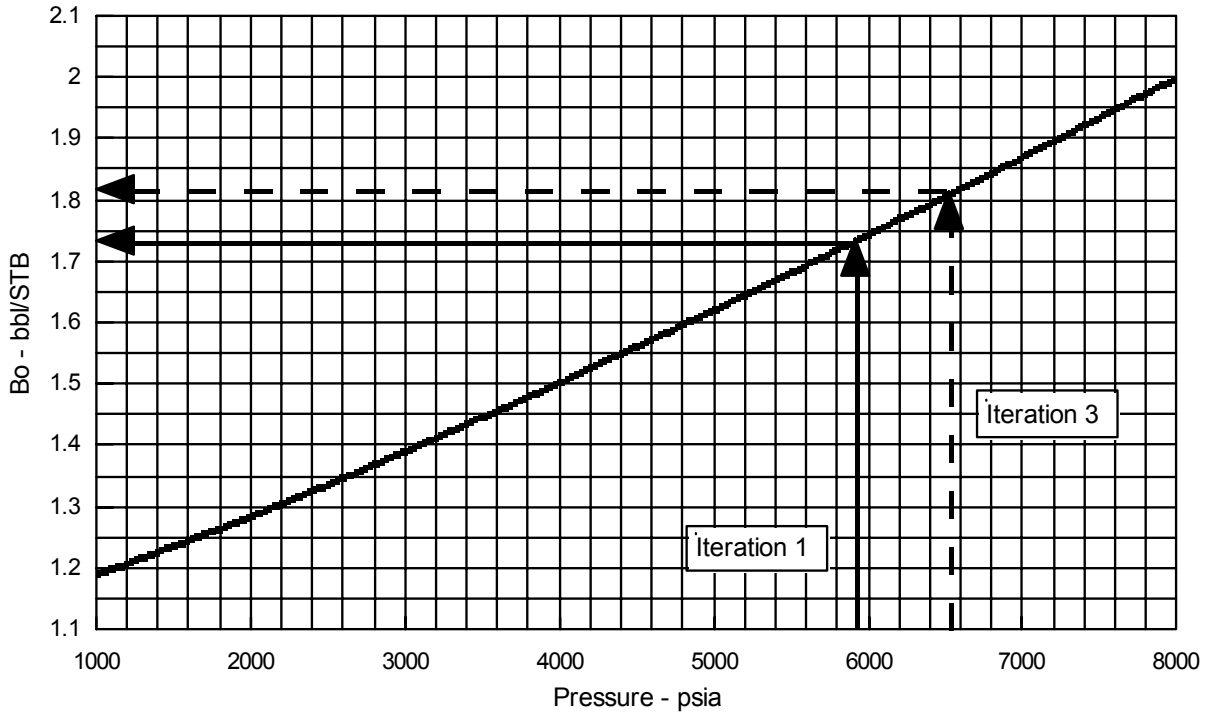

Figure C-1: Oil Formation Volume Factor versus Pressure

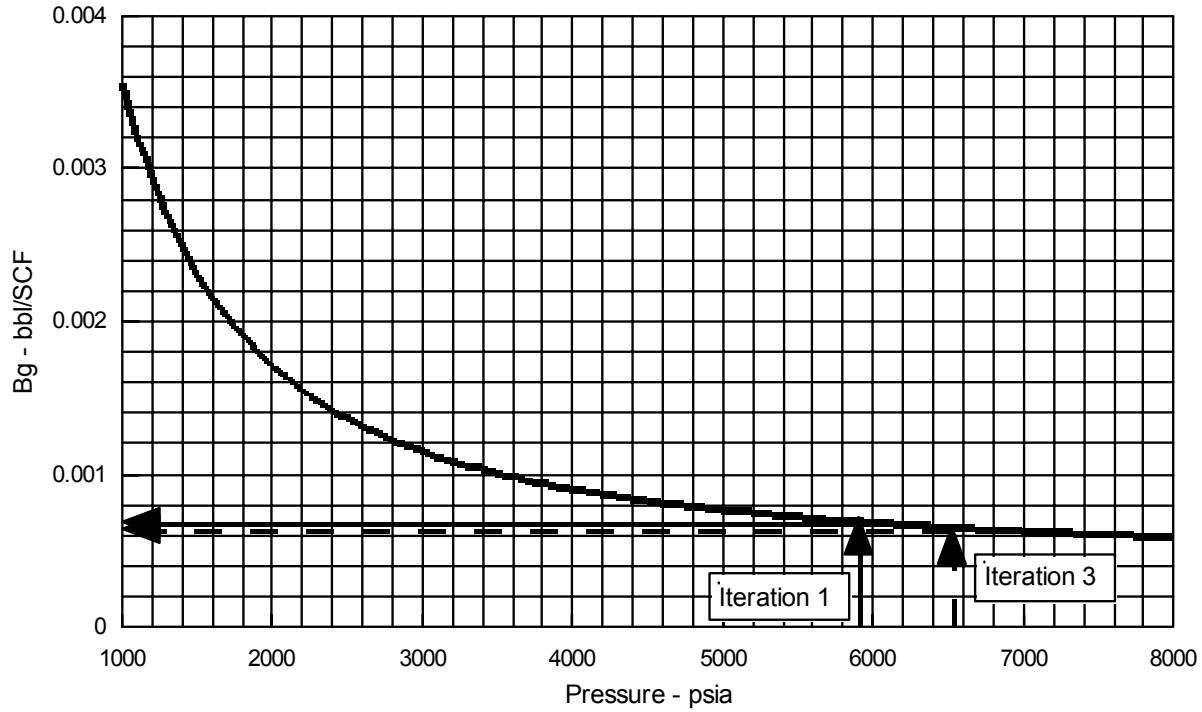

Figure C-2: Gas Formation Volume Factor versus Pressure

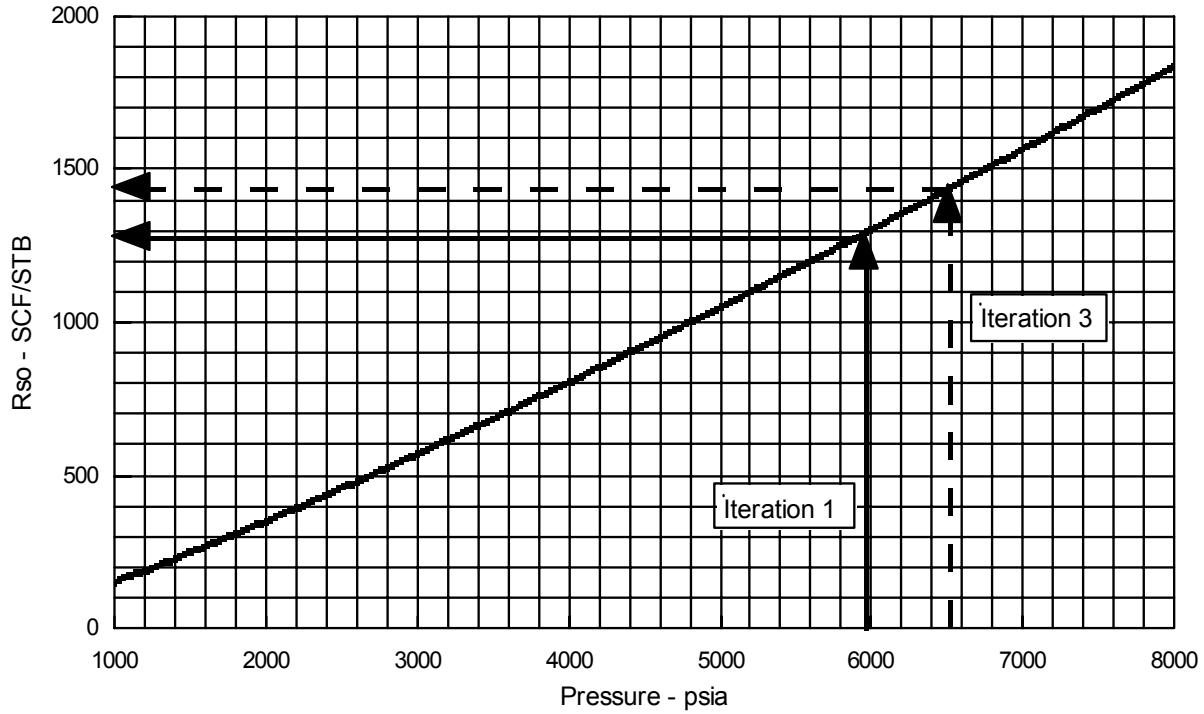

Figure C-3: Solution Gas-Oil Ratio versus Pressure

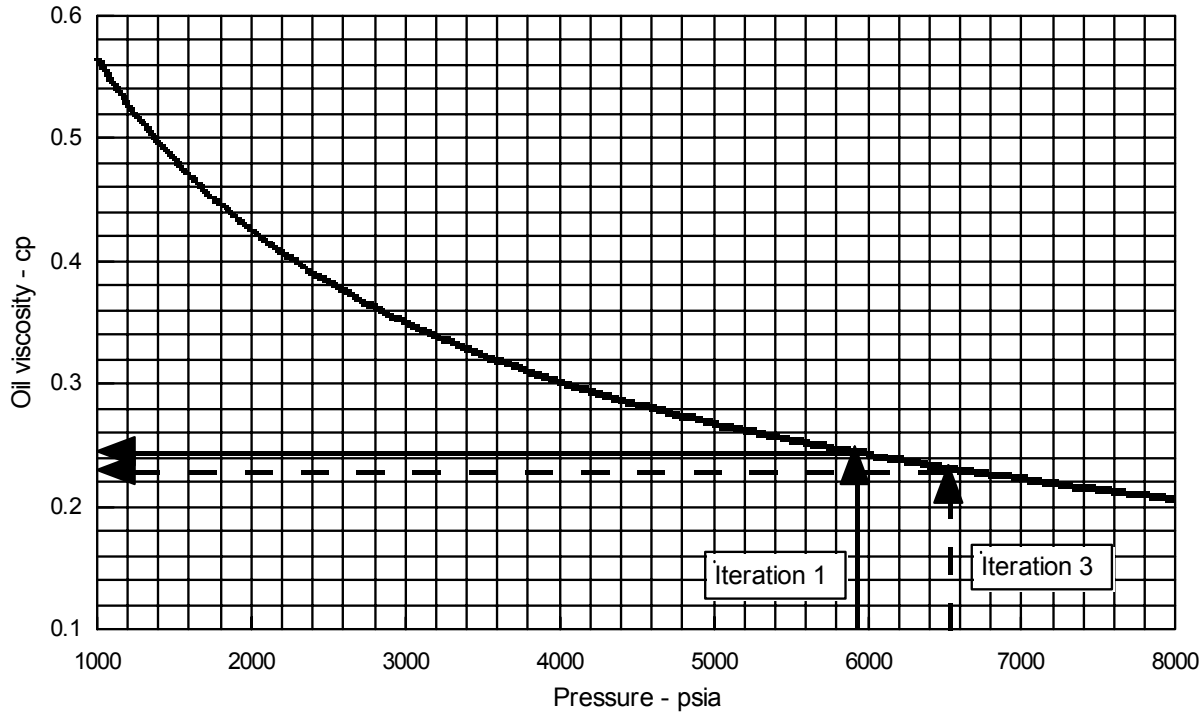

Figure C-4: Oil Viscosity versus Pressure

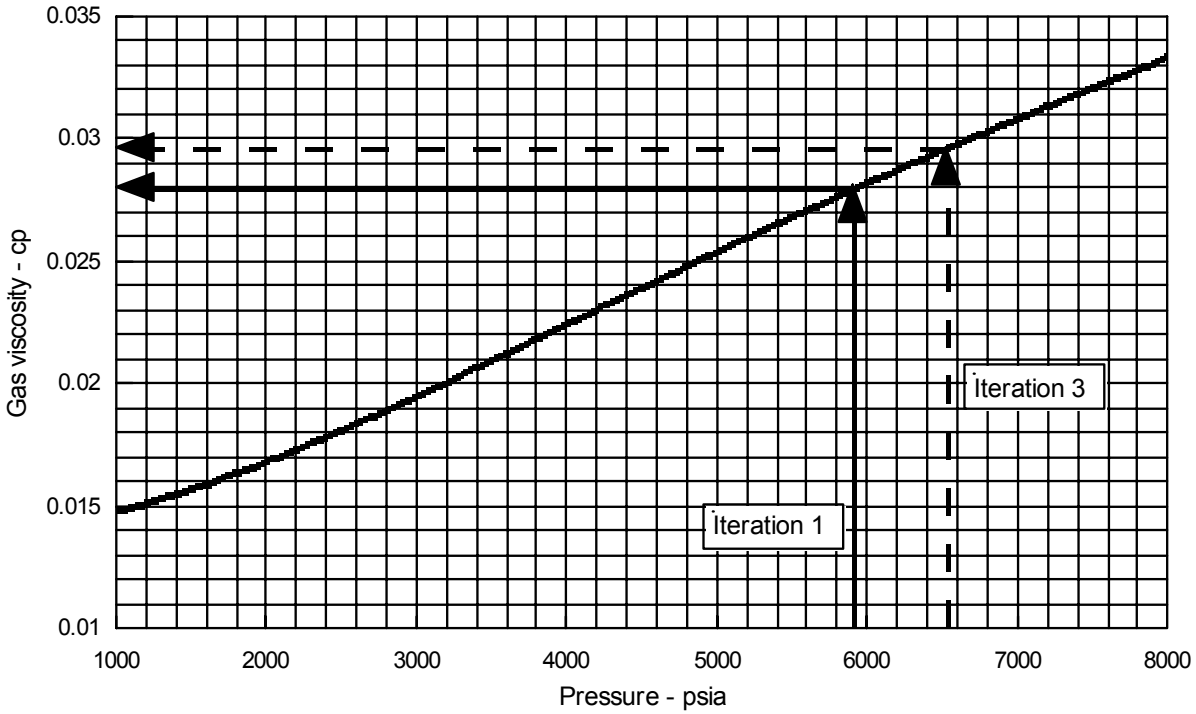

Figure C-5: Gas Viscosity versus Pressure

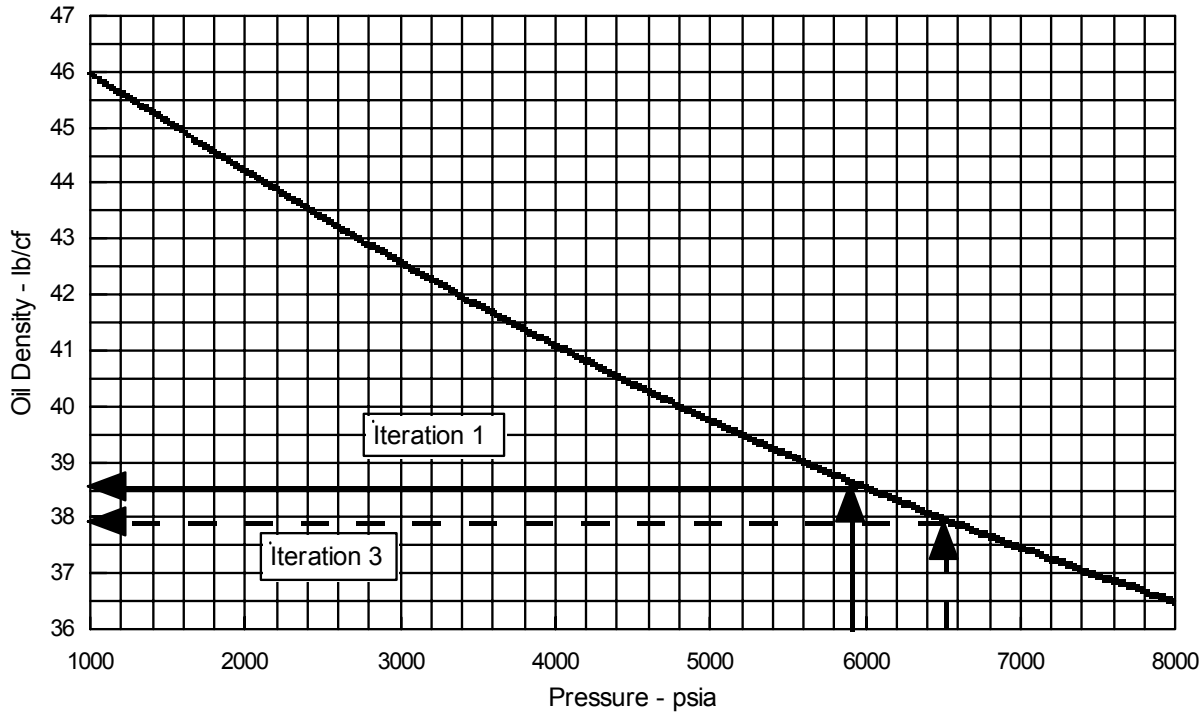

Figure C-6: Oil Density versus Pressure

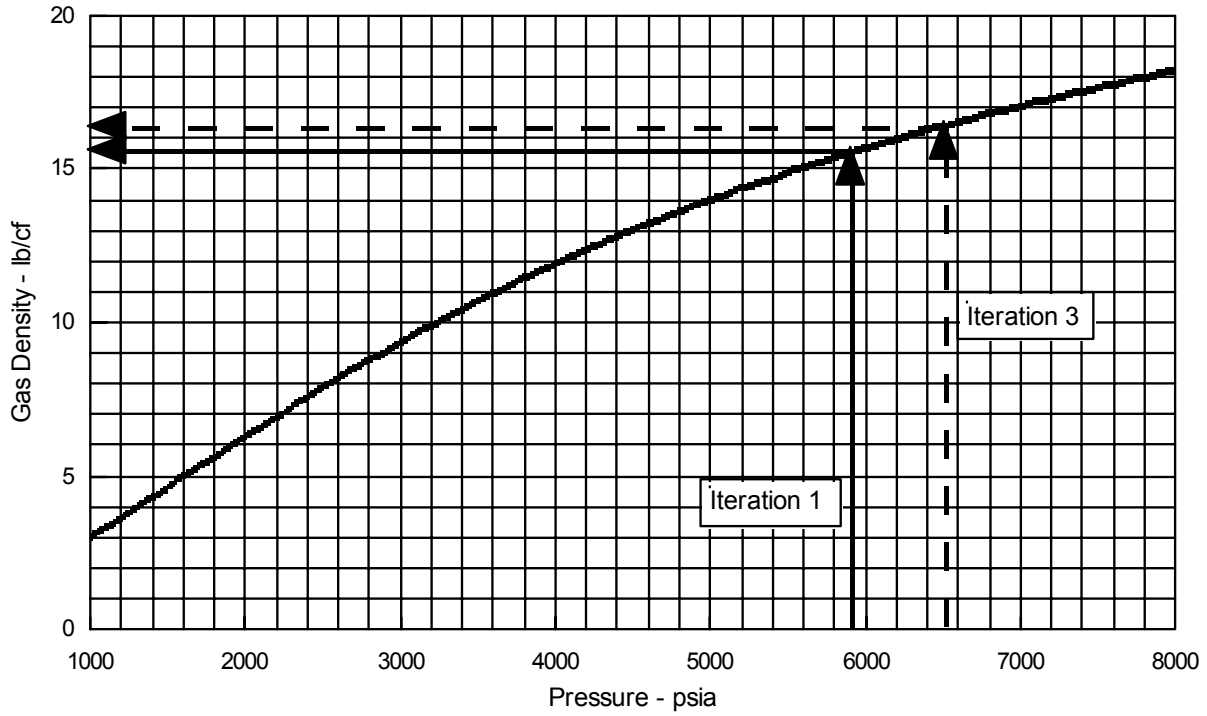

Figure C-7: Gas Density versus Pressure

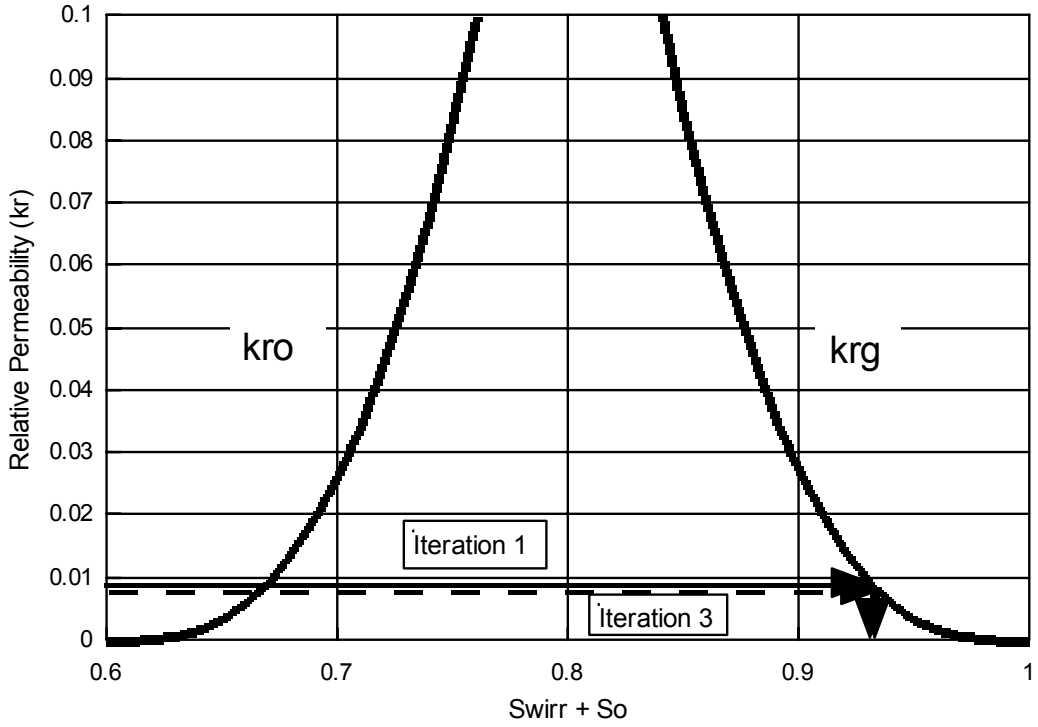

Figure C-8: 2-Phase Oil-Gas Relative Permeability versus Liquid Saturation

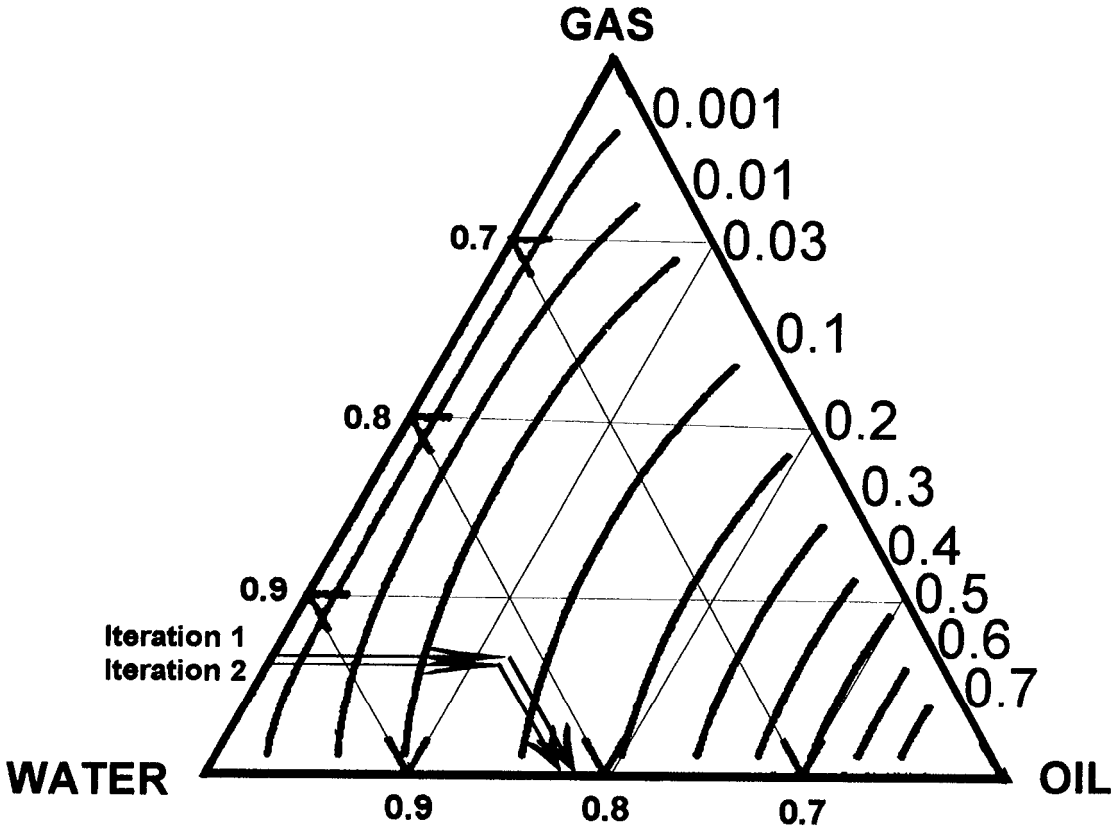

Figure C-9: 3-Phase Oil Relative Permeability versus Water and Gas Saturation

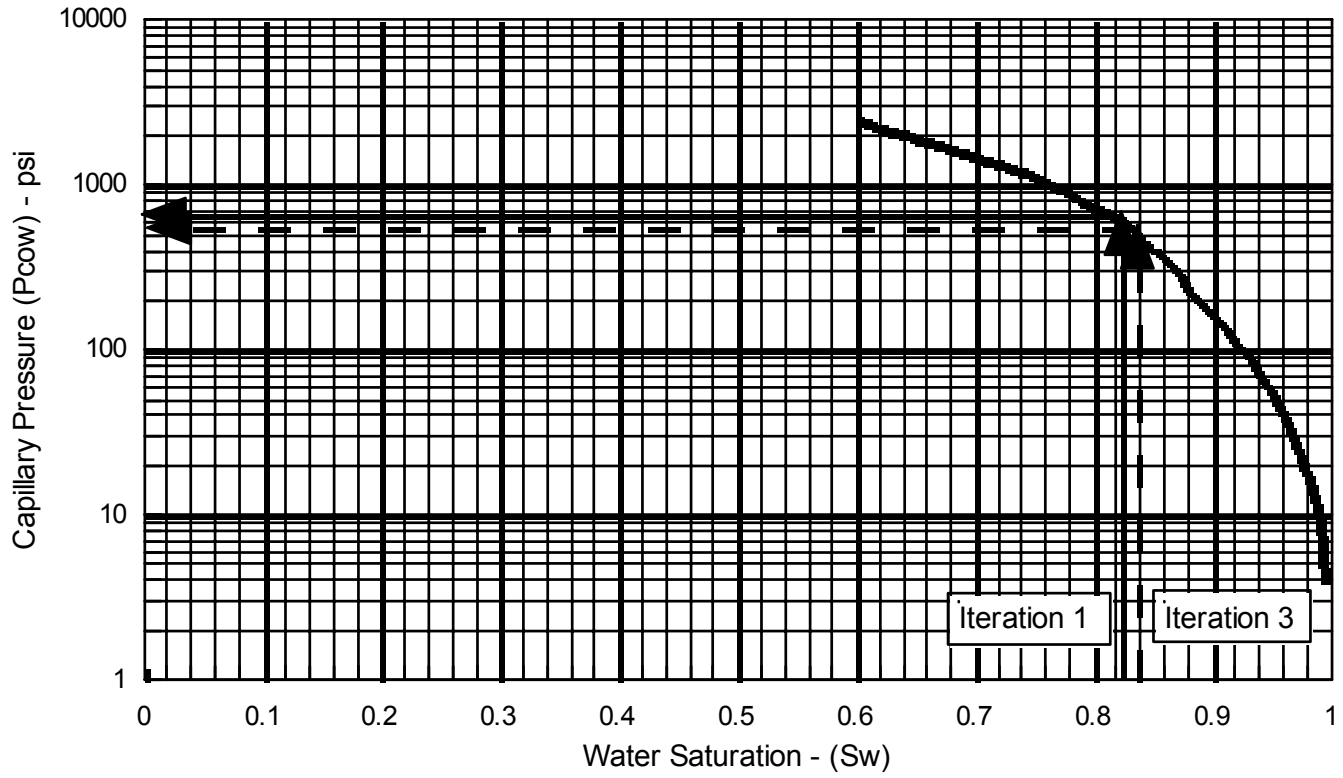

Figure C-10: Oil-Water Capillary Pressure versus Water Saturation

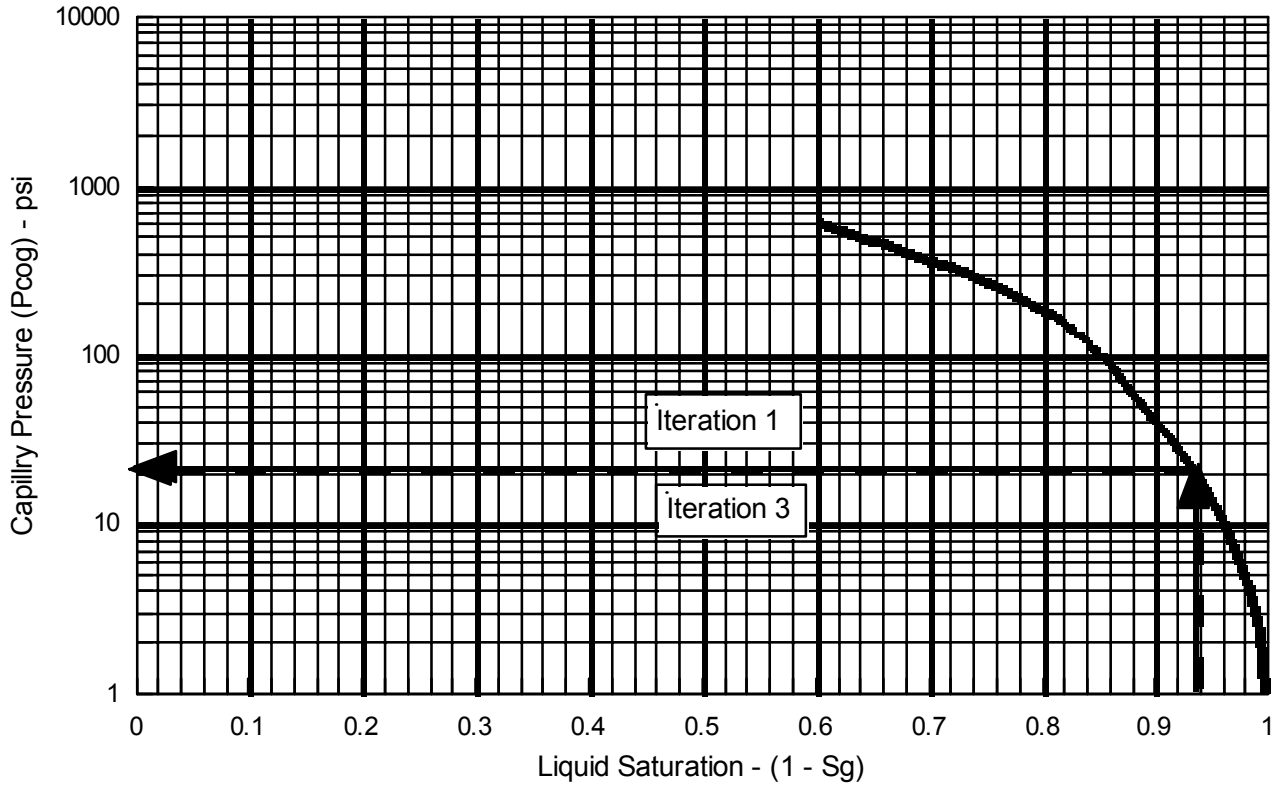

Figure C-11: Oil-Gas Capillary Pressure versus Liquid Saturation

Appendix D

FAULT-ZONE GEOMETRY AND ANISOTROPY EFFECTS IN 2-PHASE SYSTEMS

MODEL OBJECTIVES

The purpose of this modeling work was to investigate the effect of fault anisotropy upon reservoir charge rate. In previous simulations (Bennett, 1996) it had been noted that virtually all the oil injected into the fault would charge the reservoir sand until the oil column height approached the steady-state column height. As the steady state column height was approached, oil would begin to bypass the reservoir and migrate to shallower reservoirs. Anisotropic effects were evaluated on the basis of pseudo steady state reservoir bypass, or the percentage of oil being injected into the fault which bypasses the reservoir sand and continues migrating up the fault. This is measured when the reservoir charge rate has become stable and the oil column is still much less than the steady-state column height.

The bypass is illustrated in *Figure D-1* and *Figure D-2*. Given a single sand system charging at a constant volumetric rate of Qi (*Figure D-1*), some of the hydrocarbon will enter the sand (Qc) and some of the hydrocarbon will bypass the sand and flow up the fault (Qb). Since we are evaluating an incompressible system, the principle of mass conservation gives, $Qb + Qc = Qi$. We define the percent bypassing the reservoir as $Qb/Qi \bullet 100$. This percent bypass will remain relatively constant until the

steady-state column height is approached, indicating that the sand is charging at a relatively constant rate. This is illustrated in *Figure D-2* which plots cumulative volumes versus time. The top curve represents cumulative volume injected (Qi*t) at the bottom of the fault versus time. The fairly constant slope regions of the other two curves (between 0.4 and 5.0 million years) are the pseudo steady-state regions where the sand is charging at a relatively constant rate and a fairly constant fraction of the hydrocarbon is bypassing the sand and continuing up the fault. Late in the simulation the oil in place curve flattens out, indicating the sand is reaching its maximum (or steady state) oil in place and there is a corresponding increase in the slope of the bypass curve as more oil bypasses the sand and continues up the fault.

OVERVIEW

We consider two basic models: 1) "sand smear" and 2) "shale smear". The sand-smear model is comprised of a relatively thick fault (33 feet) with a thin (3 feet) low-permeability core (*Figure D-3*). The physical model for this permeability structure is that the fault prior to significant displacement had, overall, a relatively high permeability. Perhaps, for example, the fault was entirely within a sandstone bed. When the displacement occurred a large damaged zone representing the total thickness of the fault was created. The majority of the displacement however was focused along the core of the fault. This localized displacement pulverized the sand matrix causing a loss of permeability along the central core. This geometry is described by Caine, et al., (1996) as a combined conduit-barrier fault structure. It was also noted by Caine, et al., (1996)

that this type of fault has a permeability structure which causes flow to be preferentially oriented parallel to the fault.

The shale-smear model contrasts that of the sand-smear model in that the fault is thinner (7 feet) and the core now has a high, not low, permeability (*Figure D-4*). In this case the fault is within interbedded sands and shales and the shale is relatively ductile. As fault displacement occurs, shales are dragged along the fault resulting in the generation of a low-permeability sheath around the fault zone. This sealing mechanism is common in oilfields of the Niger Delta as described by Bouvier, et al., (1989).

MODEL CONSTRAINTS

Figure D-5 illustrates a typical simulation grid for both the sand-smear and shale-smear models. Note that there are three grid blocks across the width of the fault. The middle column is too thin to be apparent in *Figure D-5*. In all the simulation results presented for both the sand-smear and shale-smear models there is a constant pressure boundary condition imposed at the downdip end of each reservoir sand (*Figure D-5*). The constant pressure boundary is modeled by adding grid blocks (not shown in *Figure D-5*) between the end of the sand and the top of the fault. This keeps the aquifer region of each sand in hydrodynamic equilibrium with the top of the fault. In all the simulations there is a well injecting oil at a constant rate at the bottom of the fault zone and there is a well producing with a constant bottom hole pressure (hydrostatic) specification at the top of the fault zone (*Figure D-5*). Rock properties and grid geometries for both the sand-smear and shale-smear models are listed in *Table D-1*. Fluid properties are listed in *Table D-2*.

Table D-1: Rock Properties and Grid Geometry, Sand-Smear and Shale-Smear Models

Rock Properties	Reservoir	Fault Sheath	Fault Core
Permeability (horizontal)	1.00 md	1.7x10-2 - 1.7x10-6 md (sand-smear) 2.4x10-4 - 2.4x10-5 md (shale-smear)	2.4x10-4 - 2.4x10-8 md (sand-smear) 1.7x10-2 - 1.7x10-3 md (shale-smear)
Permeability (vertical)	0.1 md	0.017 md (sand-smear) 0.00024 md (shale-smear)	0.00024 md (sand-smear) 0.017 md (shale-smear)
Porosity	20 %	15 %	15 %
Thickness	50-200 ft	30 ft (sand-smear) 3 ft (shale-smear)	3 ft (sand-smear) 0.6 - 1.2 ft (shale-smear)
Width	120 ft	120 ft	120 ft
Angle from horizontal	10^o	80^o	80^o

Table D-2: Fluid Properties, Sand-Smear and Shale-Smear Models

Fluid Properties	Oil	Water
Density	53.05 lb/ft3	62.42 lb/ft3
Viscosity	0.35194 cp	0.18386 cp

The reservoir sand and fault zone oil-water capillary pressure data given in *Figure 2-4* were used for all models presented in this section. The Leverett-J function (Amyx et al., 1960) can be used to scale capillary pressure as a function of permeability (k) and porosity (ϕ). In the previous modeling effort (Bennett, 1996), it was determined that capillary pressure should be scaled in the direction of highest permeability. Because the vertical permeability of the fault zone in all the runs was held constant and was equal to or greater than the horizontal permeability, oil-water capillary pressure was not scaled. Both regions within the fault zone use the capillary pressure data given in *Figure 2-4*.

Fault zone and reservoir sand oil-water relative permeability data are give in *Figures 2-5* and *2-6*, respectively. All fault zone rock and fluid properties, with the exception of horizontal permeability, were the same for all sand-smear and shale-smear simulations.

SAND-SMEAR MODEL

The input data and results for the sand-smear simulations are summarized in *Table D-3*. In all sand-smear simulations the core of the fault was modeled with a vertical permeability of 0.00024 md and the sheath with a vertical permeability of 0.017 md. Various ratios of vertical to horizontal permeability (kv/kh) were investigated by holding the vertical permeability constant according to *Table D-1*, while decreasing the horizontal permeability of both the fault core and sheath in each simulation to create the permeability ratios in *Table D-3*. The fault was modeled with three horizontal grid blocks, one for the core and one on each side of the core for the sheath (*Figure D-5*). The reservoir sand was modeled as being either 50 feet thick (one grid block) or 200 feet thick (4 grid blocks) [*Table D-1*]. The fault zone capillary pressure curve given in Chapter 2 (*Figure 2-4*) was used for both zones of the fault. The oil injection rate for all sand-smear runs was 4.74×10^{-4} res.bbl/day (6.27×10^{-8} res.bbl/day/ft^2).

Table D-3: Summary of Simulations with Anisotropic Fault, Sand-Smear Model

Run Name	Fault Permeability Ratio, kv/kh	Sand Thickness Feet	Number of Cells in Sand	Reservoir Bypass Percent
Run A1	1	50	1	5
Run A2	10	50	1	45
Run A3	100	50	1	87
Run A4	1,000	50	1	97
Run A5	1	200	4	2
Run A6	10	200	4	39
Run A7	100	200	4	85
Run A8	1,000	200	4	96
Run A9	10,000	200	4	100
Run A10	10	200	4	35
Run A11	100	200	4	41
Run A12	1,000	200	4	55
Run A13	100	200	4	40

The major conclusions and observations from the sand-smear are:

1. The anisotropy of the fault has a significant impact on reservoir bypass.
2. The location of the source bed relative to the potential reservoir sands (same or opposite side) is an important factor in controlling how effectively the sands are charged.
3. Sand thickness has only a minor impact on reservoir bypass.
4. Reservoir charge rate is controlled primarily by the horizontal permeability of the damaged fault core when the source and reservoir are on opposite sides of the fault.

Additional information on the sand-smear model runs is given below.

Run A1 through Run A9 investigate the effect of fault anisotropy and sand thickness upon oil bypass. For all these runs the injection and production wells are located on the footwall (high permeability) side of the fault, opposite the sand. The sands are attached to the hanging-wall side of the fault and the low-permeability core of the fault acts as a barrier to flow from the fault to the sand.

Run A1 through Run A4 investigate the effect of increasing fault anisotropy in one order of magnitude increments upon oil by-pass of a 50 foot sand. The 5 percent oil bypass in Run A1 demonstrates that even for an isotropic fault, the low-permeability core can act as barrier to oil migration to the sand. By imposing an anisotropy (kv/kh) in the fault of one order of magnitude (Run A2), oil bypass of the sand is increased to 45 percent. Increasing anisotropy to a factor of 100 (Run A3) causes bypass to increase to

87 percent. Increasing the anisotropy to a factor of 1000 causes almost complete (97 percent) bypass of the potential reservoir sand.

Run A5 through Run A8 are similar to runs Run A1 through Run A4 with the sand thickness increased to 200 feet (and from 1 grid block to 4 grid blocks thick). Comparing runs with the same anisotropy and different sand thickness shows that increasing the sand thickness has only a minor effect in decreasing oil bypass. Additionally, Run 9 was made with an anisotropy of 10,000. This run shows that the resistance to horizontal flow in the fault for anisotropy in excess of 1,000 would not allow capillary forces to drive oil into the sand (bypass is 100 percent).

Figure D-6 shows the oil saturation in the fault and reservoir sand, for Run A5 through Run A8, 1 million years after initiating oil injection. It can be seen that even though the oil injection rate into the fault is the same for all four runs, much less oil charges the sand as the anisotropy is increased. This is particularly noticeable in Run A7 and Run A8 which have anisotropy ratios of 100 and 1,000 respectively.

Additionally, there is a significant change in oil distribution (*Figure D-6*) within the fault as anisotropy is increased. In Run A5 the oil saturation is fairly uniform across the fault. In Run A6 the oil saturation is slightly higher on the footwall side of the fault (opposite the sand) were the injection and production wells are located. In Run A7 the oil saturation on the footwall side of the fault is twice that of the hangingwall side and in Run A8 the saturation difference across the fault is nearly a factor of four.

Run A10 through Run A12 are the same as Run A6 through Run A8, respectively except the oil injection is distributed across the fault by using a row of cells across the

bottom of the fault with flow properties equivalent to the sand. Run A10 shows that oil by-pass is decreased by 10 percent for a fault with an anisotropy ratio of 10. The reduction in oil by-pass is much more prominent in Run A11 and Run A12 where anisotropy is 100 and 1,000 and by-pass is 41 and 55 percent, respectively. This indicates that oil bypass is significantly influenced by anisotropy of the high permeability zone of the fault (Run A10 through Run A12) as well as the barrier effect of the low permeability core (Run A6 through Run A8). This implies that the location of the source bed (same or opposite side as the reservoir) becomes more important in evaluating reservoir charging as fault zone anisotropy increases.

Run A13 was run to confirm the findings of runs Run A10 through Run A12. This run was similar to Run A11 except flow properties equivalent to the sand were assigned to the top and bottom rows of cells in the fault. Oil bypass for this run was similar to the results for Run A11 indicating the location of the production well at the top of the fault is not very important in these simulations.

SHALE-SMEAR MODEL

The input data and results for the three shale-smear simulations are summarized in Table 4 and the results are discussed below. Both the production well and injection well were located in the core of the fault. The oil injection rate was 2.37×10^{-4} res.bbl/day (one-half that of the sand-smear model) and the reservoir sand thickness was 50 feet for all shale-smear runs. Numerous unsuccessful attempts were made to run models with a fault geometry consisting of a 3 ft sheath and a 0.3 ft core at various flux rates.

Table D-4: Summary of Simulations with Anisotropic Faults, Shale-Smear Model

Run	Fault Anisotropy kv/kh	Fault Core Thickness ft	Oil Flux Fault Core res.bbl/day/ft2	Oil Flux Whole Fault res.bbl/day/ft2	Percent Bypass
Run A14	1	1.2	1.65x10-6	1.50x10-7	72
Run A15	1	0.6	3.30x10-6	1.57x10-7	8
Run A16	10	0.6	3.30x10-6	1.57x10-7	99

The major conclusions and observations from the shale-smear model are:

1. The effects of fault anisotropy on reservoir bypass are much more dramatic for the shale-smear model than for the sand-smear model.
2. Relative thickness of the fault core to the sheath, has a significant impact on reservoir bypass

Additional information on the shale-smear model runs is given below.

Run A15 was used as a base run to investigate the effect of relative core thickness and anisotropy within the fault. *Figure D-7* shows the oil saturation in the fault for Run A15. Note that the fault core saturation has been blownup and placed beside the fault for clarity. It can be seen that even for the isotropic case in the shale-smear model the oil saturation is much higher in the fault core (0.10) than in the sheath (0.05)

Run A14 shows the effect of increasing the core thickness relative to the low-permeability exterior thickness without changing the injection rate. Even though the fault is isotropic, increasing the core thickness provides a less resistant path from injection well to production well. This decreases the oil saturation in the fault and thus the capillary pressure driving the oil into the sand. Oil bypass is increased from 8 percent to 72 percent for the same oil injection rate.

Run A16 shows the effect of fault anisotropy in the shale-smear model. Near complete oil by-pass (99 percent) occurs at an anisotropy ratio of 10. By comparison an anisotropy in excess of 1,000 is necessary to achieve complete oil bypass in the sand-smear model. The additional flow up the core relative the sheath can also be seen in the oil saturation where the core oil saturation has increased to 0.17 while oil saturation in the sheath has dropped to 0.03.

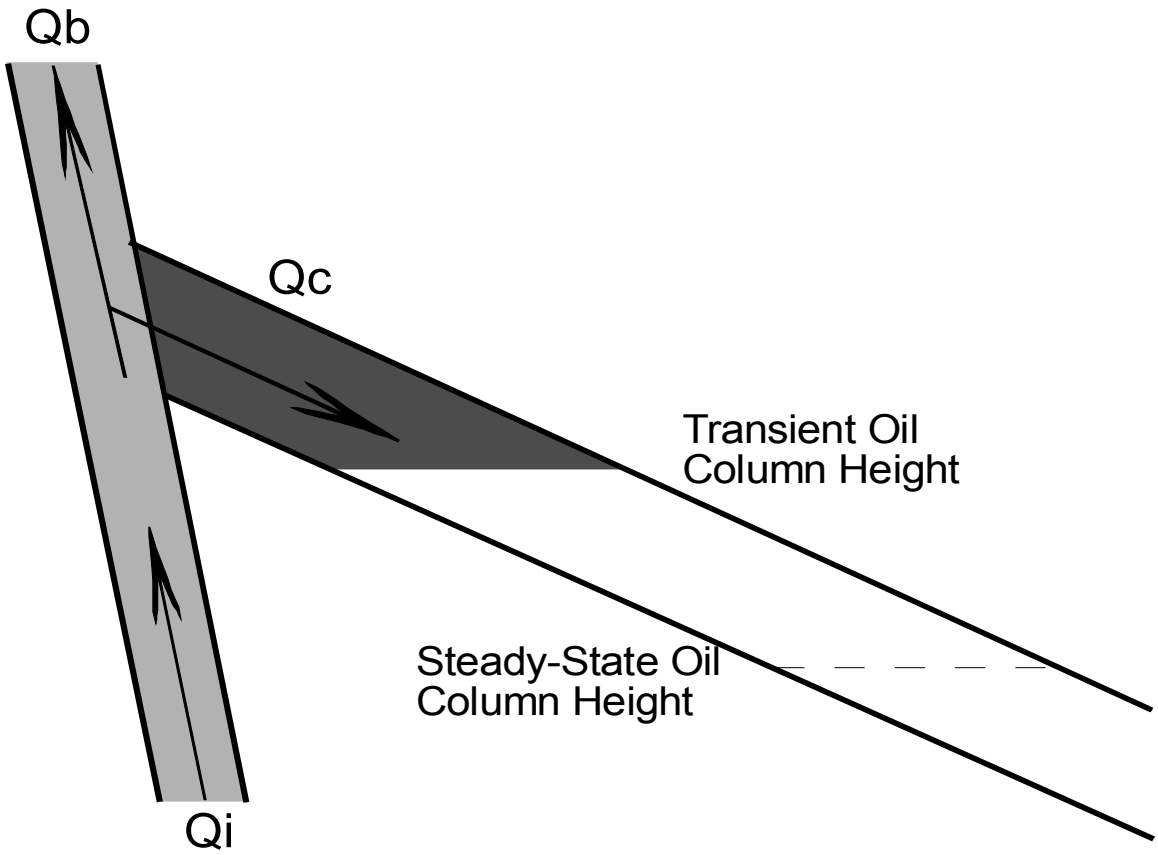

Figure D-1: Fault/reservoir flow schematic depicting oil charging the fault $\mathbf{Q_i}$, oil charging the sand $\mathbf{Q_c}$ and oil bypassing the sand $\mathbf{Q_b}$ at pseudo steady-state conditions.

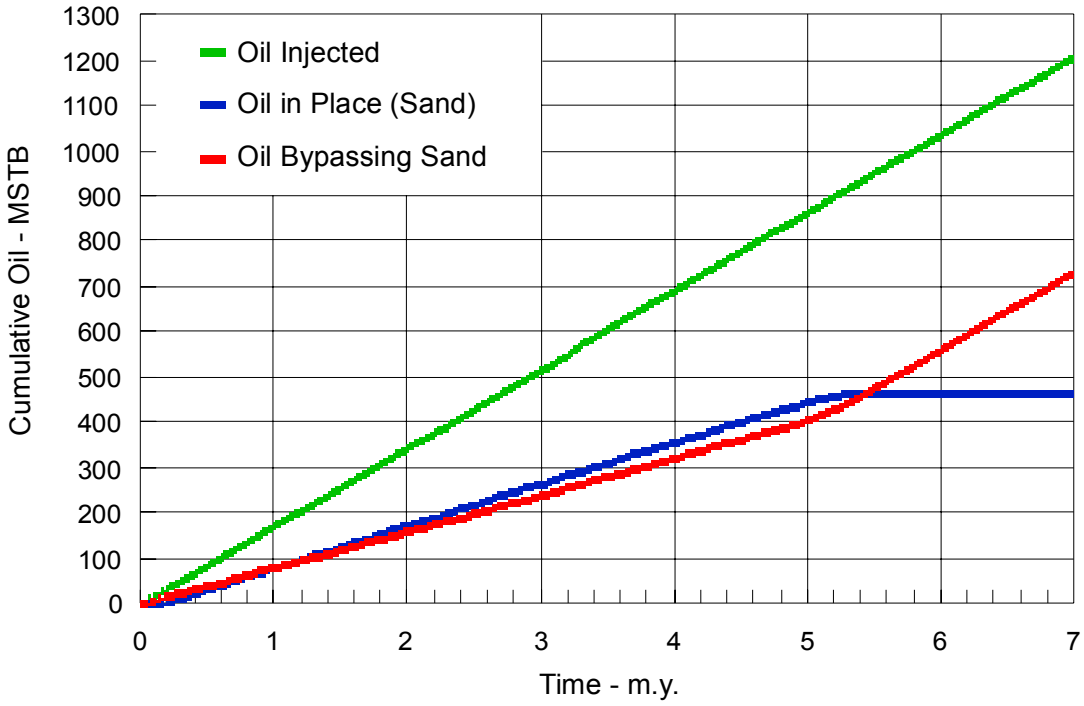

Figure D-2: Fault/reservoir cumulative flow for Run A2 showing pseudo steady-state (1 to 5 million years) and steady-state (t > 5.5 million years) time periods.

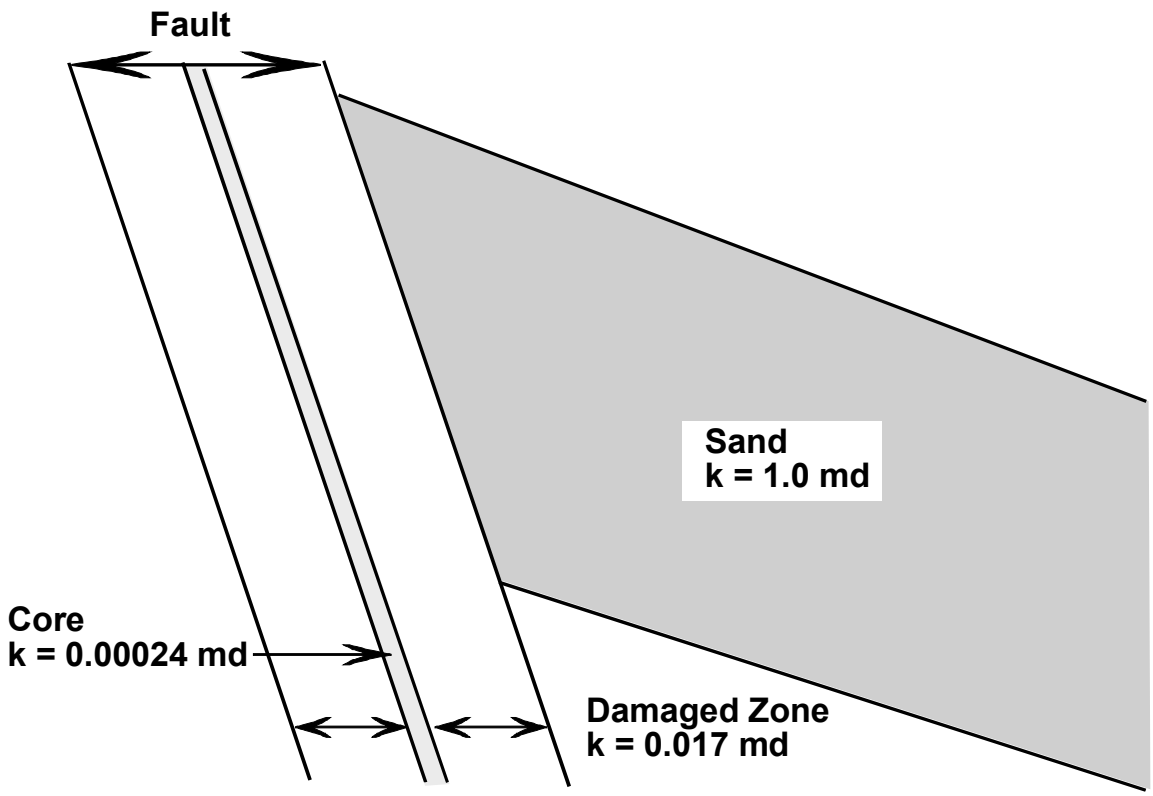

Figure D-3: Schematic of the sand-smear model geometry showing the low permeability core and high permeability damaged zone.

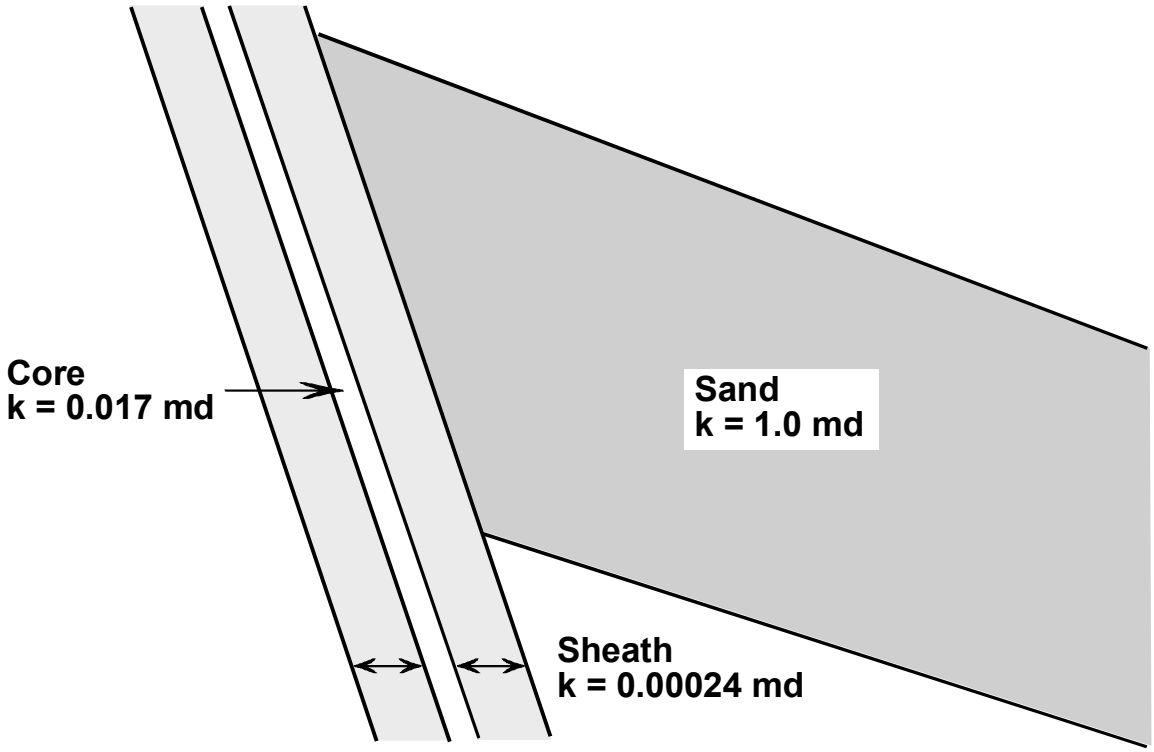

Figure D-4: Schematic of the shale-smear model geometry showing the high permeability core and low permeability sheath.

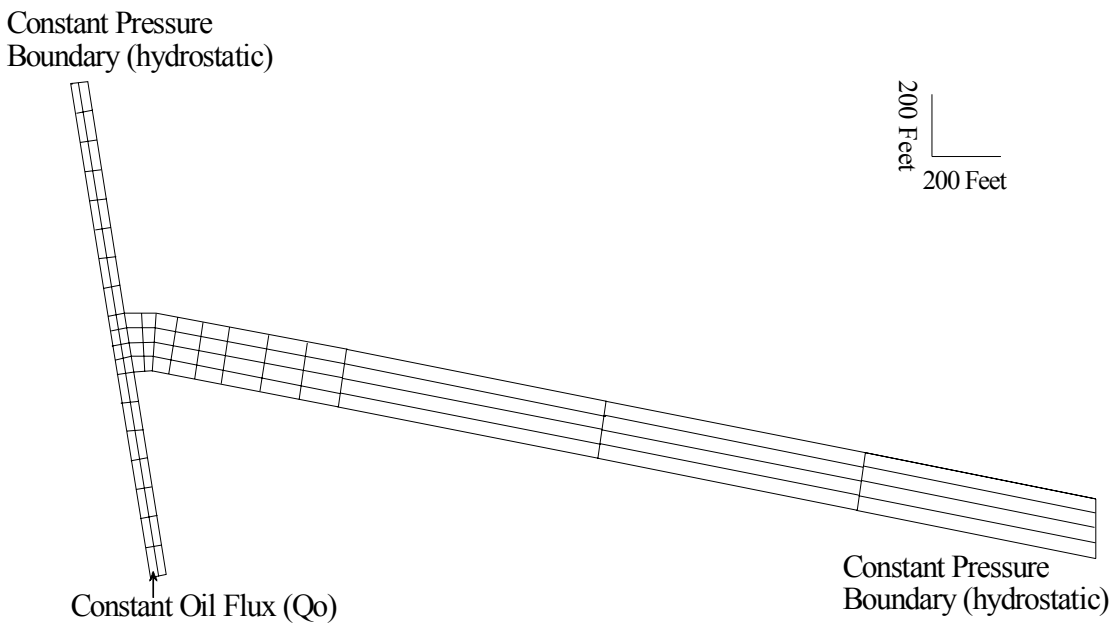

Figure D-5: Typical model grid geometry and boundary conditions for sand-smear and shale-smear models.

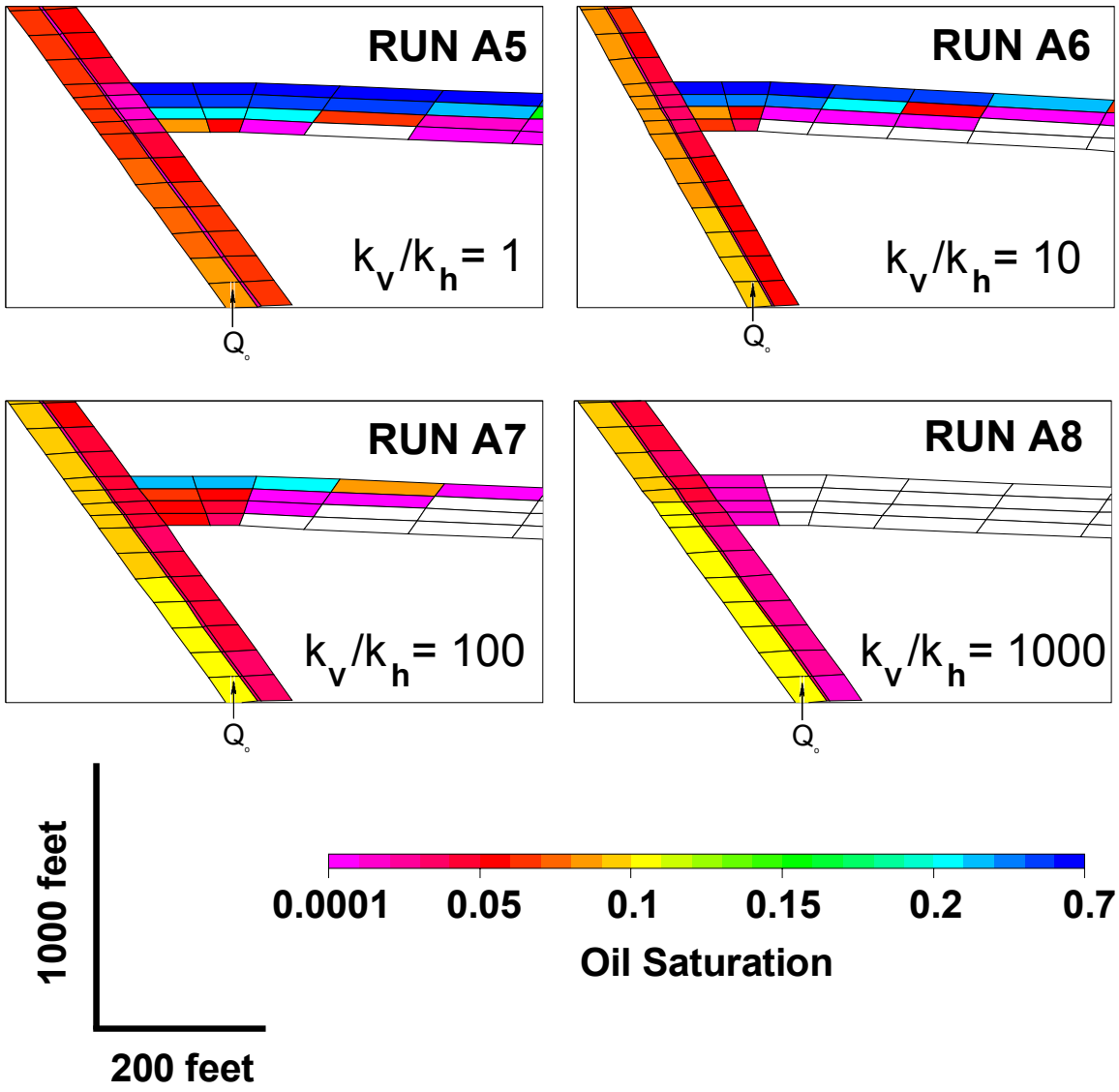

Figure D-6: Oil saturation at 1 million years for sand-smear model with source on footwall side of fault and potential reservoir sands on hangingwall side. As k_v/k_h increases, horizontal flow through the fault decreases, and oil saturation is skewed to the footwall (source) side of the fault.

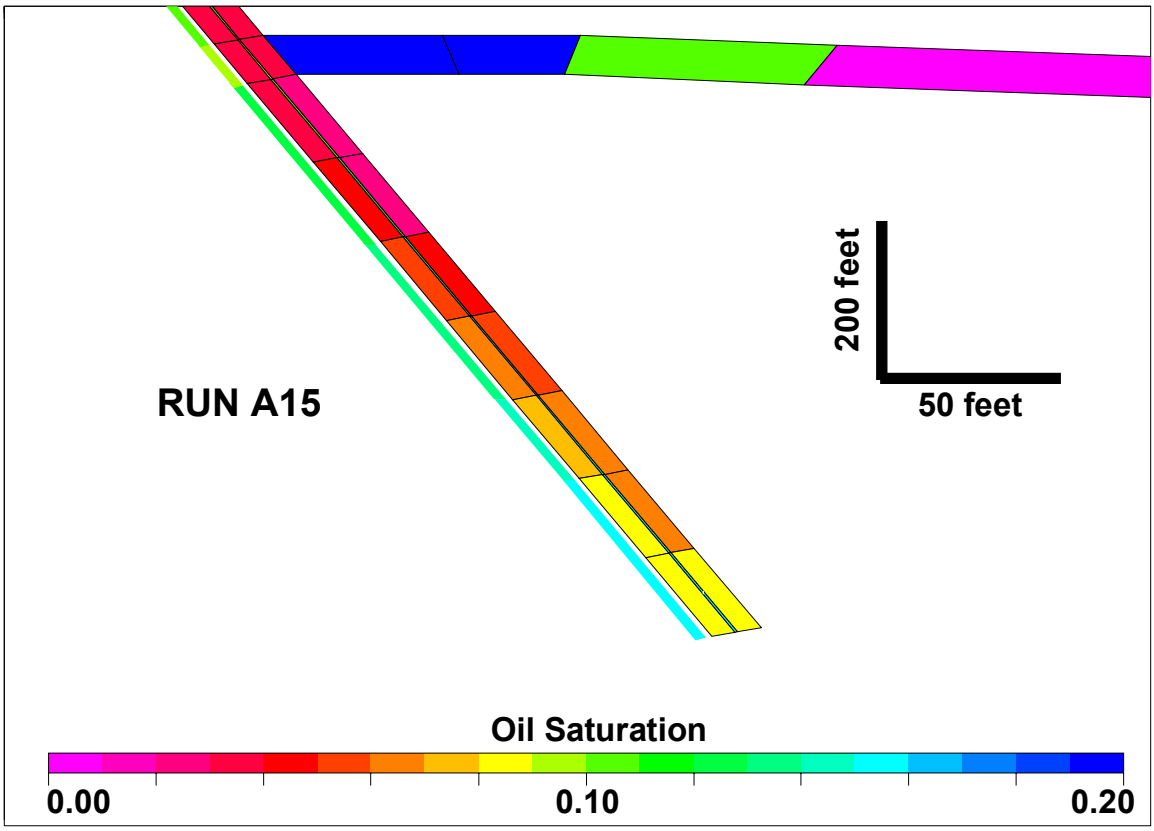

Figure D-7: Fault zone oil saturation in the shale-smear model. Oil saturation in the high permeability core is twice that of the sheath